Evaluation of Heat Transfer Coefficient during Quenching of Steels

A thesis

Submitted to the Department of Electromechanical Engineering/ University of Technology in a partial fulfilment of the requirements for the degree of Doctor of philosophy in Mechanical Engineering

Hala Salman Hasan

September 2009

Failure is the opportunity to begin again more intelligently.

Henry Ford

To my family

With my all respect, appreciation, and love.

Hala

Acknowledgement

I would like first to take this opportunity to express my sincere thanks and appreciation to Prof. Harry Bhadeshia, Prof. Jalal M. Jalil, and Mr. Mathew Peet, my supervisors in the University of Cambridge, UK, and the University of Technology, Baghdad, for the excellent support and guidance they have given me through my thesis work, they have been helpful and generous with their time and expertise to evaluate my thesis. I would like to extend my appreciation to Asst Prof. Mohammed J. Kadhim for his valuable comments in the start of this study.

I am extremely grateful to Ministry of Higher Education and to Electromechanical Engineering Department in the University of Technology for giving me the opportunity to perform my thesis work in collaboration with Department of Materials Science and Metallurgy in the University of Cambridge.

I am extremely grateful to Harry Bhadeshia, Department of Materials Science and Metallurgy / University of Cambridge, British Universities Iraq Consortium, and Murray Edwards Collage for the financial support which provides me the opportunity to pursue research at Cambridge during the last three years.

I wish to thank all members of the Phase Transformation Group for their continuous help and friendship, in particular Mathew, Amir, Stéphane, and also to the staff in the library, the laboratories, and the workshop in the department of materials science and metallurgy in Cambridge especially Kevin for their continuous help.

I wish to express my thanks to all my friends with special thanks to Eleanor, Suad, Aseel, Mohammed, Anwar, Akeel, Salam, Nuha, Amro, Paola, Samera, Thoraya and Suhal.

I am greatly indebted to my family for their support, devotion and understanding through all my life.

Abstract

The control of steel quenching has been investigated in this study by developing a physically based mathematical model using the control volume method, to simulate the quenching process and to predict the time-temperature history, quench factor, and as-quenched hardness. Accurate prediction requires knowledge of the boundary conditions, and the heat transfer coefficient which is the key parameter for quenching simulations.

The heat transfer coefficients for steels as a function of temperature were obtained by developing a suitable measurement probe. Both lumped heat capacity (Biot number ≤ 0.1) and inverse heat conduction models were utilised in the design of the probe dimensions (2 mm diameter, 10 mm length). The time-temperature history was recorded using a 1 mm K-type thermocouple inserted in the geometric centre of the cylindrical probe; these data were used to calculate the heat transfer coefficient as a function of temperature. Six steel probes with different chemical composition were used to investigate the generality of the method.

A 60×20 mm steel sample was used to demonstrate the modelling technique and to assess the applicability of the calculated heat transfer coefficient to another sample with different dimensions. Good agreement was found between the results for cooling curves and hardness distribution obtained from the quenching process modelling program and the experimentally measured cooling curves and hardness.

The performance of a number of quenchants in varying conditions was also investigated, and the designed probe was used to illustrate the effect of quenching parameters (quenchant type and quenchant temperature) on cooling

rate, heat-transfer coefficient, quench factor, and the estimated as-quenched hardness. The results show that the heat transfer properties are greatly affected by the quenchant parameters which influence the quench factor and the mechanical properties of the sample.

Thermal conductivity is also an important boundary condition for simulating the quenching process. A neural network model was formulated to estimate the thermal conductivity of steels as a function of temperature and chemical composition. With this model it is possible to simulate the quenching process for any steel rather than being limited to only those with available data. It is also a necessary tool to improve the design of steels and the heat treatment process.

Contents

Chapter 1

Introduction and Literature review

1.1 Introduction

The outstanding feature of steels which makes them such successful engineering materials is the ability to adjust the mechanical properties over a wide range using controlled heat-treatments.

The most thermodynamically favoured steel structures are produced when steel is heated to the high temperature austenite state and slowly cooled. This treatment produces a structure that has a low level of residual stress locked within the steel. However, high strength is achieved usually by rapid cooling to form a bainitic or martensitic microstructure. The cooling conditions are then nonuniform and this leads to the evolution of stresses which may be detrimental to the life of the component.

Optimisation of the quenching process usually requires the selection of cooling rates fast enough to permit the desired martensitic microstructure to form to the required depth but slow enough to minimize residual stresses and distortion (figure 1-1). The quenching intensity can be changed by varying the

type of quenchant, its concentration and temperature, and the rate of agitation [1-4].

Quenching is an important step in producing many mechanical and automotive parts; it is often the most economical way to achieve high strength and hardness. Improper control of quenching can cause distortion or cracking. When this happens to components that have already gone through a number of previous processes, every rejected part represents a significant monetary loss [5, 6]. In fact, irreproducible results caused by uncontrolled quenching is one of the major causes of rejected components, production losses and the production of components that need to be reworked [7, 8]

Control of steel making, manufacturing, and processing such as heat treatment is being continually investigated and applied. This can best be achieved by the development of a physically based mathematical model [9]. In order to use such a model, the value of the physical variables related to the phenomenon which is represented must be known. The heat transfer coefficient is one of the most important of these factors in the context of quenching [10].

The thermal conductivity is also a significant factor in the heat treatment and the use of steels. Temperature gradients during cooling can lead to microstructural gradients and to residual stresses in steel components. Thermal transients can influence the development of stresses reducing service life and safety [11, 12].

Reliable prediction of the time-temperature history, microstructure and as-quenched properties of steel requires accurate data of the boundary conditions for the process simulation. Currently, one of the greatest impediments to a full predictive quench simulation tool is the inability to characterize the surface heat transfer coefficient [13, 14].

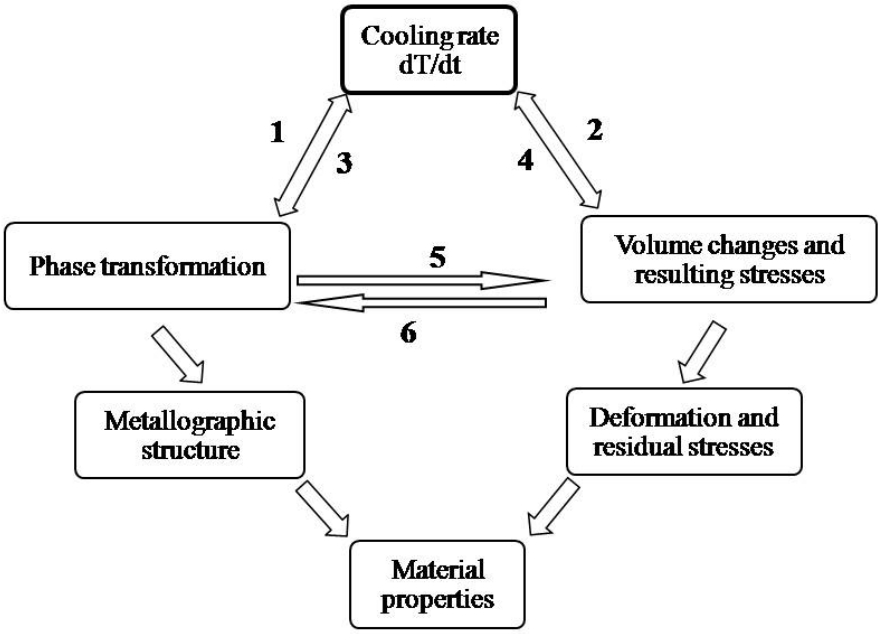

Figure 1-1: Coupling effect between cooling rate, phase transformation and stresses, and their influence on material properties.

1: Temperature dependent phase transformations.

2: Thermal stress.

3: Latent heat.

4: Heat of deformation.

5: Transformation strain.

6: Stress-induced transformation.

The major goal of this work is the accurate estimation of the heat transfer coefficient for steels at the interface between the steel and the quenching medium as a function of temperature, based on the cooling curves obtained by quenching a probe into the quenchant.

The other aim is to develop a neural network model to provide thermal conductivity values of the steel being used and how it changes with temperature depending on its chemical composition

In addition, this project focuses on the experimentally determined behaviour of different quenchants according to their physical properties (temperature and viscosity). The cooling curve was measured by the designed probe and used to calculate the quench factor. In the present work a kinetic program mucg83 [15] was used to obtain the equation that describes the time-temperature-transformation (TTT) curve for the alloy steel of interest to avoid the need for the equation constants which represent the main problem in the old approach in determining the quench factor (QF).

1.2 Literature review

The primary function of a quenchant is to control the heat-transfer rate from an object during the quenching process and to produce the desired combination of hardness, strength, and toughness. The quenchant should also minimize distortion due to the development of residual stresses by promoting the uniformity of cooling over the surface of the component. The mechanical properties obtained are significantly affected by the cooling rates attained during quenching [16-18].

Cooling curve analysis is the most useful tool in selecting the appropriate quenching medium for the heat treatment of steel parts. The technique evaluates the cooling power of quenching media by measuring the thermal response of a probe, suitably instrumented with thermocouples which are used later to estimate quench severity and quench factor. The most common probe configuration is a cylindrical bar with a length that is at least four times the diameter to minimize end cooling effects (figures 1-2 to 1-5). A thermocouple is usually located at the geometric centre of the probe. Probes with multiple thermocouples embedded are also used in order to measure thermal gradients [17-21].

Quenching probes are usually constructed from materials that do not exhibit any phase transformation during quenching, such as Inconel 600 [19, 22-24], silver [19, 22, 25] or 304 stainless steel [26-27], to allow the results to be interpreted without the complication of exothermic transformation. In addition, using such materials eliminates the danger of cracking of the probe; especially in the more severe quench media.

A variety of instrumented probes sizes, shapes, metals and data analysis strategies have been used for cooling curve analysis with various degrees of success [19-31]. There have been attempts to standardize probe design in order to facilitate the comparison of cooling curve data. Some of the standards developed include; the Japanese standard silver probe and the Wolfson probe which is constructed from inconel 600. Table 1-1 shows a comparison of cooling curve standards.

Tagaya and Tamura developed the Japanese industrial standard (JIS) [32, 33] for cooling curve acquisition utilizing a cylindrical silver probe with a thermocouple assembly specifically constructed to determine the change in surface temperature with time during quenching (figure 1-2). The cylindrical silver probe was adopted for the JIS method because of its high conductivity, the absence of phase transformation, and no surface oxidization; this means it has a high sensitivity and excellent reproducibility of results. However, its thermal conductivity is quite different from that of steel. It also has a high cost of manufacturing, and it is difficult to prepare delicate surface thermocouple assemblies, because silver is mechanically weak.

The probe currently with the widest acceptance as standard is the 12.5 mm diameter 60 mm length Inconel 600 probe. This probe is specified in the ISO method (figure 1-3) [18, 34] mainly because of its excellent mechanical properties. However its sensitivity is less than that of the silver probe. Also, the surface condition of this ISO probe is not stable during initial heating, while that of the silver probe is always stable. The Inconel probe has a thermal conductivity which is much closer to that of steel than is the case with silver. It also does not exhibit any phase transformations [19, 22-24].

Table 1-1: Comparison of probe specifications standards.

Variable	ISO 9950:1995(E) (International)	AFNOR NFT-60778 (France)	JIS K 2242 (Japan)	ZBE 45003-88 (China)	Proposed ASTM (United State)
Probe	Inconel 600	Silver, 99.999% pure	Silver, 99.99% pure	Silver, 99.96% pure	Inconel 600
Probe dimensions, Diameter × Length, mm	12.5 × 60	16 × 48	10 × 30	10 × 30	12.5 × 60
Probe quenching temperature, °C	850± 5	800± 5	810± 5	810± 5	850± 5

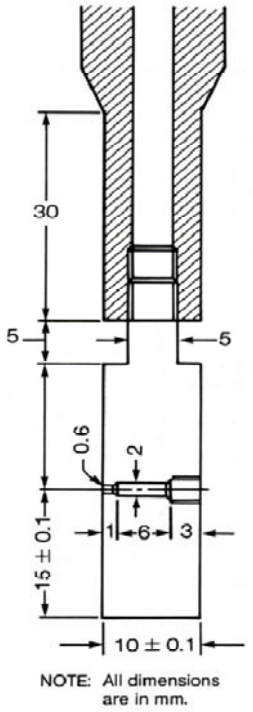

Figure 1-2: JIS Silver probe [18].

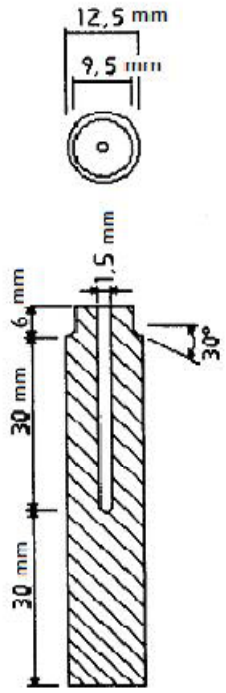

Figure 1-3: Inconel 600 probe [18].

Bates and Totten [35] have used an aluminium probe with multiple thermocouples (figure 1-4) to measure temperature gradients while cooling in various quenching media. The maximum difference in temperature between the surface and the centre of the probe can be used to estimate the propensity for stress formation and distortion during quenching.

Hines and Mueller [18] compared the performance of 25×100 mm cylindrical AISI 1546 steel (0.46 C-1.25 Mn wt%) and type 304 stainless steel probes (figure 1-5). Their results showed that the low hardenability AISI 1546 probe consistently produced longer vapour film stage time than the type 304 probe, both of which were quenched into the same medium. This behaviour was attributed to the exothermic phase transformation of austenite to ferrite and pearlite in the AISI 1546 steel. Similar results were obtained using AISI 5160 steel probe (0.6 C-0.8 Cr-0.88Mn-0.23Si wt%).

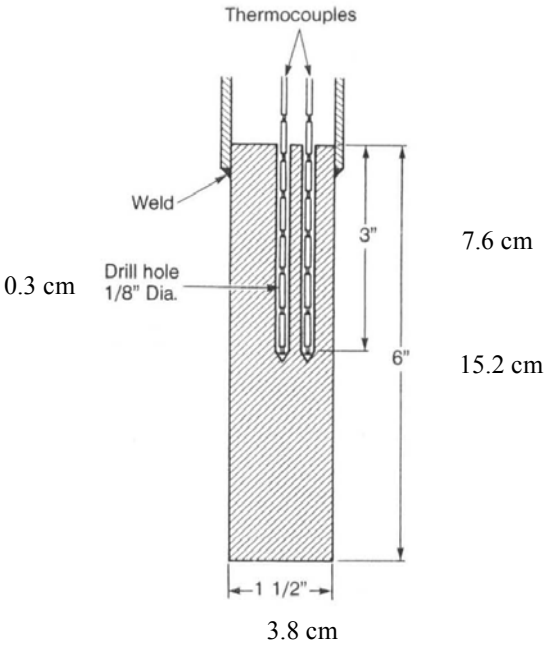

Figure 1-4: Multiple thermocouples probe [18].

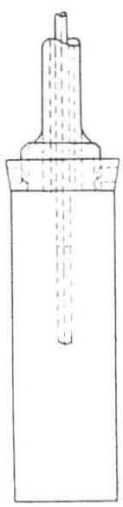

Figure 1-5: Hines-Mueller type 304 stainless steel probe [18].

1.2.1 Calculation of heat transfer coefficient

Quenching a hot object into a liquid medium involves a complex heat transfer process. Heat extraction from the surface of the object occurs through several different-heat transfer mechanisms and in distinct temperature ranges. The stages are: formation of vapour blanket film, nucleate boiling, and convection cooling stage. Reliable simulation of the quenching process requires accurate data of the boundary conditions; the heat transfer coefficient is the most important parameter during a quenching process [36-37], and it has a great influence upon the development of microstructure and residual stresses in steel parts. It is the key parameter in numerical simulations of the quenching process [16, 29, 38-43].

In much of the previous research, the surface heat transfer coefficients have usually been treated as constants. In reality, coefficients are nonlinear functions of the temperature and the volume fractions of the phases [43]. There have been attempts to evaluate coefficients as a function of temperature for steels during the course of quenching.

The estimation of the heat transfer coefficient is complicated by the latent heat released during phase transformations. In addition, the heat transfer coefficient during quenching of metals depends not only on the quenchant factor but also on work-piece factors such as its dimension and surface condition. Consequently, an estimation of the coefficients from cooling curve data obtained using the standard probe is often conducted. Because it is difficult to directly measure the cooling curve on the surface of a quenched probe, the inverse calculation method of heat transfer coefficient becomes a major method for solving the above problem [13, 22, 37, 44-52]. Figure 1-6 shows the surface heat transfer coefficient as a function of surface temperature

obtained using different probes materials, the probes dimensions are 30×90 mm cylinder quenched in water at 18 °C, the probes made from nickel, CrNi-steel, and Inconel 600. The figures 1-7 to 1-9 show the effect of quenchant parameters on the heat transfer coefficients, which will be explained in chapter 3.

One of the first attempts to devise a method of experimental measurement of overall heat transfer coefficients was by Lambert and Economopoulos [37]. This method involved the introduction of a probe inside the environment investigated (reheating furnace, quenching bath) while recording the time-temperature curve of a given point in the probe. And the overall heat-transfer coefficients were computed on the basis of experimental results, using a numerical solution of the inverse heat conduction problem, the probes were made from two different materials, nickel and mild steel.

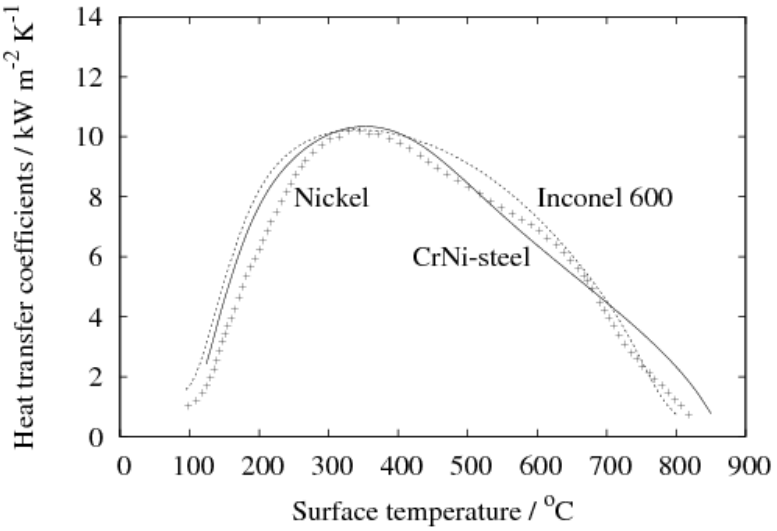

Figure 1-6: Heat-transfer coefficients as a function of temperature during quenching of cylindrical probe with 30×90 mm dimensions [18].

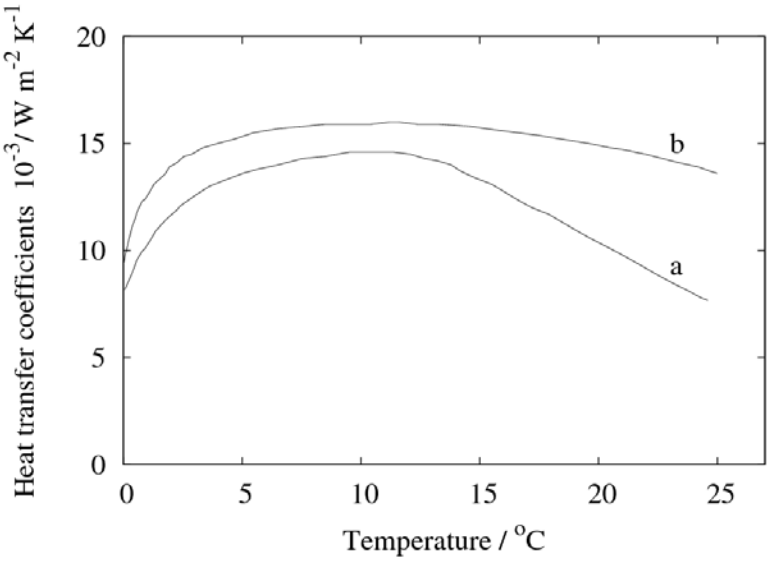

Figure 1-7: Effect of quenchant composition on the heat-transfer coefficients [18].

a-NaCl b-NaOH

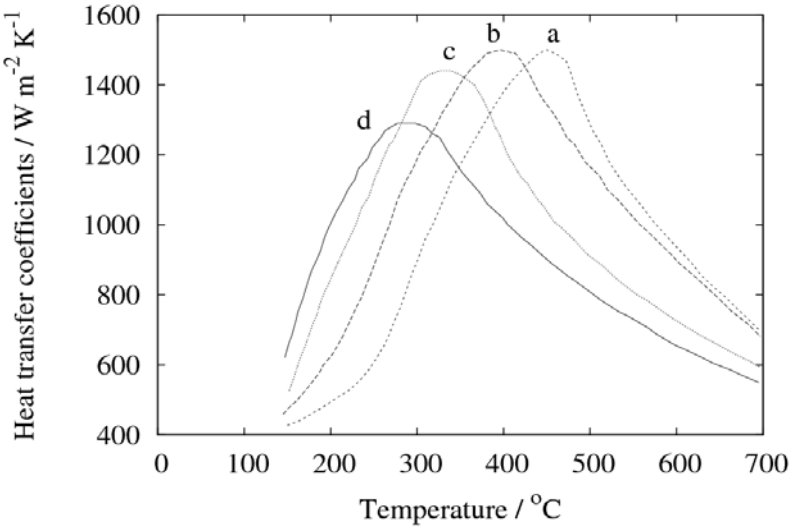

Figure 1-8: Heat-transfer coefficients as a function of temperature during quenching in various viscosity oil quenching [18]:

a- 113.9×10^{6} $m^2 s^{-1}$ b- 68.3×10^{6} $m^2 s^{-1}$

c- 31.1×10^{6} $m^2 s^{-1}$ d- 22.9×10^{6} $m^2 s^{-1}$

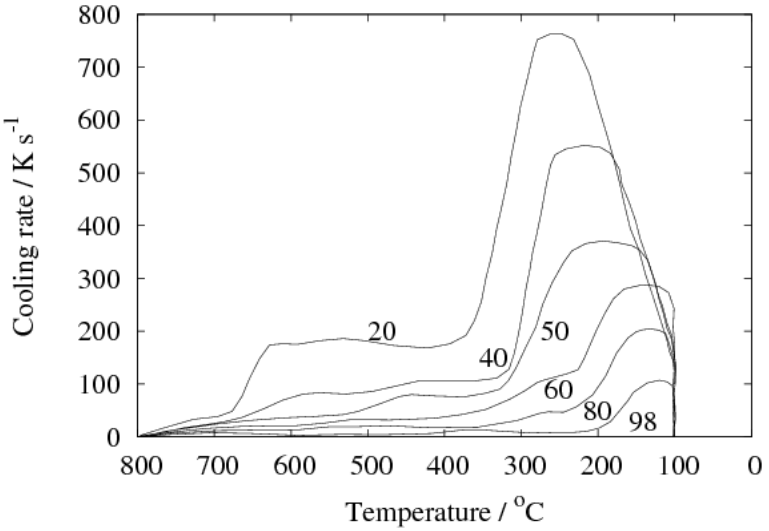

Figure 1-9: Cooling rates as a function of temperature obtained using silver ball with 20 mm diameter quenched in a different temperatures still water [1].

Many techniques have been developed for the inverse analysis method to compute surface heat transfer coefficient distribution from experimental data. The inputs to the analysis are the probe geometry, material properties, and the measured temperature histories, and the output is the heat transfer coefficient [13, 44-48].

Narazaki *et al.* [49] studied the influence of the accuracy of the heat transfer coefficients on the simulation of quenching process of steel. They found that the calculated cooling curves using the heat transfer coefficient which is estimated by the cooling curve data of the JIS silver probe or the ISO Inconel probe, were in reasonable agreement with the measured cooling curves during water quenching, while the heat transfer coefficient in polymer quenching should be modified with the cooling curve data of steel specimen.

They also confirmed the effects of the accurate prediction of the heat transfer coefficient on the calculated martensite transformation and the part distortion using the simulation methods.

Funatani *et al.* [22] tried to clarify the effect of the shape, size and material of probes on the result of the cooling curve test for oils, water and polymer solutions. They found that silver probes have better sensitivity than those made of Inconel, and give more useful data for the measurement of heat transfer coefficient.

Different commercial computer based instruments designed for testing quenching media in accordance with these standards are available. For example, IVF quench test, since 1988 [50] and, IVF smart quench system, since 2003 [51], which include the necessary computer software. This instrument allows the measurement of heat transfer coefficient (for the ISO 9950 probe) by the inverse method; the heat transfer coefficient can then be used for calculation of the microstructural constituents and the hardness profile of cylindrical samples of arbitrary diameter [52].

Until now probes dimensions of less than 10 mm are not often used because of the difficulty of temperature control during the transfer from the furnace to the quench bath, which make it very difficult to characterize the real heat transfer coefficient for steel, and that is the greatest impediment to a full predictive quench simulation tool.

1.2.2 Quench factor analysis

Quantifying quenching and the cooling effect of quenchants have been studied extensively. One method that quantifies the quench path and material

kinetic properties is called the ″quench factor″ and was described originally by Staley and Evancho, based on the Avrami or ″additivity″ rule [54-55].

Historically the average quench rate has been used to predict properties and microstructure after quenching, but it is not sufficient to provide accurate property data, and serve as a predictive tool. In all cases the quench factor was developed to quantitatively predict properties [56].

Since its development, Quench factor analysis has been applied to a wide range of aluminium alloy and steels to predict properties and/or optimise industrial quenching procedures, and has been recognised as an important technique for modelling property variation during continuous cooling [27, 57-61].

The procedures for developing the quench factor have been documented; the results can be used in an appropriate method to predict tensile properties, hardness and conductivity, but it is found that the quench factor could not be used to predict elongation because of its strong dependency on grain size [55].

The quench factor can be calculated relatively easily from time – temperature curves and the equation describing the time-temperature-transformation curve (TTT curve) derived for the alloy of interest. The TTT curve is usually described in the form [27, 55]:-

$$C_T(T) = -K_1\, K_2\, \exp\left(\frac{K_3\, {K_4}^2}{RT(K_4 - T)^2}\right) \exp\left(\frac{K_5}{RT}\right)$$

where:

$C_T(T) =$ The critical time required to form a constant amount of a new phase or reduce the hardness by a specified amount. (The locus of the critical time values as a function of temperature formed the TTT curve.)

K_1 = constant which equals the natural logarithm of the fraction untransformed during quenching.

K_2 = constant related to the reciprocal of the number of nucleation sites.

K_3 = constant related to the energy required to form a nucleus.

K_4 = constant related to the solvus temperature.

K_5 = constant related to the activation energy of diffusion.

R = 8.3143/ J K^{-1} mol^{-1}.

T = temperature/ °C.

The constants K_1 , K_2 , K_3 , K_4 and K_5 define the shape of the TTT curve.

While quench factor analysis appears to be an excellent technique of correlating cooling curves with metallurgical response, it suffers from a lack of availability of the constants for the C_T function, all of them must be measured [17, 55].

1.3 Objective of the study

The main objectives of the study are:

1. To investigate and understand the role of the quenchant type and quenchant temperature on the cooling rate and the heat transfer coefficient, and consequent effects on the microstructure and the properties of steel.
2. To develop a reliable probe design to determining the accurate surface heat-transfer coefficient for steels as a function of surface temperature, using measured temperature profiles.
3. To investigate the effect of quenching parameters on the quench factor and the resulting hardness.
4. To develop a neural network model to predict the thermal conductivity of steels as a function of temperature, along with meaningful estimates of the accuracy of the predictions.
5. To develop a computer program using the control volume method to simulate the quenching process and calculate the temperature profile inside the steel. The boundary conditions for the modelling program are the estimated heat transfer coefficient and the predicted thermal conductivity.

1.4 Research work layout

The research work presented in this thesis is in seven chapters.

Chapter 1, which has been already introduced, is an introduction and a thorough review of the relevant literature and previous work done in the field

of quenching. The literature review focuses on cooling curve analysis as a tool to evaluate the cooling power of quenchants, and on the type of probes available to measure cooling curves.

Chapter 2 deals with the quenching process and its stages, and the mechanisms of heat transfer during these stages, and the parameters that affect these mechanisms. Starting with the relevant literature and showing how the knowledge can be used to develop the models, this chapter also describes material physical properties (specific heat and heat conductivity) as a function of temperature and the mathematical description of quenching process.

Chapter 3 is an overview of the thermal conductivity and the problems of modelling complex properties and describes the bayesian neural network model for thermal conductivity for steels and the data used in its creation and also its predictive ability.

In chapter 4, the experimental work, the design of a probe and quenching system to measure heat transfer coefficient is described, along with experimental details such as the probe preparation and the methods for analysing the collected data.

In chapter 5 the results of the experimental work and associated discussion are presented. The results illustrate how the inverse method is used to calculate the heat transfer coefficient using probe technique for different steels and for a variety of quenchants at different temperatures. The results also illustrate the effect of quenchant type and quenchant temperature on cooling rate, heat-transfer coefficient, quench factor, and estimated as-quenched hardness. A case study is presented to demonstrate the modelling

technique described in chapter 4 and to assess the applicability of the calculated heat transfer coefficient to other samples with different dimensions.

Chapter 6 includes conclusions, recommendations and suggestions for the future work.

Chapter 2

Theoretical background

2.1 Quenching and quenching stages

Quenching refers to the process of cooling metal parts from the austenitizing or solution treating temperature (typically from within the range of 815 to 870 °C for steel) sufficiently rapidly to avoid the formation of such products as ferrite, pearlite and bainite [17, 62]. The quenching process is therefore defined as the controlled extraction of heat, the primary function of the quenchant being to control the heat transfer rates from the part and produce the desired hardness, strength and toughness. The quenchant should also minimize distortion and residual stresses by ensuring uniformity over the whole of the sample. The physical properties obtained are directly related to cooling rates. Quenchants can be liquid, solid, or gas [63].

Methods for determining the ability of a quenchant to extract heat can be divided into two broad categories; mechanical and thermal. The mechanical procedures usually employ hardness measurements or etching procedures applied to quenching parts. These methods determine the depth of martensite

formation in the steel concerned after quenching under standardized conditions. Thermal techniques involve measuring the time required to cool between specified temperatures, determining the rate of cooling in a standard specimen, or defining by some other thermal means the ability of quenchant to extract heat [18].

The examination of quenching performance by cooling curve analysis is becoming increasingly popular and perhaps the most informative method of characterizing a quenchant. The cooling curve produced when a component, initially at a temperature well above the boiling point of the quenchant, is introduced into the liquid, is much more complex than that suggested by Newton's law of cooling; heat transfer is controlled by different cooling mechanisms [1, 64] as shown in figure 2-1. The maximum heat transfer occurs during the nucleate boiling stage.

2.1.1 Stage-A Heat Removal

The first stage `A´ of cooling is characterized by the formation of a quenchant-vapour blanket around the part; when the hot steel first encounters the liquid, vapour bubbles are nucleated, and grow, at the hot interface. Initially, the nucleation and growth rates are so high that the surface of the steel is covered with a continuous vapour film [65].

The vapour blanket is maintained while the supply of heat from the interior of the part to the surface exceeds the amount of heat needed to evaporate the quenchant. Relatively slow cooling occurs during this period because the vapour envelope acts as an insulator, and cooling occurs principally by radiation through the vapour film. The temperature above

which a total vapour blanket is maintained is called the characteristic temperature of the liquid, also known as the Leidenfrost temperature [17, 18].

The vapour blanket stage is not usually present in parts quenched in aqueous solutions containing more than about 5 wt% of an ionic material such as potassium chloride, lithium chloride, sodium hydroxide, or sulphuric acid. When the saturated salt crystals deposit on the metal are heated by the metal, water escapes from them by microscopic explosions thereby breaking the vapour blanket and facilitating the nucleation of vapour bubbles. As a result, the duration of the vapour blanket stage is shortened or sometimes this stage does not occur at all and is replaced by the boiling stage `A´. Conversely, heat transfer in gas quenchants such as air and inert gases occurs exclusively by a vapour blanket mechanism [1, 66].

2.1.2 Stage-B Heat Removal

The highest cooling rates occur in stage B or the nucleate boiling stage. As the steel cools, the rate of nucleation and growth of the vapour bubbles becomes smaller, and, when a region of the vapour breaks from the surface under the buoyancy forces and rises in the liquid, fresh liquid is swept in to the region it occupied. This cold and fresh liquid heats to the boiling point and vapour begins to form again; upon reaching a certain size, this bubble breaks free. The process is repeated because in this stage the colder liquid is constantly brought into contact with the hot surface and vaporised, the steel cools the fastest, and high heat extraction rates are achieved [1, 67].

2.1.3 Stage-C Heat Removal

Stage C involves the cooling of the liquid and begins when the temperature of the steel surface reaches a point where liquid convection is sufficient to keep it from boiling. Below this temperature, boiling stops and cooling takes place by conduction and convection into the quenchant, and the rate of cooling again decreases. The cooling rates in this stage are dependent on the viscosity of the quenchant. All other factors being equal, cooling rates decrease with increasing viscosity.

Optimal quenching processes usually require maximum A and B stage cooling rates to avoid the pearlite transformation region and minimal C stage cooling rates because the tendency for distortion and cracking is more likely to happen in the temperatures where the martensite structure can formed [17, 67].

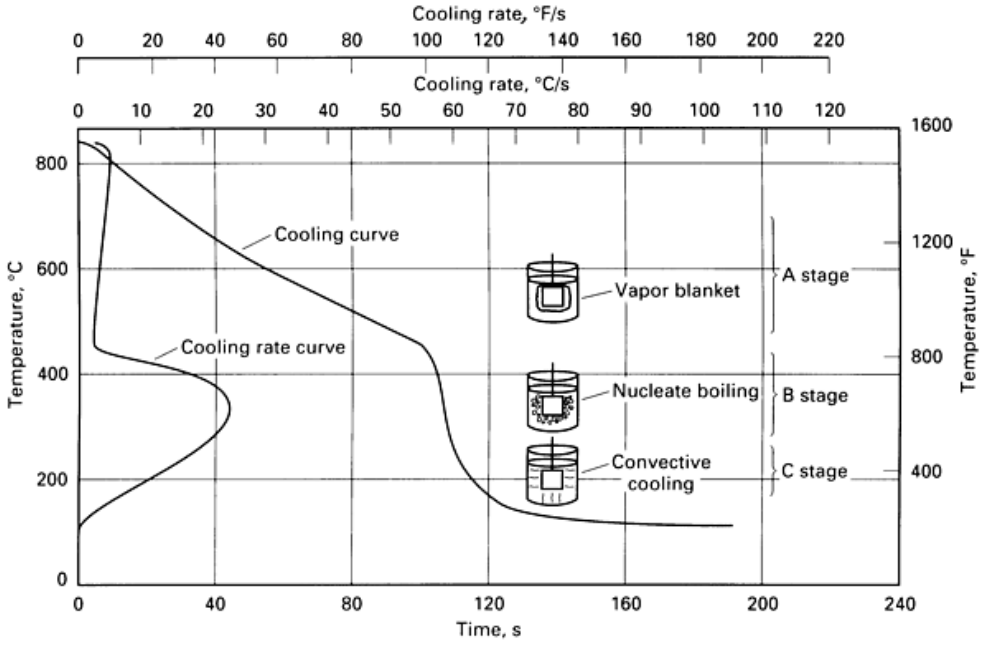

Figure 2-1: Cooling curve and cooling rate curve at the centre of a 25 mm diameter probe quenched with 95 °C water flowing at 0.25 m sec^{-1} [17].

2.2 Cooling curve analysis

The most useful way of accurately describing the complex mechanism of quenching is to develop a cooling curve for the quenching medium under controlled conditions. A cooling curve test simulates conditions of actual cooling in a test piece of the same metal of which the part is to be made during quenching into the test medium. The analysis of the resulting cooling curve yields quantitative heat transfer data as a function of temperature [18, 66].

The parameters obtained from cooling curves are:

- The maximum cooling rate ($\dot{T}_{max}$):
  Usually it is desirable for the $\dot{T}_{max}$ to occur at temperature in the region of the ferrite and pearlite transformation region if maximum hardness is desired, since this ensures the minimisation of ferrite and pearlite.

- The cooling rate at about 300 °C ($\dot{T}_{max}$):
  Cooling rates in the region where austenite transform into martensite should be minimized to reduce the potential for cracking and distortion [1, 17].

2.2.1 Effect of quenching parameters on cooling curve

Various factors in addition to work piece configuration may affect the heat extracting potential of quenching liquid, including:

2.2.1.1 Quenchant type

The purpose of the quenchant is to control heat transfer from the hot metal work piece. The type of quenchant used has a dramatic effect on cooling rate. Many materials and solutions have been used as quenchants for steels. The fastest quench rates are obtained using water or brine (water-salt solution). Slower, less drastic quenchants include the water based polymers, oil and salts. Very slow cooling can be obtained in air, inert gas atmospheres or vacuum [1, 18].

2.2.1.2 Quenchant temperature

The temperature of the quenchant obviously affects its ability to extract heat. However, it is not always true that a colder quenchant will give faster extraction. Water loses its cooling power as it approaches its boiling point, but this is not the case for oil, which becomes less viscous as the temperature increased. The reduced oil viscosity offsets any reduced quenching ability caused by the temperature rise.

Increasing the temperature of the work piece has relatively little effect on its ability to transfer heat to the quenching medium because of the large temperature difference with the quenching medium. The most noticeable change in ability to transfer heat probably comes from the more rapid oxidation of the test piece at higher temperatures; this can either increase or decrease the heat transfer capability, depending on the thickness of the oxide developed [18, 65].

2.2.1.3 Quenchant agitation

Agitation or forced circulation of the quenchant has a dramatic influence on heat transfer. It causes an earlier mechanical disruption of the vapour blanket in stage A and produces smaller, more frequently detached vapour bubbles during stage B. It can mechanically disrupt or dislodge gels and solids from the surface of the test piece or those suspended at the edge of the vapour blanket, thus producing faster heat transfer in stage C. Agitation also circulates cool liquid to replace the heated liquid surrounding the work piece. Agitation can be accomplished by mechanically moving the parts through the bath, pumping to recirculate the quenchant or mechanically agitating the fluid [1, 67].

2.2.2 Estimating as quenched hardness of steel from cooling curve

Quench factor analysis permits the direct correlation of the shape of the cooling curve with the appropriate property curve developed for the steel of interest.

The key foundational principle of quench factor analysis is the use of isothermal transformation kinetics to estimate transformation behaviour during continuous cooling. By representing a quenching curve as a series of consecutive isothermal transformation events and adding together the amount transformed during each isothermal step, the effect of temperature on transformation rate can be taken into account for virtually any stepped quenching or continuous cooling thermal path. Consequently, the effect of quench rate on properties can be modelled much more accurately than if an average quenches rate approach is taken. The use of isothermal data to make

non-isothermal transformation predictions is due to Scheil and Avrami [61, 68].

Quench factor analysis provides a single number, Q, which relates the cooling rate in a part and the transformation kinetics of the particular alloy being quenched. Cooling rates used in the analysis may be experimentally measured or calculated from heat transfer data.

Alloy hardening characteristics are described by the time – temperature – transformation (TTT) curve.

The basic hypothesis behind the quench factor concept is that the hardening behaviour of steel during continuous cooling can be predicted by dividing a cooling curve into discrete temperature – time increments and determining the ratio of the amount of time the steel was at each temperature divided by the amount of time required to obtain a specified amount of transformation at that temperature. The sum of the incremental quench factor values over the transformation range between the A_3 and the M_S temperatures is the quench factor, Q; this approach is usually referred to as the Avrami or additively rule.

Quench factors can be calculated relatively easily from digitally recorded time temperature curves (cooling curve) obtained in instrumented parts and the TTT-curve for the alloy of interest [56].

TTT curves were calculated for steel of composition Fe-0.16 C-0.16 Si-0.67 Mn wt% using MAP-STEEL-MUCG83 (figure 2-2) for the modelling of transformations in steels. This program allows calculations of kinetics for the solid state phase transformations from austenite to martensite, bainite, Widmanstätten ferrite, allotriomorphic ferrite, *etc*. [15].

The TTT diagram consists of two C-curves representing the initiation of transformation. The higher temperature C–curve is for reconstructive (diffusional) reactions such as allotriomorphic ferrite and pearlite. The lower C-curve is for displacive reactions such as Widmanstätten ferrite and bainite or acicular ferrite. When making a quench factor calculation, an incremental quench factor, q for each time step Δt in the transformation range is first calculated using the following equation [17, 18]:

$$q = \frac{\Delta t}{t_c} \tag{2.1}$$

where:

$t_c =$ the critical time required to obtain the first detectable amount of ferrite, pearlite, or bainite typically 0.1 or 0.5% (the locus of the critical time is the start of transformation C-curve).

$\Delta t =$ the time step used in data acquisition.

The incremental quench factor values are summed over the transformation range between A_{r3} and M_S to produce the cumulative quench factor, Q, according to the equation:

$$Q = \sum_{T=M_S}^{T=A_{r3}} \frac{\Delta t}{t_c} \tag{2.2}$$

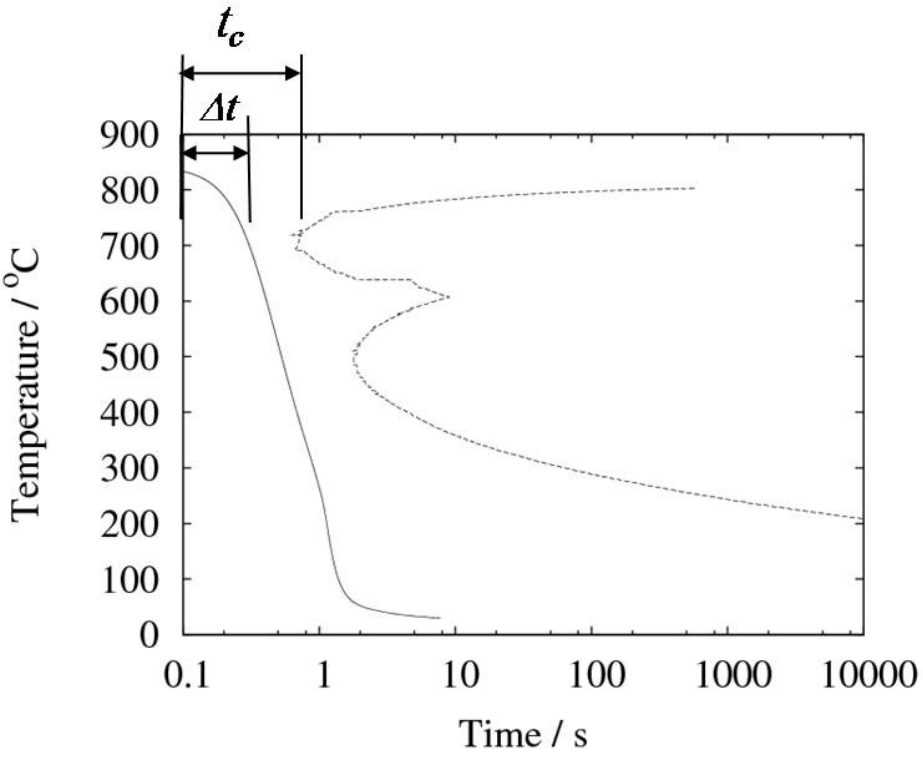

Figure 2-2: Calculation of quench factor from cooling curve and C-Curve for Fe-0.16 C-0.16 Si-0.67 Mn wt% steel.

The cumulative quench factor reflects the heat extraction characteristics as a function of the quenchant type, quenchant agitation, and quenchant temperature over the transformation range of the steel being quenched. These factors include section thickness, agitation, and surface finish effects on cooling rate as well as the transformation rate of the alloy. The calculation process is illustrated schematically in figure 2-2.

The quench factor can be used to estimate the as-quenched hardness in steel using the following equation [56, 59, 60, 61]:

$$Hp = H_{min} + (H_{max} - H_{min})\exp(K_1 Q) \tag{2.3}$$

where:

$Hp =$ the predicted hardness.

$H_{max} =$ the maximum hardness for alloy (martensite hardness).

$H_{min} =$ the minimum hardness for alloy (ferrite-pearlite hardness).

$K_1 =$ the constant which equals the natural logarithm of the volume fraction austenite not transformed above the M_S during cooling; that is, the fraction defined by the C-curve, typically ln 0.995 = -0.00501

$Q =$ the quench factor.

The critical value of the quench factor is the maximum value that will produce the desired hardness in the particular steel being quenched.

Maximum hardness and strength values are obtained with low quench factors but minimum quenching stresses are obtained with high quench factors. Minimum residual stress and distortion consistent with the quench factor is just below the critical value.

The goal of quench factor analysis is to interrelate alloy hardenability and quenching variables, and allow empirical predictions to be made about hardness and strength in specific alloys and specific locations in parts. Once a quench factor is established that will provide the required hardness and strength. A quench should be selected and used in such a way that thermal stress and the tendency for distortion and quench cracking is minimized.

2.3 Quenching as a heat transfer process

2.3.1 Unsteady state heat transfer

The heat transfer is unsteady when a temperature at any given location in a system changes with time.

The phenomenon of unsteady state heat transfer occurs often in industrial processes, such as quenching of metals. In these applications, heat transfer is a dynamic, time dependent process.

The unsteady problems are formulated according to *a lump* or *a distributed system analysis*. Convective heat transfer through boundaries is important in the formulation and solution of conduction problems. The dimensionless form of the boundary condition yields the Biot number, Bi, which is the ratio of the external conductance to internal conductance [69].

$$Bi = \frac{R_{cond}}{R_{conv}} = \frac{h(V|A_S)}{k} = \frac{h\,L_c}{k} \tag{2.4}$$

h = heat transfer coefficient / W m^{-2} °C^{-1}.

k = Thermal conductivity of the quenched part / W m^{-1} °C^{-1}.

L_c = Characteristic length for the part / m.

A_S = Surface area of the part being quenched / m^2.

V = Volume of the part / m^3.

When the internal resistance is negligible (or when the external conductance is large), $k / L_c \rightarrow \infty$ and $B_i \rightarrow 0$ this case corresponds to a small L or large k , and permits the omission of the spatial temperature variation

perpendicular to the boundary having this condition; thus it leads to *a lumped system analysis.*

When the internal and external resistances (or conductance) are comparable, the general boundary condition cannot be simplified and the problem must be solved in terms of this condition. This case requires *the distributed system approach.*

The calculation of heat transfer coefficients through the use of the lumped sum model make it possible to estimate the amount of time a system takes to reach steady state conditions [69, 70].

2.3.2 Heat transfer during quenching

Heat removal from parts during quenching can be mathematically described in terms of the effective interface heat transfer coefficient.

A quenchant must impart a sufficiently high interface heat transfer coefficient to produce a cooling rate that will minimize transformation of austenite to ferrite or pearlite and yield the desired amount of martensite or bainite.

The interface heat transfer coefficient is defined as [70, 71]:

$$h = \frac{q}{A(T_S - T_\infty)} \tag{2.5}$$

where:

q = Heat flow from the part to the quenchant.

A = Part area.

T_S = The part surface temperature.

T_∞ = The environment temperature.

The interface heat transfer coefficient under conditions of interest can be determined by recording a cooling curve using a thermocouple located in the centre of cylindrical test probes with particular dimensions. The cooling rate can be determined over a particular temperature range from the cooling curve, to estimate the interface heat transfer coefficient. That provides the effective interface heat transfer coefficient over the temperature range of interest.

The benefit of knowing or experimentally determining interface heat transfer coefficients produced by a specific quenchant under known conditions is that these values can be used with confidence in finite element or finite difference heat transfer calculations to model the thermal behaviour of parts or components that have not actually been instrumented. These calculated cooling curves can then be used to estimate the as-quenched hardness in these locations.

2.3.3 Determination of heat transfer coefficient using inverse method

In the numerical simulation of quenching process, the temperature field is usually determined using the heat transfer equation. It is then necessary to know the various coefficients, the boundary conditions, and the initial condition, in order to reach the solution. We look in that case for the response of the system with a known initial temperature field to the heat transfer limited by known boundary conditions. The surface heat transfer coefficient is the

most important boundary condition and key parameter for process simulation [42, 56].

It is also possible, however, to reverse the problem. The inverse problem is defined as one in which the sought objective or the value to be determined is unattainable by direct experiments, and conclusions concerning their characteristics are drawn following indirect measurements of parameters. The boundary conditions of heat transfer are sought in the inverse method [73]. The process effects can be determined by the temperature changes at a point located at the geometric centre for a probe, where the probe dimensions can be determined using the lumped capacitance theory [74, 75].

Temperature history measurement is used as an input to an inverse heat conduction model to estimate the heat transfer coefficient at the metal /quenchant interface. The non-linear surface heat transfer coefficients include the coupled effects between phase transformation and temperature [43, 76].

2.3.3.1 Lumped Capacitance Models

In a quenching process heat transfer is a dynamic, time dependent process. When the thermal properties of the body under investigation and the thermal conditions of its surface are such that the temperature inside the body varies uniformly in time and the body is at any moment almost isothermal, the lumped capacitance method in this case is a convenient, simple and accurate tool of thermal analysis. If the part is immersed at $t = 0$ in a cooling fluid with $T_\infty < T_i$, the temperature inside the body (T_i) decreases smoothly and monotonously, to reach eventually the equilibrium value (T_∞).

Heat is transferred inside the body by conduction and by convection from the body to the surrounding fluid reservoir. If the thermal resistance of the body is small as compared with that of the fluid ($B_i \leq 0.1$), then the instantaneous temperature field inside the body is uniform, and the internal temperature gradients are negligibly small. The energy balance equation then takes the particular form [70, 71, 77]:

$$-E_{out} = E_{st} \tag{2.6}$$

$E_{st} =$ the change in the thermal energy storage in the solid. The equation describing this process is:

$$E_{st} = \rho V C_P(T) \frac{dT}{dt} \tag{2.7}$$

$E_{out} =$ Thermal energy transferred between the part and the fluid surrounding it. The equation used to describe this mechanism is:

$$E_{out} = hA_S(T_S - T_\infty) \tag{2.8}$$

This means:

$$-hA_S(T_S - T_\infty) = \rho V Cp(T) \frac{dT}{dt} \tag{2.9}$$

where:

$T_S =$ Temperature of the part surface / °C.

T_∞ = Temperature of the quenchant / °C.

ρ = Material density / kg m^{-3}.

$C_p(T) =$ Specific heat / J kg^{-1} °C^{-1}.

T = Temperature / °C.

The above equation can be manipulated to directly solve for h:

$$h = \frac{\rho V C_p(T)\frac{dT}{dt}}{A_S(T_S - T_\infty)} \tag{2.10}$$

2.3.3.2 Applicability of lumped capacity analysis

The ratio of the internal (conductive) resistance to the external (convective) resistance from a solid exchanging heat with a fluid can be denoted by the Biot number, *Bi*.

This dimensional quantity plays an important role in the evaluation of the internal conduction heat transfer process with surface convection conditions, and it may be used to assess the validity of the lumped capacitance method for a particular case. Essentially, $Bi \leq 0.1$ means that the internal conduction thermal resistance of the body is much smaller than that due to convection.

Hence, the lumped capacitance model is consistent and can be used safely. Such an analysis may be expected to yield reasonable estimates within about 5% percent [11, 12, 77].

2.4 Material physical properties

Both thermal conductivity *(k)* and specific heat *(C_p)* values of the material need to be expressed as a function of temperature during the quenching process in order to increase the accuracy of the calculations.

The density (ρ) is assumed as constant (7858 kg m^{-3}) because the variation of its volume due to expansion during the quench is small [11, 71].

2.4.1 Specific heat capacity

Specific heat capacity varies with both temperature and structure. In particular it tends to show anomalously high values near the temperatures at which magnetic transformations occur. The position of the peaks due to the high values of this property depend upon the temperature at which transformation occur [70, 78].

Thermodynamic calculations were carried out with MTDATA software to predict the equilibrium phase fraction (figure 2- 3) and to estimate the specific heat of Fe-0.16 C-0.16 Si-0.67 Mn wt% as a function of temperature. During the calculation two conditions were used, first, only austenite was allowed to exist. The data for the specific heat can be fitted to one polynomial equation to cover the entire temperature range as shown in figure 2- 4 (1200 °C > T > 0°C). This equation was used to calculate the surface heat transfer coefficient during the quenching process for the probe, which is expected to remain as austenite until the M_s temperature is reached.

$$C_p(T) = 478.3 - 0.141\,T \qquad \text{J kg}^{-1}\text{ K}^{-1} \qquad (2.11)$$

In a second calculation, austenite ferrite and cementite were allowed to exist. The data for the specific heat can be fitted by a fifth order polynomial to cover the entire temperature range as shown in figure 2- 4 (1200 °C > T > 0°C). This equation was used in the program to calculate the temperature distribution inside the sample. In both cases the specific heat capacity started to be similar after M_S temperature. In both cases also, the discontinuity in the heat capacity due to transformations was omitted, which represents a much smaller amount of energy when compared to the heat released by the cooling process.

$$C_p(T) = 487.6 - 1.57\,T + 2 * 10^{-2}\,T^2 - 7.69 * 10^{-5}\,T^3 + 1.2 * 10^{-7}\,T^4 - 6.67 * 10^{-11}\,T^5 \qquad \text{J kg}^{-1}\,\text{K}^{-1} \qquad (2.12)$$

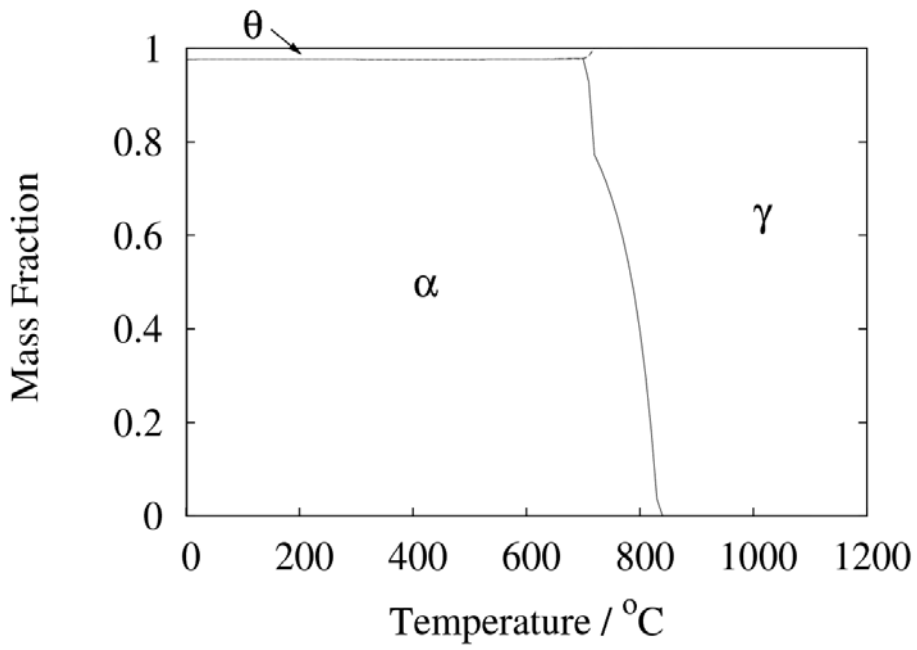

Figure 2-3: Evolution of equilibrium phase fraction using MTDATA calculation for Fe- 0.16 C- 0.16 Si- 0.67 Mn wt% steel. Only ferrite, austenite, cementite were allowed to exist.

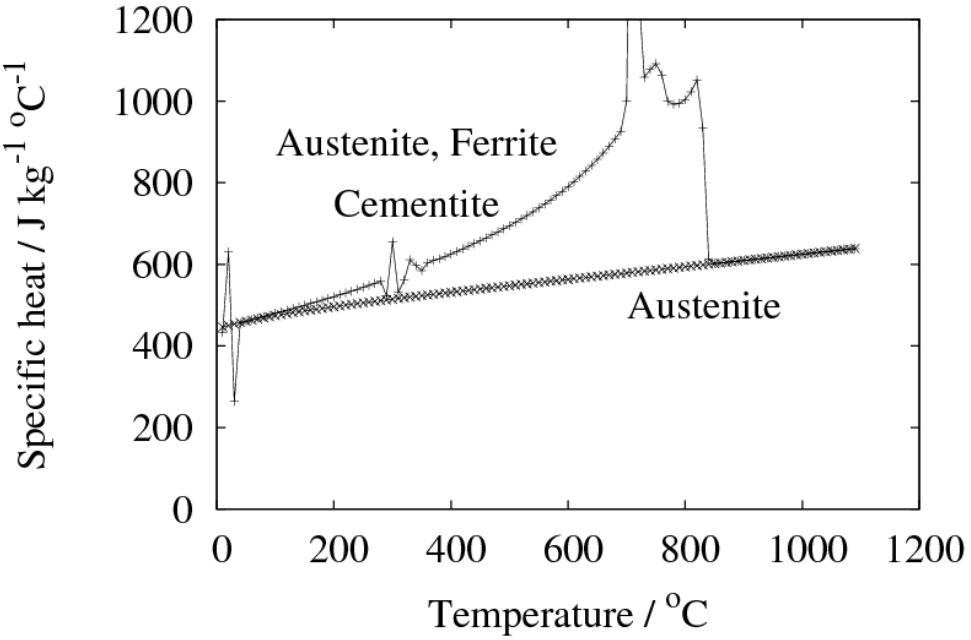

Figure 2-4: Calculated specific heat capacity of Fe- 0.16 C- 0.16 Si-0.67 Mn wt% steel as a function of temperature using MTDATA.

2.4.2 Thermal conductivity

Thermal conductivity is a function of the composition and the structure of the material. It generally decreases with temperature; austenite has the lowest conductivity [64]. Figure 2-5 shows the dependency of thermal conductivity on temperature as predicted using a neural network model [79] as will be explained in chapter 3, which can be summarized by a third order polynomial equation to indicate the variation of thermal conductivity with temperature. This equation covers the temperature range shown in the figure (1000 °C > T > 0°C).

$$k(T) = 51.76 - 9.88 * 10^{-3} T - 5.52 * 10^{-5} T^2 + 4.16 * 10^{-8} T^3 \quad \text{W m}^{-1}\text{K}^{-1} \qquad (2.13)$$

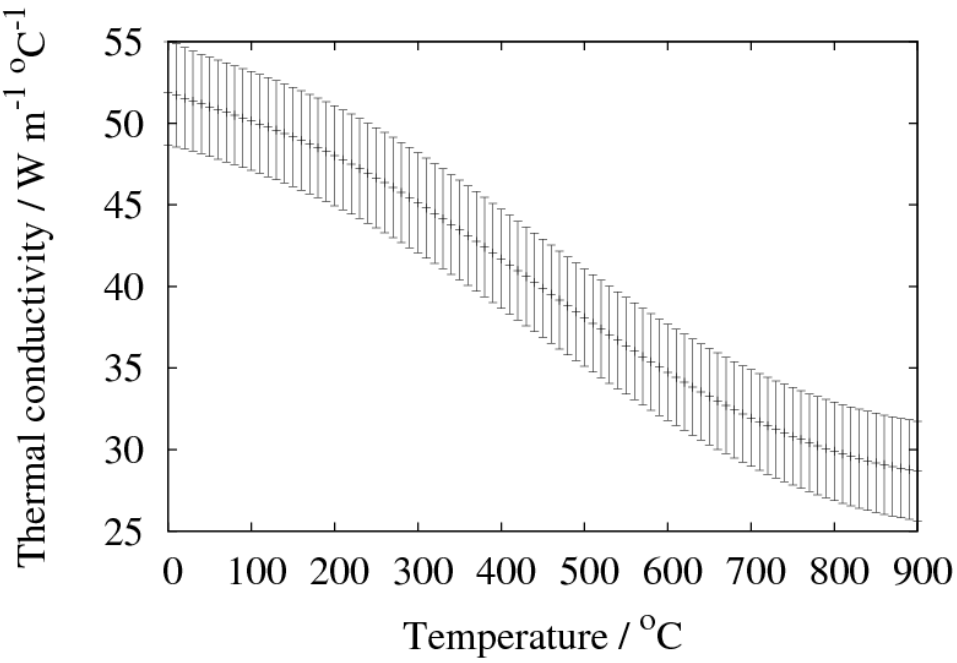

Figure 2-5: Calculated thermal conductivity for Fe- 0.16 C- 0.16 Si- 0.67 Mn wt% steel as a function of temperature using the thermal conductivity neural network model.

2.5 Theoretical and experimental investigation

The information about a quenching process can be obtained by two main methods, experimental investigation and theoretical calculation [12].

2.5.1 Experimental investigation

The most reliable information about a physical process in often given by actual measurement. An experimental investigation involving full scale equipment is prohibitively expensive and often impossible. The alternative then is to perform experiments on small scale models. The resulting information, however, must be extrapolated to large scale.

2.5.2 Theoretical calculation

Theoretical prediction works out the consequences of a mathematical model, rather than those of an actual physical model. For the quenching processes of interest here, the mathematical model mainly consists of a set of differential equations.

2.5.3 Advantages of computer model over experiments

- An important advantage of computational prediction is its low cost in most applications; the cost of a computer run is many orders of magnitude lower than that of a measurement.
- A computer solution of a problem can give detailed and complete information. It can provide the values of all the relevant variables through the domain of interest. Obviously, no experimental study can be expected to measure the distributions of all variables over the entire domain. For this reason, even when an experiment is performed, there is a great value in obtaining a companion computer solution to supplement the experimental information [12].

2.6 Mathematical description of quenching process

The formulation of a quenching process involves translating the problem into a mathematical form, usually differential equations.

Formulation of heat conduction in three dimensions is based on differential heat balance over a suitably chosen small volume element in the system. One of the three common coordinate systems-the rectangular Cartesian, the cylindrical polar, and the spherical polar may be selected

depending upon the geometrical shape of the body in which conduction or diffusion of heat is taking place [70].

2.6.1 Control Volume Formulation

The basic idea of the control volume formulation is easy to understand and leads itself to direct physical interpretation. The calculation domain is divided into a number of non overlapping control volumes such that there is one control volume surrounding each grid point. The differential equation is integrated over each of these.

The most attractive feature of the control volume formulation is that the resulting solution would imply that the integral conservation of quantities such as mass, momentum, and energy is exactly satisfied over any group of control volumes and, of course, over the whole calculation domain. This characteristic exists for any number of grid points; not just in a limiting sense when the number of grid points becomes large. Thus, even the coarse-grid solution would exhibit exact integral balances [70].

2.6.2 Mathematical formulation and heat balance

The cylindrical polar coordinate system has been used for the mathematical formulation. The choice of the coordinate axes and the cylindrical body is shown in figure 2-6; also shown in the same figure is the small annular cylindrical element of radius r_m, thickness Δr, height Δz, and polar angle $\Delta \emptyset$. The heat balance has been taken over this small element. There are six heat output terms for the six surfaces of the volume element and the accumulation term, there is no generation term in heat balances because there is no heat source.

The heat balance equation is written as [12, 70, 71]:

$$\left(\begin{array}{l}\text{The change in the thermal}\\ \text{energy storage of the volume}\\ \text{element during } \Delta t\end{array}\right) = \left(\begin{array}{l}\text{Heat transferred out of the}\\ \text{volume element from all of}\\ \text{its sides during } \Delta t\end{array}\right)$$

$$E_{st} = \sum_{all\ sides} Q \tag{2.14}$$

$$E_{st} = \rho V C_p(T) \frac{dT}{dt} \tag{2.6}$$

$$\sum_{all\ sides} Q = q_s + q_n + q_e + q_w + q_t + q_b \tag{2.15}$$

$$\rho V C_p \frac{T^{p+1}_{(i,j,k)} - T^{p}_{(i,j,k)}}{\Delta t} = q_s + q_n + q_e + q_w + q_t + q_b \tag{2.16}$$

where $T^{p}_{(i,j,k)}$ and $T^{p+1}_{(i,j,k)}$ are the temperatures of the nodes at times $t = p\,\Delta t$ and $t = (p+1)\,\Delta t$ respectively. $T^{p+1}_{(i,j,k)} - T^{p}_{(i,j,k)}$ represents the temperature change of the node during the time interval (Δt).

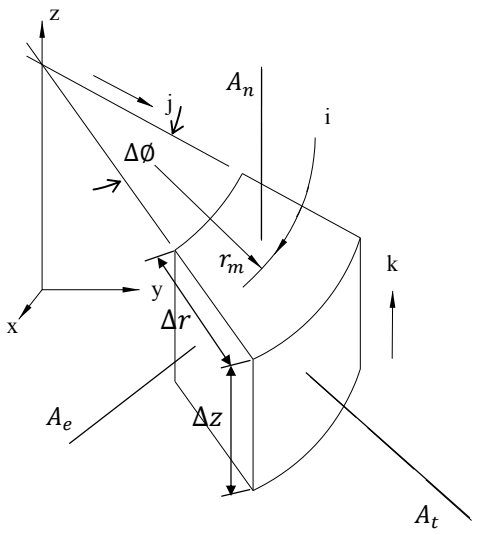

Figure 2-6: The volume element for the cylindrical coordinate system.

A_s = the area in the south direction = $r_m \Delta\emptyset \Delta r$

A_n = the area in the north direction = $r_m \Delta\emptyset \Delta r$

A_e = the area in the east direction = $\Delta r \Delta z$

A_w = the area in the west direction = $\Delta r \Delta z$

A_t = the area in the rear direction = $\left(r_m + \frac{\Delta r}{2}\right) \Delta\emptyset \Delta z$

A_b = the area in the front direction = $\left(r_m - \frac{\Delta r}{2}\right) \Delta\emptyset \Delta z$

ΔV = volume elements = $r_m \Delta\emptyset \Delta r \Delta z$

q_s = Heat conduction in the south direction of the node.

$$q_s = kA_s \frac{dT}{\Delta z} = \frac{kA_s}{\Delta z}\left(T^P_{(i,j,k-1)} - T^P_{(i,j,k)}\right) \tag{2.17}$$

q_n = Heat conduction in the north direction of the node.

$$q_n = kA_n \frac{dT}{\Delta z} = \frac{kA_n}{\Delta z}\left(T^P_{(i,j,k+1)} - T^P_{(i,j,k)}\right) \tag{2.18}$$

q_e = Heat conduction in the east direction of the node.

$$q_e = kA_e \frac{dT}{r_m \Delta\emptyset} = \frac{kA_e}{r_m \Delta\emptyset}\left(T^P_{(i+1,j,k)} - T^P_{(i,j,k)}\right) \tag{2.19}$$

q_w = Heat conduction in the west direction of the node.

$$q_w = kA_w \frac{dT}{r_m \Delta\emptyset} = \frac{kA_w}{r_m \Delta\emptyset}\left(T^P_{(i-1,j,k)} - T^P_{(i,j,k)}\right) \tag{2.20}$$

q_t = Heat conduction in the rear direction of the node.

$$q_t = kA_t \frac{dT}{\Delta r} = \frac{kA_t}{\Delta r}\left(T^P_{(i,j+1,k)} - T^P_{(i,j,k)}\right) \tag{2.21}$$

$q_b =$ Heat conduction in front direction of the node.

$$q_b = kA_b \frac{dT}{\Delta r} = \frac{kA_b}{\Delta r}\left(T^P_{(i,j-1,k)} - T^P_{(i,j,k)}\right) \tag{2.22}$$

Substitute these equations in the main equation (2.16):

$$\frac{kA_s}{\Delta z}\left(T^P_{(i,j,k-1)} - T^P_{(i,j,k)}\right) + \frac{kA_n}{\Delta z}\left(T^P_{(i,j,k+1)} - T^P_{(i,j,k)}\right) + \frac{kA_e}{r_m \Delta \emptyset}\left(T^P_{(i+1,j,k)} - T^P_{(i,j,k)}\right) + \frac{kA_w}{r_m \Delta \emptyset}\left(T^P_{(i-1,j,k)} - T^P_{(i,j,k)}\right) + \frac{kA_t}{\Delta r}\left(T^P_{(i,j+1,k)} - T^P_{(i,j,k)}\right) + \frac{kA_b}{\Delta r}\left(T^P_{(i,j-1,k)} - T^P_{(i,j,k)}\right) = \rho \Delta V C_p \frac{T^{p+1}_{(i,j,k)} - T^p_{(i,j,k)}}{\Delta t} \tag{2.23}$$

Dividing both sides by $\rho \Delta V C_p$ and substituting $\alpha = \frac{k}{\rho C_p}$ results:

$$a_s\left(T^P_{(i,j,k-1)} - T^P_{(i,j,k)}\right) + a_n\left(T^P_{(i,j,k+1)} - T^P_{(i,j,k)}\right) + a_e\left(T^P_{(i+1,j,k)} - T^P_{(i,j,k)}\right) + a_w\left(T^P_{(i-1,j,k)} - T^P_{(i,j,k)}\right) + a_t\left(T^P_{(i,j+1,k)} - T^P_{(i,j,k)}\right) + a_b\left(T^P_{(i,j-1,k)} - T^P_{(i,j,k)}\right) = \frac{T^{p+1}_{(i,j,k)} - T^P_{(i,j,k)}}{\Delta t} \tag{2.24}$$

where

$\alpha =$ thermal diffusivity $= \frac{k}{\rho C_p}$ (units m^2/s)

$$a_s = \frac{\alpha A_s}{\Delta z \Delta V}, \qquad a_n = \frac{\alpha A_n}{\Delta z \Delta V}, \qquad a_e = \frac{\alpha A_e}{r_m \Delta \emptyset \Delta V}$$

$$a_w = \frac{\alpha A_w}{r_m \Delta \emptyset \Delta V}, \qquad a_t = \frac{\alpha A_t}{\Delta r \Delta V}, \qquad a_b = \frac{\alpha A_b}{\Delta r \Delta V}$$

This can be re-arranged to:

$$T_{(i,j,k)}^{p+1} = T_{(i,j,k)}^{p} + \Delta t\big[a_s T_{(i,j,k-1)}^{P} - a_s T_{(i,j,k)}^{P} + a_n T_{(i,j,k+1)}^{P} - a_n T_{(i,j,k)}^{P} + a_e T_{(i+1,j,k)}^{P} - a_e T_{(i,j,k)}^{P} + a_w T_{(i-1,j,k)}^{P} - a_w T_{(i,j,k)}^{P} + a_t T_{(i,j+1,k)}^{P} - a_t T_{(i,j,k)}^{P} + a_b T_{(i,j-1,k)}^{P} - a_b T_{(i,j,k)}^{P}\big] \quad (2.25)$$

where;

$$a = a_s + a_n + a_e + a_w + a_t + a_b$$

Therefore the temperature change in one iteration for the internal node (node 1) is given by:

$$T_{(i,j,k)}^{p+1} = T_{(i,j,k)}^{p} + \Delta t\big(a_s T_{(i,j,k-1)}^{P} + a_n T_{(i,j,k+1)}^{P} + a_e T_{(i+1,j,k)}^{P} + a_w T_{(i-1,j,k)}^{P} + a_t T_{(i,j+1,k)}^{P} + a_b T_{(i,j-1,k)}^{P} - a T_{(i,j,k)}^{P}\big) \quad (2.26)$$

Only the final equations for the other nodes will be given in the section 2-6-3-2.

2.6.3 Initial condition and boundary nodes

Figure 2-7 shows the cylindrical shape of the part and the associated initial and boundary conditions.

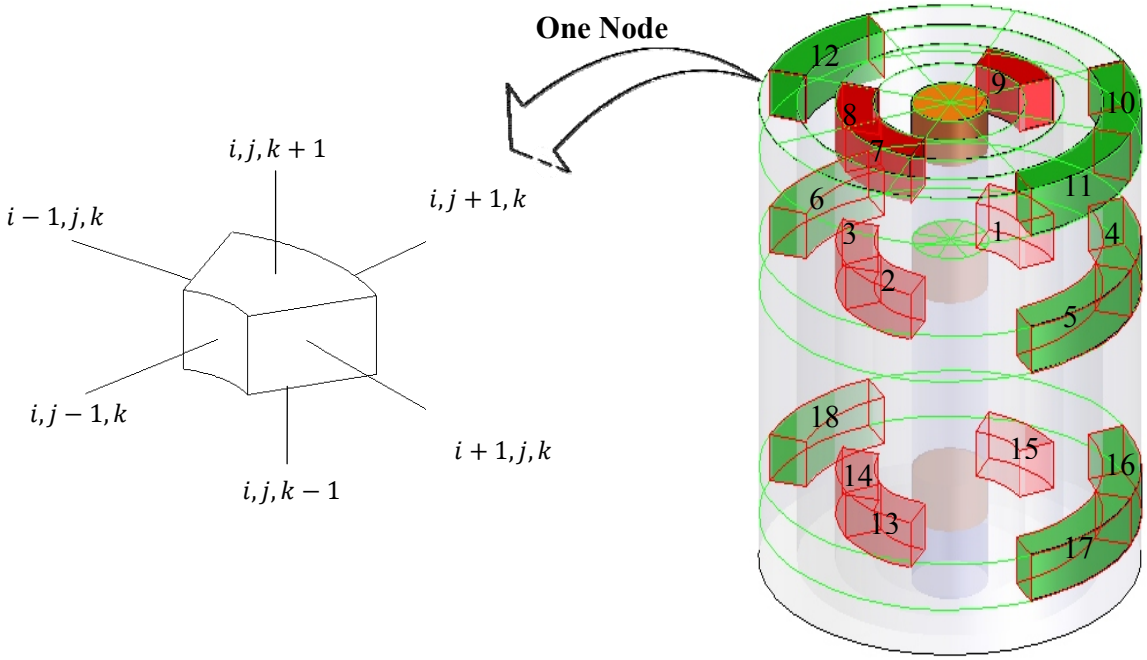

Figure 2-7: The cylindrical shape of the part and the boundary node distribution, nodes types are labelled 1- 18.

2.6.3.1 Initial condition

An initial condition dictates the temperature (or its distributions) within the body at zero time.

$t=0, \quad 1 < i < m, \quad 1 < j < n, \quad 1 < k < f;$

$T = T_{initial\ temperature}$ = quenching temperature.

2.6.3.2 Boundary conditions

Boundary nodes specify the temperatures at the boundaries enclosing the body (figure 2-7).

Node 2:

For the conditions $i = 1, \quad n > j > 1, \quad f > k > 1$

The temperature of the node after one time interval (Δt) is:

$$T_{(i,j,k)}^{p+1} = T_{(i,j,k)}^{p} + \Delta t\big(a_s T_{(i,j,k-1)}^{P} + a_n T_{(i,j,k+1)}^{P} + a_e T_{(i+1,j,k)}^{P} + a_w T_{(m,j,k)}^{P} + a_t T_{(i,j+1,k)}^{P} + a_b T_{(i,j-1,k)}^{P} - a T_{(i,j,k)}^{P}\big) \quad (2.27)$$

and the volume element is given by:

$$\Delta V = r_m \Delta \emptyset \Delta r \Delta z$$

Node 3:

For the conditions $i = m, \quad n > j > 1, \quad f > k > 1$

The temperature of the node after one time interval *(Δt)* is:

$$T_{(i,j,k)}^{p+1} = T_{(i,j,k)}^{p} + \Delta t\big(a_s T_{(i,j,k-1)}^{P} + a_n T_{(i,j,k+1)}^{P} + a_e T_{(1,j,k)}^{P} + a_w T_{(i-1,j,k)}^{P} + a_t T_{(i,j+1,k)}^{P} + a_b T_{(i,j-1,k)}^{P} - a T_{(i,j,k)}^{P}\big) \quad (2.28)$$

and the volume element is given by:

$$\Delta V = r_m \Delta \emptyset \Delta r \Delta z$$

Node 4:

For the conditions $i = 1, \quad j = n, \quad f > k > 1$

The temperature of the node after one time interval *(Δt)* is:

$$T_{(i,j,k)}^{p+1} = T_{(i,j,k)}^{p} + \Delta t\big(a_s T_{(i,j,k-1)}^{P} + a_n T_{(i,j,k+1)}^{P} + a_e T_{(i+1,j,k)}^{P} + a_w T_{(m,j,k)}^{P} + a_{t(Convection)} T_{out} + a_b T_{(i,j-1,k)}^{P} - a T_{(i,j,k)}^{P}\big) \quad (2.29)$$

where the $a_{t(Convection)}$ and the volume element are given by:

$$a_{t(Convection)} = \frac{\alpha h A_t}{K \Delta V} \qquad \Delta V = r_m \Delta \emptyset \Delta r \Delta z$$

Node 5:

For the conditions $i = m, \quad j = n, \quad f > k > 1$

The temperature of the node after one time interval *(Δt)* is:

$$T_{(i,j,k)}^{p+1} = T_{(i,j,k)}^{p} + \Delta t\big(a_s T_{(i,j,k-1)}^{P} + a_n T_{(i,j,k+1)}^{P} + a_e T_{(1,j,k)}^{P} + a_w T_{(i-1,j,k)}^{P} + a_{t(Convection)} T_{out} + a_b T_{(i,j-1,k)}^{P} - a T_{(i,j,k)}^{P}\big) \quad (2.30)$$

where the $a_{t(Convection)}$ and the volume element are given by:

$$a_{t(Convection)} = \frac{\alpha h A_t}{K \Delta V} \qquad \Delta V = r_m \Delta \emptyset \Delta r \Delta z$$

Node 6:

For the conditions $m > i > 1, \quad j = n, \quad f > k > 1$

The temperature of the node after one time interval *(Δt)* is:

$$T_{(i,j,k)}^{p+1} = T_{(i,j,k)}^{p} + \Delta t\big(a_s T_{(i,j,k-1)}^{P} + a_n T_{(i,j,k+1)}^{P} + a_e T_{(i+1,j,k)}^{P} + a_w T_{(i-1,j,k)}^{P} + a_{t(Convection)} T_{out} + a_b T_{(i,j-1,k)}^{P} - a T_{(i,j,k)}^{P}\big) \quad (2.31)$$

where the $a_{t(Convection)}$ and the volume element are given by:

$$a_{t(Convection)} = \frac{\alpha h A_t}{K \Delta V} \qquad \Delta V = r_m \Delta \emptyset \Delta r \Delta z$$

Node 7:

For the conditions $i = 1, \quad n > j > 1, \quad k = f$

The temperature of the node after one time interval (Δt) is:

$$T_{(i,j,k)}^{p+1} = T_{(i,j,k)}^{p} + \Delta t\big(a_s T_{(i,j,k-1)}^{P} + a_{n(Convection)} T_{out} + a_e T_{(i+1,j,k)}^{P} + a_w T_{(m,j,k)}^{P} + a_t T_{(i,j+1,k)}^{P} + a_b T_{(i,j-1,k)}^{P} - a T_{(i,j,k)}^{P}\big) \quad (2.32)$$

where the $a_{n(Convection)}$ and the volume element are given by:

$$a_{n(Convection)} = \frac{\alpha h A_n}{K \Delta V} \qquad \Delta V = r_m \Delta \emptyset \Delta r \frac{\Delta z}{2}$$

Node 8:

For the conditions $i = m, \quad n > j > 1, \quad k = f$

The temperature of the node after one time interval (Δt) is:

$$T_{(i,j,k)}^{p+1} = T_{(i,j,k)}^{p} + \Delta t\big(a_s T_{(i,j,k-1)}^{P} + a_n T_{out} + a_e T_{(1,j,k)}^{P} + a_w T_{(i-1,j,k)}^{P} + a_t T_{(i,j+1,k)}^{P} + a_b T_{(i,j-1,k)}^{P} - a T_{(i,j,k)}^{P}\big) \quad (2.33)$$

where the $a_{n(Convection)}$ and the volume element are given by:

$$a_{n(Convection)} = \frac{\alpha h A_n}{K \Delta V} \qquad \Delta V = r_m \Delta \emptyset \Delta r \frac{\Delta z}{2}$$

Node 9:

For the conditions $m > i > 1, \quad n > j > 1, \quad k = f$

The temperature of the node after one time interval (Δt) is:

$$T_{(i,j,k)}^{p+1} = T_{(i,j,k)}^{p} + \Delta t\big(a_s T_{(i,j,k-1)}^{P} + a_n T_{out} + a_e T_{(i+1,j,k)}^{P} + a_w T_{(i-1,j,k)}^{P} + a_t T_{(i,j+1,k)}^{P} + a_b T_{(i,j-1,k)}^{P} - a T_{(i,j,k)}^{P}\big) \quad (2.34)$$

where the $a_{n(Convection)}$ and the volume element are given by:

$$a_{n(Convection)} = \frac{\alpha h A_n}{K \Delta V} \qquad \Delta V = r_m \Delta \emptyset \Delta r \frac{\Delta z}{2}$$

Node 10:

For the conditions $i = 1$, $j = n$, $k = f$

The temperature of the node after one time interval (Δt) is:

$$T_{(i,j,k)}^{p+1} = T_{(i,j,k)}^{p} + \Delta t\big(a_s T_{(i,j,k-1)}^{P} + a_n T_{out} + a_e T_{(i+1,j,k)}^{P} + a_w T_{(m,j,k)}^{P} + a_t T_{out} + a_b T_{(i,j-1,k)}^{P} - a T_{(i,j,k)}^{P}\big) \quad (2.35)$$

where the $a_{n(Convection)}$ and the volume element are given by:

$$a_{n(Convection)} = \frac{\alpha h A_n}{K \Delta V} \qquad \Delta V = r_m \Delta \emptyset \Delta r \frac{\Delta z}{2}$$

Node 11:

For the conditions $i = m$, $j = n$, $k = f$

The temperature of the node after one time interval (Δt) is:

$$T_{(i,j,k)}^{p+1} = T_{(i,j,k)}^{p} + \Delta t\big(a_s T_{(i,j,k-1)}^{P} + a_n T_{out} + a_e T_{(1,j,k)}^{P} + a_w T_{(i-1,j,k)}^{P} + a_t T_{out} + a_b T_{(i,j-1,k)}^{P} - a T_{(i,j,k)}^{P}\big) \quad (2.36)$$

where the $a_{t(Convection)}$ and the volume element are given by:

$$a_{t(Convection)} = \frac{\alpha h A_t}{K \Delta V} \qquad \Delta V = r_m \Delta \emptyset \Delta r \frac{\Delta z}{2}$$

Node 12:

For the conditions $m > i > 1$, $j = n$, $k = f$

The temperature of the node after one time interval (Δt) is:

$$T_{(i,j,k)}^{p+1} = T_{(i,j,k)}^{p} + \Delta t\big(a_s T_{(i,j,k-1)}^{P} + a_n T_{out} + a_e T_{(i+1,j,k)}^{P} + a_w T_{(i-1,j,k)}^{P} + a_t T_{out} + a_b T_{(i,j-1,k)}^{P} - a T_{(i,j,k)}^{P}\big) \quad (2.37)$$

where the $a_{n(Convection)}$ and the volume element are given by:

$$a_{n(Convection)} = \frac{\alpha h A_n}{K \Delta V} \qquad \Delta V = r_m \Delta \emptyset \Delta r \frac{\Delta z}{2}$$

Node 13:

For the conditions $i = 1$, $n > j > 1$, $k = 1$

The temperature of the node after one time interval (Δt) is:

$$T_{(i,j,k)}^{p+1} = T_{(i,j,k)}^{p} + \Delta t\big(a_s T_{out} + a_n T_{(i,j,k+1)}^{P} + a_e T_{(i+1,j,k)}^{P} + a_w T_{(m,j,k)}^{P} + a_t T_{(i,j+1,k)}^{P} + a_b T_{(i,j-1,k)}^{P} - a T_{(i,j,k)}^{P}\big) \quad (2.38)$$

where the $a_{s(Convection)}$ and the volume element are given by:

$$a_{s(Convection)} = \frac{\alpha h A_s}{K \Delta V} \qquad \Delta V = r_m \Delta \emptyset \Delta r \frac{\Delta z}{2}$$

Node 14:

For the conditions $i = m$, $n > j > 1$, $k = 1$

The temperature of the node after one time interval (Δt) is:

$$T_{(i,j,k)}^{p+1} = T_{(i,j,k)}^{p} + \Delta t\big(a_s T_{out} + a_n T_{(i,j,k+1)}^{P} + a_e T_{(1,j,k)}^{P} + a_w T_{(i-1,j,k)}^{P} + a_t T_{(i,j+1,k)}^{P} + a_b T_{(i,j-1,k)}^{P} - a T_{(i,j,k)}^{P}\big) \quad (2.39)$$

where the $a_{s(Convection)}$ and the volume element are given by:

$$a_{s(Convection)} = \frac{\alpha h A_s}{K \Delta V} \qquad \Delta V = r_m \Delta \emptyset \Delta r \frac{\Delta z}{2}$$

Node 15:

For the conditions $m > i > 1$, $n > j > 1$, $k = 1$

The temperature of the node after one time interval (Δt) is:

$$T_{(i,j,k)}^{p+1} = T_{(i,j,k)}^{p} + \Delta t\big(a_s T_{out} + a_n T_{(i,j,k+1)}^{P} + a_e T_{(i+1,j,k)}^{P} + a_w T_{(i-1,j,k)}^{P} + a_t T_{(i,j+1,k)}^{P} + a_b T_{(i,j-1,k)}^{P} - a T_{(i,j,k)}^{P}\big) \quad (2.40)$$

where the $a_{s(Convection)}$ and the volume element are given by:

$$a_{s(Convection)} = \frac{\alpha h A_s}{K \Delta V} \qquad \Delta V = r_m \Delta \emptyset \Delta r \frac{\Delta z}{2}$$

Node 16:

For the conditions $i = 1$, $j = n$, $k = 1$

The temperature of the node after one time interval (Δt) is:

$$T_{(i,j,k)}^{p+1} = T_{(i,j,k)}^{p} + \Delta t\big(a_s T_{out} + a_n T_{(i,j,k+1)}^{P} + a_e T_{(i+1,j,k)}^{P} + a_w T_{(m,j,k)}^{P} + a_t T_{out} + a_b T_{(i,j-1,k)}^{P} - a T_{(i,j,k)}^{P}\big) \quad (2.41)$$

where the $a_{s(Convection)}$ and the volume element are given by:

$$a_{s(Convection)} = \frac{\alpha h A_s}{K \Delta V} \qquad \Delta V = r_m \Delta \emptyset \Delta r \frac{\Delta z}{2}$$

Node 17:

For the conditions $i = m$, $j = n$, $k = 1$

The temperature of the node after one time interval (Δt) is:

$$T_{(i,j,k)}^{p+1} = T_{(i,j,k)}^{p} + \Delta t\big(a_s T_{out} + a_n T_{(i,j,k+1)}^{P} + a_e T_{(1,j,k)}^{P} + a_w T_{(i-1,j,k)}^{P} + a_t T_{out} + a_b T_{(i,j-1,k)}^{P} - a T_{(i,j,k)}^{P}\big) \quad (2.42)$$

where the $a_{t(Convection)}$ and the volume element are given by:

$$a_{t(Convection)} = \frac{\alpha h A_t}{K \Delta V} \qquad \Delta V = r_m \Delta \emptyset \Delta r \frac{\Delta z}{2}$$

Node 18:

For the conditions $m > i > 1$, $j = n$, $k = 1$

The temperature of the node after one time interval (Δt) is:

$$T_{(i,j,k)}^{p+1} = T_{(i,j,k)}^{p} + \Delta t\big(a_s T_{out} + a_n T_{(i,j,k+1)}^{P} + a_e T_{(i+1,j,k)}^{P} + a_w T_{(i-1,j,k)}^{P} + a_t T_{out} + a_b T_{(i,j-1,k)}^{P} - a T_{(i,j,k)}^{P}\big) \quad (2.43)$$

where the $a_{t(Convection)}$ and the volume element are given by:

$$a_{t(Convection)} = \frac{\alpha h A_t}{K \Delta V} \qquad \Delta V = r_m \Delta \emptyset \Delta r \frac{\Delta z}{2}$$

The centre:

At the centre For the conditions $1 \leq i \leq m$, $j = 1$, $1 \leq k \leq f$

where;

$T = T_{(i,j,k)}^{p+1} = \frac{\sum t(i,2,k)}{m}$

2.6.4 Program description

The program is divided into two sections: input & initialization and solution of the temperature profile at each time increment (Figure 2-8).

Input and Initialization: Sets the number of nodes, material properties, initial constant temperature distribution within the body at zero time, the ambient quenchant temperature, the simulations stop temperature at the part centre, and the part dimensions.

Temperature Profile:

- The main loop is initiated and continues until the nodes at the part centre reach the stop temperature (part centre temperature = quenchant temperature).

- Locate the node positions and their equation (internal or surface nodes).

- Update the temperature profile and temperature step based on the current temperature profile and function of material properties and calculated thermal conductivity at each step for internal nodes, and function of material properties and calculated thermal conductivity and heat transfer coefficient for the surface node.

- Update the time-temperature history matrix.

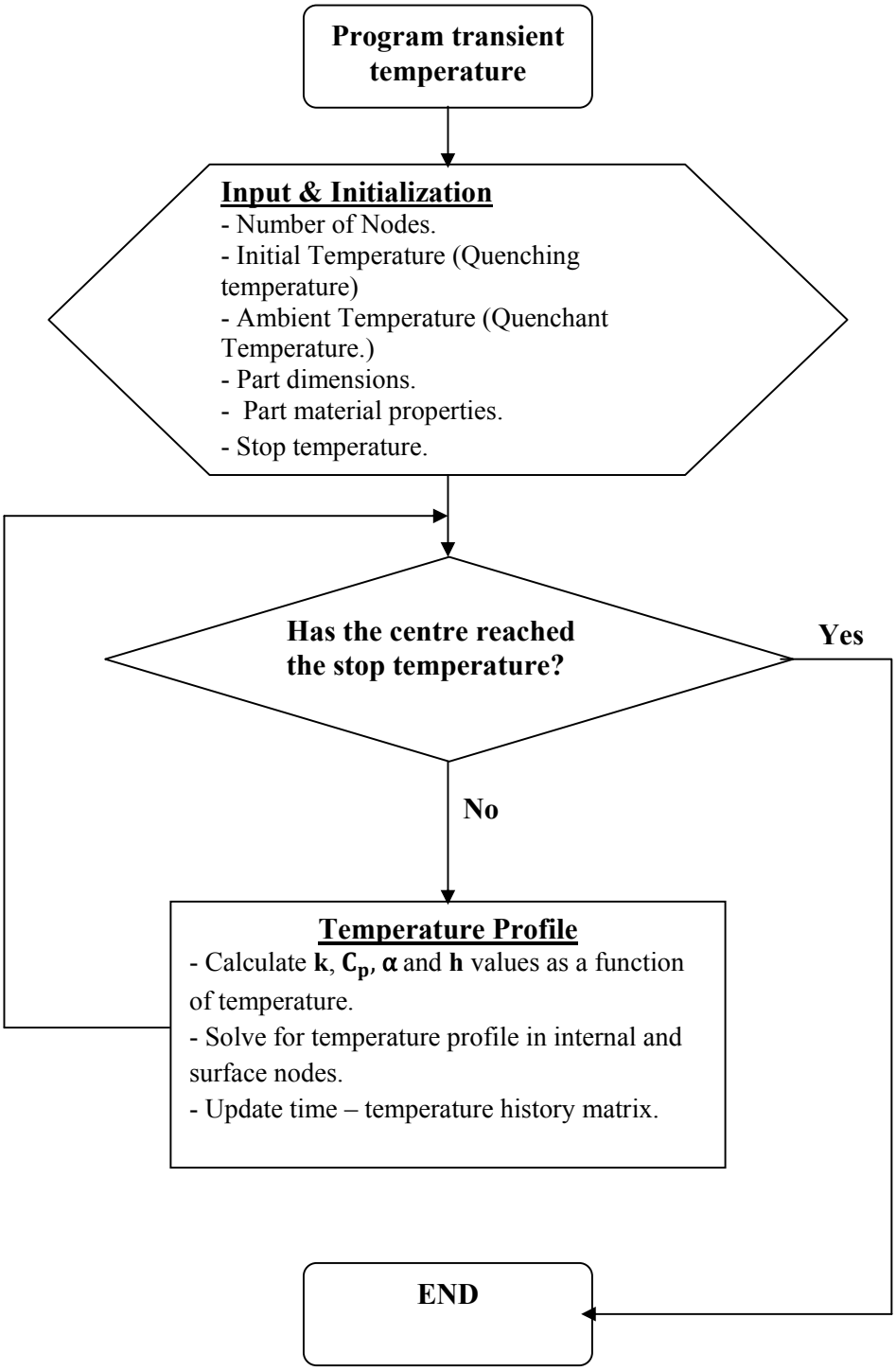

Figure 2-8: Temperature profile program flowchart.

Chapter 3

Neural Network Model for Prediction of Thermal Conductivity of Steels

3.1 Introduction

Quenching processes are sensitive to the thermal conductivity. Accurate modelling and probe design rely on knowledge of this parameter as discussed in chapter 2. The dependence of thermal conductivity on temperature must be known for the steel studied (equation 2.13); it controls after all the magnitude of the thermal gradients which occur in components during quenching. Gradients lead to thermal stresses, and may also lead to variation in microstructure, both of which limit the size of components that can be with the desired homogeneous microstructure.

In the absence of any quantitative model the only choice is to look for similar compositions contained in published tables of data [70, 80, 81], but appropriate information may not always be available.

Due to the complexity, no physical model exists that can estimate the thermal conductivity of an arbitrary steel; this limits the ability to model the quenching behaviour. Nevertheless a lot of conductivity data have been published; it was decided to develop a quantitative neural network to express the information in multivariate form.

A neural network can be regarded as a general form of regression, providing an approach by which a quantitative prediction may be made in situations when the complexity of the problem makes a *physically rigourous* treatment difficult. However, the technique can become *mathematically rigourous* when developed in a Bayesian framework, since the relevance of each datum and each variable can then be inferred automatically.

3.2 Modelling Complex Properties

There are material properties that can be modelled simply and analytically, such as crystallization kinetics or the tensile properties of composite materials. However, in some cases the property arises from many interacting effects, not all of which are well understood. Even if the mechanisms are known it may not be clear how they work together, and simplification of the problem may be unacceptable from an engineering point of view. The yield stress of a metal for example, cannot be calculated from first principles, although the dependence on variables such as grain size, dislocation density, etc, is understood.

In cases like these, properties can be estimated based on models that have been fitted to the available empirical data. A neural network can make the best use of existing complex, multi-dimensional data even when the data are sparse, not uniformly distributed in the variable space, or both. The purpose of the data-fitting is to assess the contribution of each input parameter to the output, and to make quantitative, rather than merely qualitative, predictions. This approach has been demonstrated as a powerful tool to aid the creation of new materials [82-83].

3.3 Thermal conductivity

The large heat conductivity of metals is one of their most ordinary properties, because both electrons and phonons (the lattice vibration) contribute to the thermal conductivity. The heat conductivity can be described as [84]:

$$K = \frac{1}{3}\left[(C_V v\, l)_p + (C_V v\, l)_e\right] \tag{3.1}$$

where C_V is the specific heat capacity , v velocity, and l is the mean free path. The first term in this equation is the lattice contribution, the velocity in this term is almost constant (the speed of sound), and the second term comes from electrons, the velocity is the mean speed of the responsible electrons. In metals the electron contribution is dominant, whereas for semiconductors and insulators, the phonon contribution is dominant.

In good electrical conductors a rather large number of free electrons move about the lattice of the material. Just as these electrons may transport electric charge, they may also carry thermal energy from a high temperature region to a low temperature region. Energy may also be transmitted as vibrational energy in the lattice structure of the material. In general, however, this latter mode of energy transfer is not as large as the electron transport, and for this reason good electrical conductors are almost always good heat conductors, like copper, aluminium and silver, and electrical insulators are usually good heat insulators[1] [84].

[1] Diamond is an exception, being an electrical insulator, but capable of thermal conductivity five times as high as silver or copper (about 2000 W m^{-1} K^{-1} at room temperature), because of the strong carbon-carbon interaction and the exceptionally high velocity of sound (1800 m s^{-1}).

3.3.1 Thermal conductivity and electrical resistivity

Since the free electrons are responsible for the electrical and thermal conductivities of conductors, many researchers use the Wiedemann-Franz-Lorenz law to attempt to relate the thermal conductivity to the electrical resistivity (equation 3.3). This can be an extremely useful approximation, since it is much easier to measure resistivity than thermal conductivity; however, they do not generally have the same temperature dependence [70 ,85]:

$$\frac{K}{\sigma T} = \frac{\pi^2 k_B^2}{3e^2} \equiv L_\circ \tag{3.2}$$

where σ is the electrical resistivity, k_B the Boltzmann constant, e is the electron charge, $L_\circ$ called the Lorenz number which is the same for all metals ($L_\circ = 2.45 \times 10^{-8}\ \mathrm{W\,\Omega\,K^{-2}}$) then:

$$\frac{K}{\sigma} = L_\circ \mathrm{T} \tag{3.3}$$

3.3.2 Effect of temperature

As the temperature is increased, electron-phonon scattering becomes dominant decreasing the thermal conductivity in metals. The mean free path for such scattering reduces with increasing temperature ($l \propto T^{-n}$ with n larger than unity); the mean free path of electron at room temperature is typically on the order of 10 nm depending on the material. As a result of electron-phonon scattering, thermal conductivity of metals decreases at high temperatures. There is also the possibility for a more complex behaviour due to heterogeneous microstructures and phase transformations [84].

3.3.3 Effect of alloying

The thermal and the electrical resistance of alloys with the foreign atoms in solid solution is nearly always greater, and in some cases considerably greater, than that of a pure metal [85]. One atomic percent of tin added to copper will increase the specific electrical resistance from 1.55 to 4.15 μΩ cm. In dilute concentrations the effect of alloying is independent of temperature. The high resistance of alloys can be explained by electron interactions with the matrix. The resistance of a pure metal is largely due to the disturbance to the periodicity of the lattice by thermal agitation. When foreign atoms are added they cause perturbations in the lattice, and electrons will be deflected even in the absence of thermal agitation [85, 86].

Nechtelberger [87] empirically related the change in thermal conductivity of ferrite by alloying to the thermal conductivity of pure iron by an equation of the form:

$$\lambda = \lambda_o - \ln \sum x \tag{3.4}$$

where x was the alloying element in %. Perhaps such a relation can be justified if we consider the disturbance in periodicity by alloying.

Since there is a large effect on thermal conductivity by any disturbance in the periodicity, the heat treatment of steels can be expected to have a large effect on conductivity; after all, a large variety of microstructures can be achieved at constant composition. For example, quickly cooling a steel from the austenite range is likely to produce a martensitic microstructure, with carbon and other alloying elements present in a super-saturated solid solution. Heating will then trigger tempering behavior, as carbides precipitate and grow. In contrast, slow cooling would produce a coarser mixture of cementite and

ferrite with lower amounts of solute elements in ferrite, and with a lower defect density. The thermal conductivity of the martensite at room temperature would be lower, but would tend towards that of the ferrite-cementite mixture upon heat treatment below the austenite phase field.

As temperatures increase into range 700-900 °C the thermal conductivity of different steels converge, this can be explained by the increased important of phonon scattering, also the phase change to austenite occurs and elements go into solution.

Richter [88] and Powell [89] have shown the thermal conductivities as a function of temperature for a number of different steels. The thermal conductivities of the alloys diverge as temperature is decreased, pure iron having the highest thermal conductivity, followed by steels, alloy steels and then the high-alloy steels. High-alloy steels have relatively low thermal conductivity at ambient temperature than at high temperatures. At higher temperatures when austenite forms in all the alloys, the thermal conductivities become similar (figure 3-1).

The thermal conductivity of an alloy will depend upon temperature and microstructure (therefore time in some cases). In principle, an accurate model should be possible when the microstructure can be predicted (a problem which is still the topic of a great deal of research). Giving contributions to different phases with different contributions, a law of mixtures rule should be successful; indeed such an approach has been used for cast irons [17].

3.4 Bayesian Neural Networks

Bhadeshia has provided two comprehensive reviews on the use and performance of neural networks in materials science [82, 90]; with the objective of encouraging the proper application of this method. The approach used in this chapter follows the work of MacKay [91], who applied neural networks models in a Bayesian framework making it possible to 'quantitatively embody Occam's razor'[2].

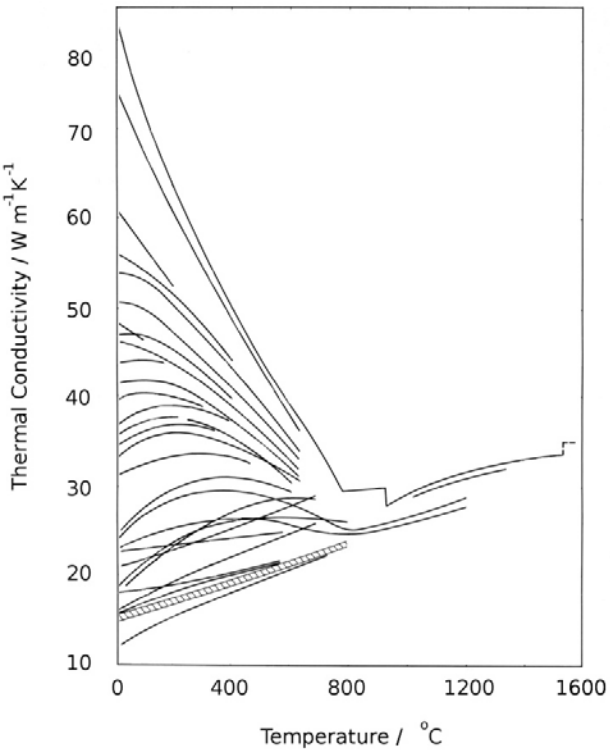

Figure 3-1: Variation of thermal conductivities of iron and steels with temperature [88].

a-Iron. b- Carbon steel.

c- Alloy steels. d- High alloy steels.

[2] Occam's razor is the principle that states a preference for simple theories. `Accept the simplest explanation that fits the data'.

Along with the Bayesian approach MacKay also recommends incorporating the further methods which can also contribute to the success of modelling. The robustness is further improved by splitting the data into testing and training sets, which allows the selection of models which avoid overfitting. Multiple sub-models are trained to form an optimum committee of models [92-94]. These methods further attempt to find the appropriate level of complexity from the data provided, and provide a robust solution which generalizes well. The approach used has been applied previously in materials science, [95-100], a good explanation of the use of the committee of models has been provided by Sourmail *et al.* [101].

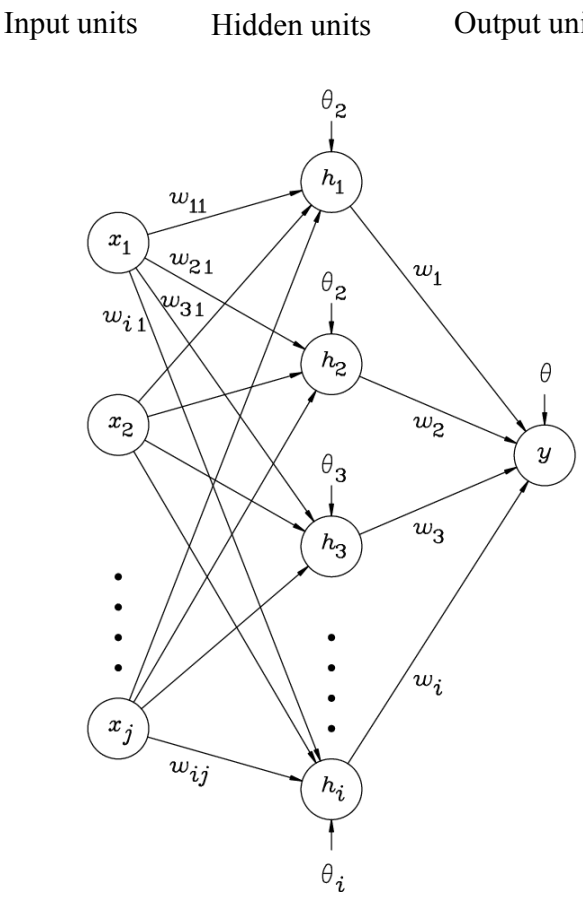

Figure 3-2: An example of three layer neural network with four inputs and five hidden units.

There is an implicit assumption in neural network modelling that the input variables are related to the output by a continuous and differentiable function. In training the network the aim is to mimic the behavior of this function. MacKay [92] has shown that a sufficiently complex three-layer network, as shown in figure 3-2, using hyperbolic tangent functions in the form of equation 3.5, is able to imitate any such non-periodic function.

The neural network in this case is simply a flexible equation that can be fit to any data set, by adjusting the parameters or "weights". It is usual for the equation 3.5 to be the sum of many hyperbolic tangent functions equation 3.6. The output variable is expressed as a linear summation of activation functions, h_i, weighted by the weights w_i and the bias θ.

$$y = \sum_i w_i \, h_i + \theta \tag{3.5}$$

In the case of a hyperbolic tangent formulation, the activation function for a neuron i in the hidden layer is given by:

$$h_i = \tanh\left(\sum_j w_{ij} x_j + \theta_i\right) \tag{3.6}$$

with weights w_{ij} and biases θ_i. In order to allow simple comparison between inputs whose magnitude are arbitrary, each variable is normalised within the range ±0.5 using the function:

$$x_{j=} \frac{x - x_{min}}{x_{max} - x_{min}} - 0.5 \tag{3.7}$$

where x is the un-normalised input, x_{min} and x_{max} are the minimum and maximum values in the database for that input, and x_j is the normalised value.

'Training the network' is achieved by altering the parameters to fit the functions to the data using 'back propagation' gradient descent optimization

procedures [102], to minimise an objective function which balances complexity and accuracy, typically:

$$M(w) = \beta E_D + \alpha E_W \tag{3.8}$$

E_W is a regularization function to penalize more complex functions, which have larger number of hidden units and is given by:

$$E_W = \frac{1}{2}\sum_{ij} w_{ij}^2 \tag{3.9}$$

E_D is the overall error between target output values and network output values, given by:

$$E_D = \frac{1}{2}\sum\left(t^{(i)} - y^{(i)}\right)^2 \tag{3.10}$$

where $t^{(i)}$ and $y^{(i)}$ are the target and corresponding output values for the example input from the training data $x^{(i)}$. α and β are control parameters which influence the balance between a simple but inaccurate model, and an overcomplex, also inaccurate model. MacKay's algorithm allows the inference of these parameters from the data, permitting automatic control of the model complexity this is necessary to generate a model of appropriate complexity, which can find the general trends from the data.

The final values of the weights depend upon the initial guess made for the probability distribution of the weights and the number of hidden units. Therefore a large number of separate models are trained with different starting conditions.

Sub-models are best evaluated using the log predictive error (LPE), in comparison to calculating the test error (sum squared error) this function penalises inaccurate predictions less when they are accompanied by large error

bars. Assuming that for each example m the model gives a prediction according to the normal distribution with average $y^{\mathrm{m}}$and variance $\sigma^{(m)^2}$:

$$LPE = \sum_m \left[\frac{1}{2}\frac{(t^m - y^m)^2}{\sigma^{(m)^2}} + \log\left(\sqrt{2}\sqrt{\pi\sigma^{(m)}}\right)\right] \quad (3.11)$$

This is combined with cross-validation to further guard against over-fitting. The data is split into training and testing set, this allows alternate sub-models to be compared by their performance in predicting the unseen data using equation (3.11). A collection of the best models as decided by the lowest LPE is combined to make a committee model. The prediction is the average of those of the sub-models. The errors for the different committees can be calculated and the one with the lowest perceived predictive error is used.

3.4.1 Overfitting the model of neural network

Overfitting the data is a difficulty caused by the use of powerful nonlinear regression methods. In addition to the methods described above to help avoid this, the experimental data can be divided into two sets, a training dataset and a test dataset. The model is initially produced using only the training data. The test data are then used to assess the model behavior when presented with previously unseen data. This is illustrated in Figure 3-3, which shows three attempts at modelling noisy data for a case where *y* should vary with x^3. A linear model (Figure 3-3 (a)) is too simple and does not capture the real complexity in the data. An over complex function such as that illustrated in Figure 3-3 (c) accurately models the training data but generalises badly. The optimum model is illustrated in Figure 3-3 (b). The training and test errors are shown schematically in Figure 3-3 (d); not surprisingly, the training error (the mismatch between model predictions and the training dataset) tends to

decrease continuously as the model complexity increases. It is the minimum in the test error (the mismatch between model predictions and the test dataset) which enables that model to be chosen which generalises best to unseen data [102-104].

3.4.2 Noise and uncertainties

There are two kinds of errors to consider, when conducting experiments, the noise in the data and the uncertainty of modelling. The noise results in a different output for the same set of inputs when the experiment is repeated. This is due to errors in measurement, and due to variables which were not controlled so their influence is not included in the analysis. The second kind deals with the uncertainty of modelling; there are many mathematical functions which can adequately represent the same set of empirical data.

As shown in Figure 3-4 the error bars, which are calculated using Bayesian inference, represent both experimental noise (region A) and the uncertainty in prediction due to lack of knowledge (region B) [102].

This methodology has proved to be extremely useful in materials science where properties need to be estimated as a function of a vast array of inputs. It is then unlikely that the inputs are uniformly distributed in the input space.

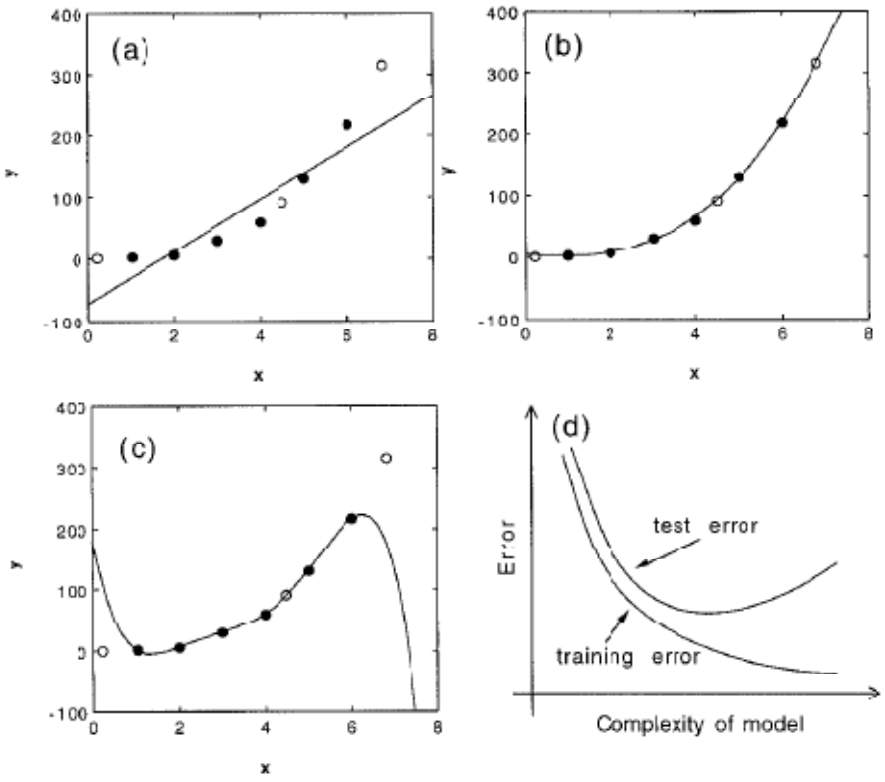

Figure 3-3: Variations in the test and training errors as a function of model complexity, for noisy data in a case where *y* should vary with x^3. The filled points were used to create the models (training data), and the circles constitute the test data [102].

(a) A linear function which is too simple.

(b) A cubic polynomial with optimum representation of both the training and test data.

(c) A fifth order polynomial which generalizes poorly.

(d) Schematic illustration of the variation in the test and training errors as a function of the model complexity.

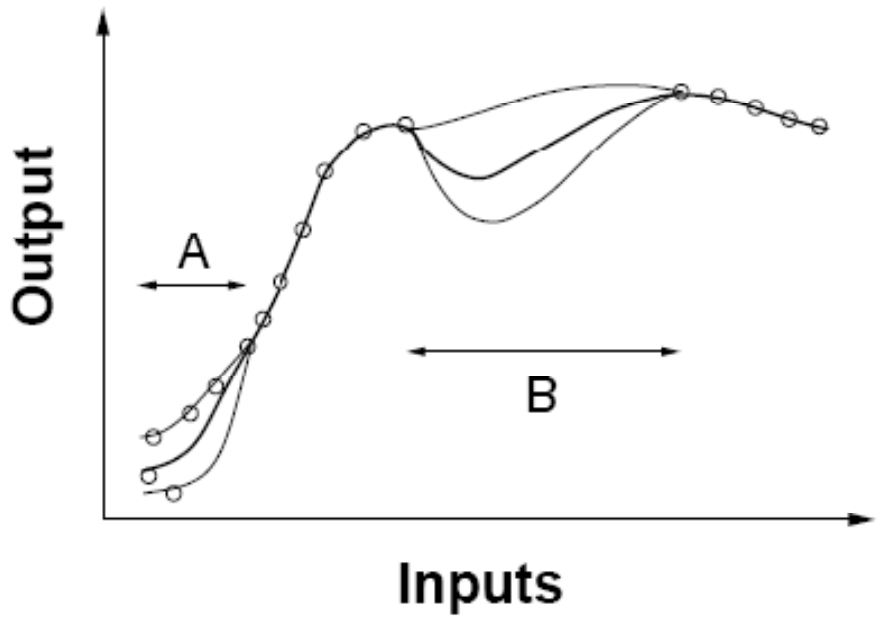

Figure 3-4: Schematic illustration of the uncertainty in defining a fitting function in regions where data are sparse (B) or where there is scatter (A).The thinner lines represent error bounds due to uncertainties in determining the weights [102].

3.5 Procedures

To investigate the composition dependence of the thermal conductivity, a database was collated and a neural network produced. Modelling was carried out using the Bayesian neural network after Mackay as implemented in the bigback program using the commercially available Neuromat model manager software interface [105].

The database of the thermal conductivity of steels was obtained from the published literature [80, 81]. Data are generally available in a form giving the chemical composition, temperature and sometimes the heat treatment condition of the steel. Details of the initial condition of the steel have been

omitted from this model so as to make it more generally applicable. This also avoids any complications which would be introduced from differences in the experimental procedure used to determine the thermal conductivity reported. Any differences due to microstructure should be incorporated into the spread of the predicted values.

The database contained 757 pairs of inputs (composition and temperature) and output (thermal conductivity) representing 223 steels. For many of the steels thermal conductivity had been reported over a range of temperatures, whereas others were only associated with a room temperature measurement only. Details of the inputs and the ranges for which data were available can be seen in table 3-1. The data are also available online [106].

In the case of N, B, Zr there were insufficient data to model this effect in a useful manner. It was therefore assumed that the small amounts of Zr, B and N do not influence the thermal conductivity; these inputs were removed but the steels concerned were kept in the database used for training. It's likely that all the alloys in the database include some level of nitrogen due to steel-making processes but the concentrations were not reported or measured. This is true of many elements, which will usually be present in trace amounts but are not generally reported. Any effect of these elements should therefore be reflected with greater uncertainty in the predictions. Figure 3-5 illustrates the range and the distribution of the variables plotted against the thermal conductivity.

The data were divided into two groups, the training and test data sets. In the ideal case the data would be a random sample from the input space, with each input changing independently. This is never going to be the case in practice. There is therefore an advantage in carefully selecting which of the data should be included in the training and the testing sets. This is necessary to

ensure that each set is a representative sample of the overall data, and to help avoid over–fitting by using as many as possible different compositions examples in each set and ensure that some compositions are used only in the testing set. Since it is desired to produce a model capable of predicting the thermal conductivity of unseen compositions, it is important to test this during the training procedure.

Table 3-1: Summary of the database of steel thermal conductivities, all elements are in wt%.

Input	Minimum	Maximum	Average	Standard Deviation
Fe wt%	8.687	100	89.22	16.25
C wt%	0.0	1.22	0.29	0.26
Mn wt%	0.0	13.0	0.74	1.25
Ni wt%	0.0	63.0	3.52	8.38
Mo wt%	0.0	4.80	0.33	0.82
V wt%	0.0	3.00	0.07	0.31
Cr wt%	0.0	30.40	3.82	6.86
Cu wt%	0.0	0.69	0.03	0.1
Al wt%	0.0	11.00	0.13	1.14
Nb wt%	0.0	3.00	0.06	0.33
Si wt%	0.0	3.50	0.27	0.47
W wt%	0.0	18.50	0.48	2.76
Ti wt%	0.0	1.40	0.015	0.11
Co wt%	0.0	55.9	0.93	6.05
Temperature /◦C	-200	1571	384.34	332
Conductivity / W m^{-1} K^{-1}	10.9	83.81	33.59	11.68

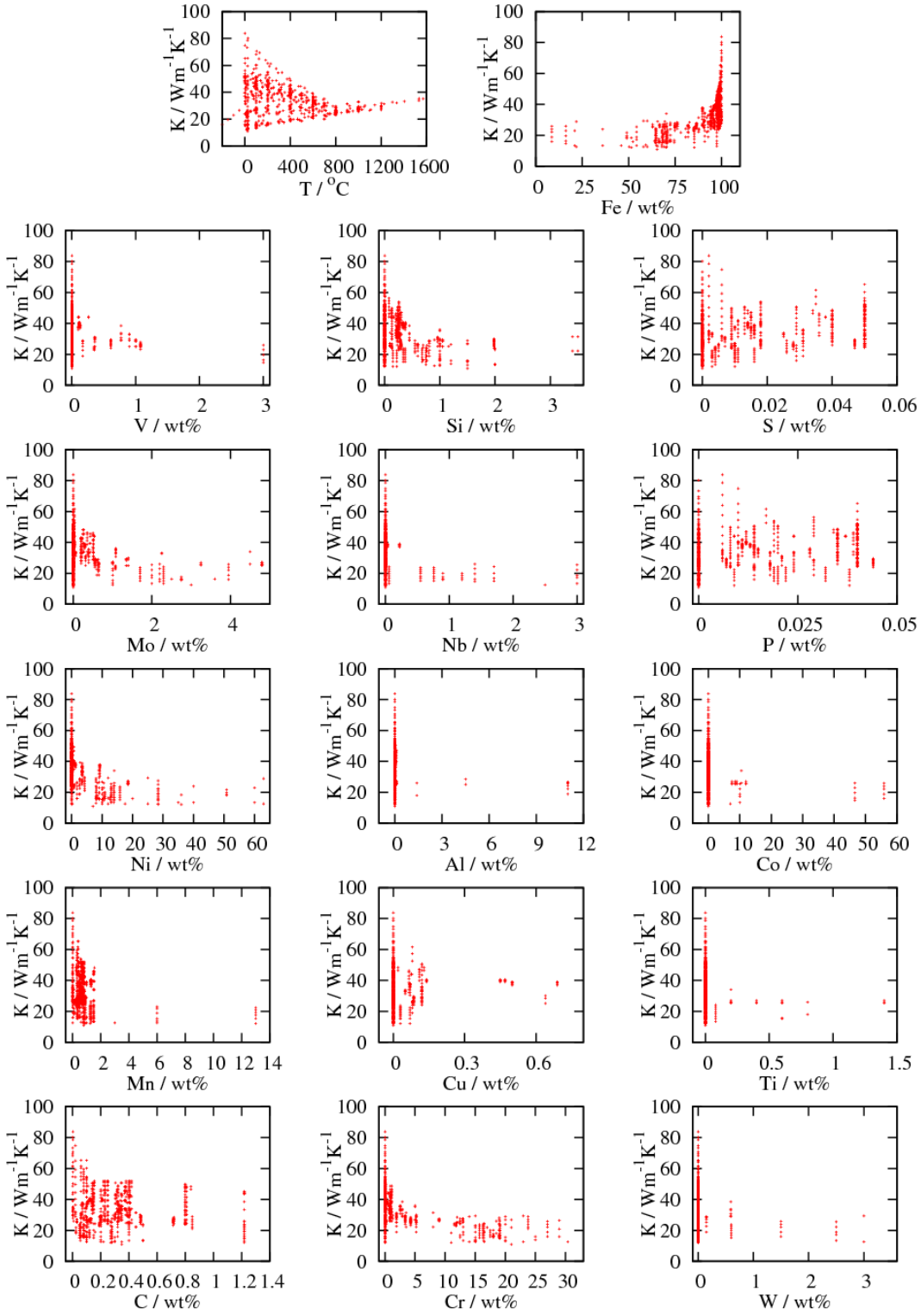

Figure 3-5: Distribution of data.

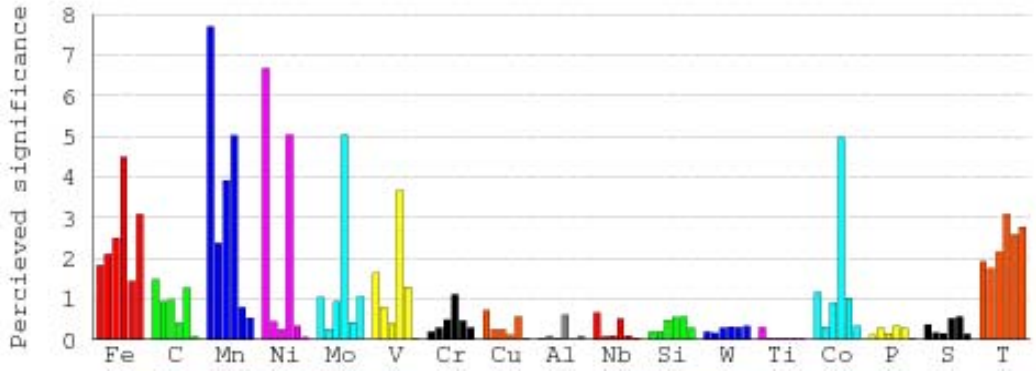

Figure 3-6: Significance of each input in each sub-model used to build the committee model, T is the temperature.

Training of sub–models with between 1 and 25 hidden units and using 9 different random seeds resulted in 153 sub–models successfully trained from 225 different initial conditions. Testing each of these models capabilities to predict the unseen testing set allowed a ranking by the log predictive error. A committee model of the best six models was selected since this resulted in the lowest combined test error.

Figure 3-6 shows the significance of each of the input variables as perceived by the neural network in influencing the thermal conductivity, the magnitude of the significance is a measure of the extent to which a particular input explains the variation in thermal conductivity. The model perceives low significance for Cu, Cr, Al, Nb, Si, W, Ti, P and S, this may mean the relationship is very simple, for example linear throughout the range of input, or that there is a low correlation between these inputs and the thermal conductivity. It also might be the case that these elements have been counted for through the 'Fe' input. Carbon has higher significant than these elements. Different sub-models assigned different significances to Mn, Ni, Mo, V and Co which sometimes had significance similar to carbon and sometimes had

large weights. Temperature and the sum of the elements (Fe) were robustly perceived to be significant inputs.

3.6 Model predictions

Figure 3-7 shows a comparison between the predicted thermal conductivity using neural network model and the target data from the test set. There is good agreement between them, which indicates optimum performance for the model.

Figure 3-8 shows the influence of increasing temperature on the thermal conductivity of iron and different steel compositions. Each composition has different thermal conductivity value at room temperature. As the temperature is increased, phonon scattering starts to dominate and the mean free path reduces with increasing temperature, and at high temperatures (austenite phase field) the thermal conductivity is much less dependent on the purity of the sample because all the elements go to the solution, the values converge.

Figures from 3-9 to 3-34 show that thermal conductivity decreases for each element as alloying increases, as expected from equation 3.4. The majority of the elements decrease the thermal conductivity when added both to pure iron and 0.1 carbon steel. The effect is more pronounced at lower temperatures. Vanadium and copper are both exceptions, it is likely the explanation is that these elements are not generally in solid solution. Vanadium will remove carbon from solution to form carbides, and copper will form copper precipitates, which have much higher conductivity than iron. Similarly titanium can be seen to have an effect in the 0.1 carbon steel (where TiC will form) but interestingly not in the pure iron. Effect of increased conductivity for vanadium addition to pure iron (figure 3-17) is probably an

artefact in the model, because the majority of data are for steels (containing carbon).

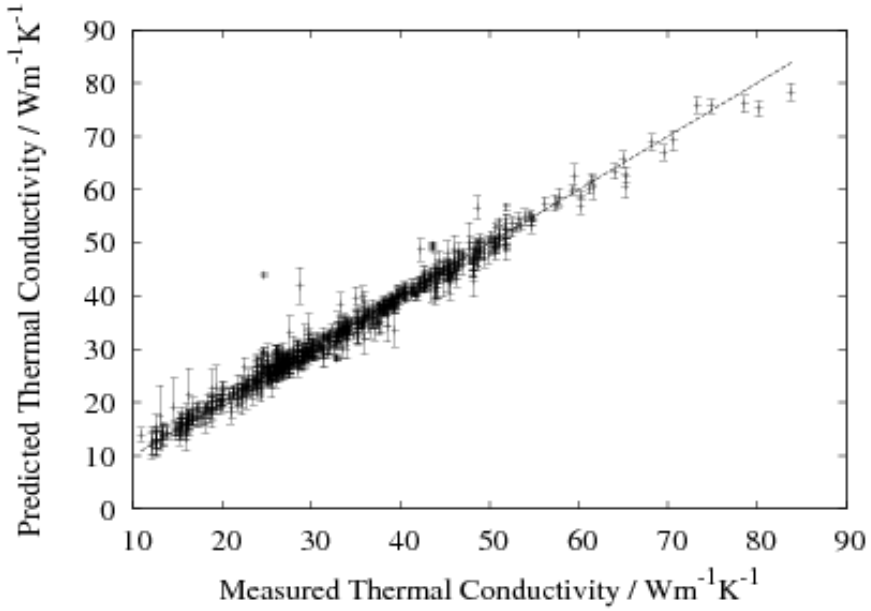

Figure 3-7: Comparison of predicted against the measured thermal conductivity for the final committee.

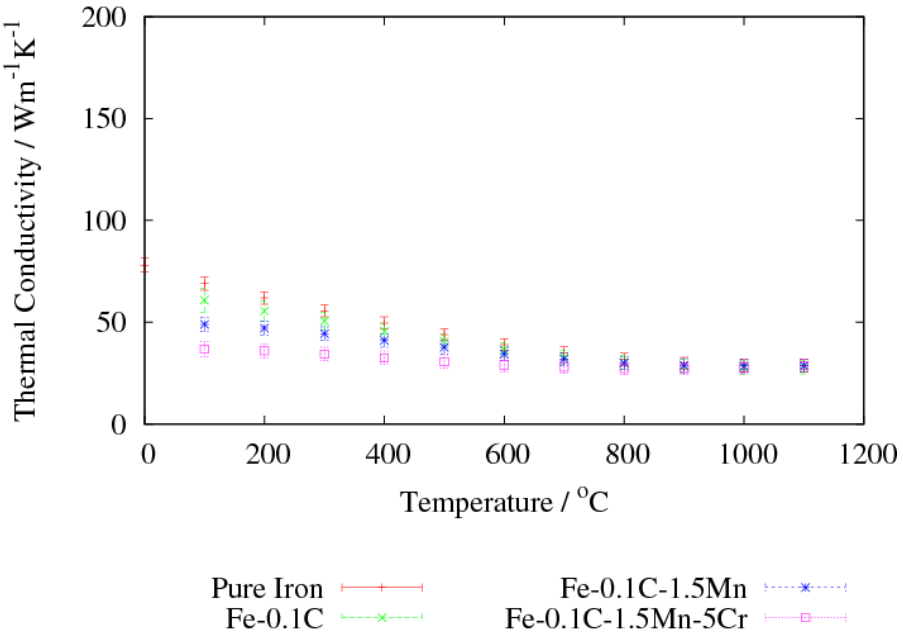

Figure 3-8: predicted influence of temperature on the thermal conductivity of iron and different compositions steels.

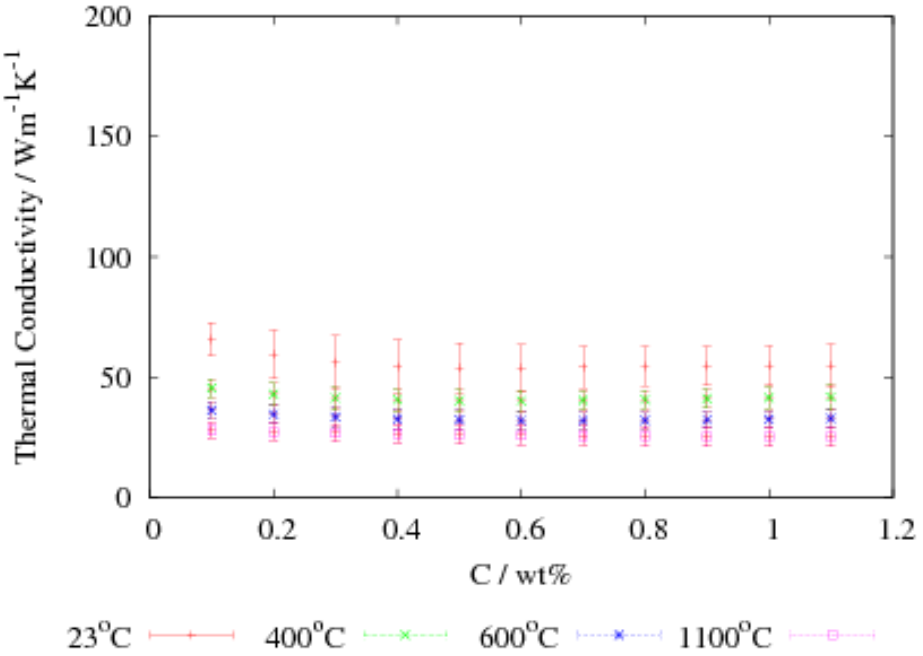

Figure 3-9: Predicted influence of carbon addition to pure iron at different test temperatures.

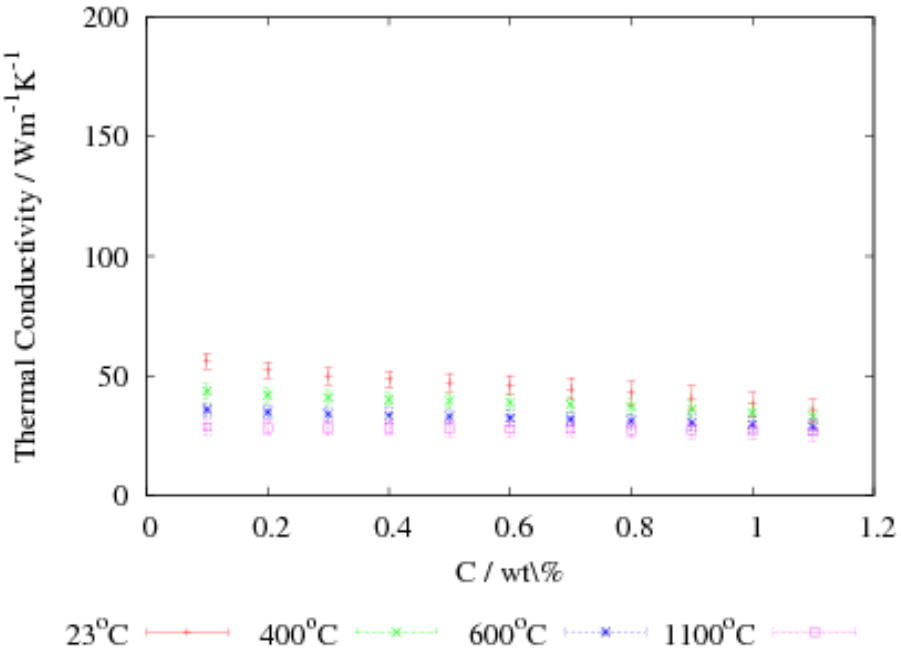

Figure 3-10: Predicted influence of carbon addition to 0.1C-1.5Mn steel at different test temperatures.

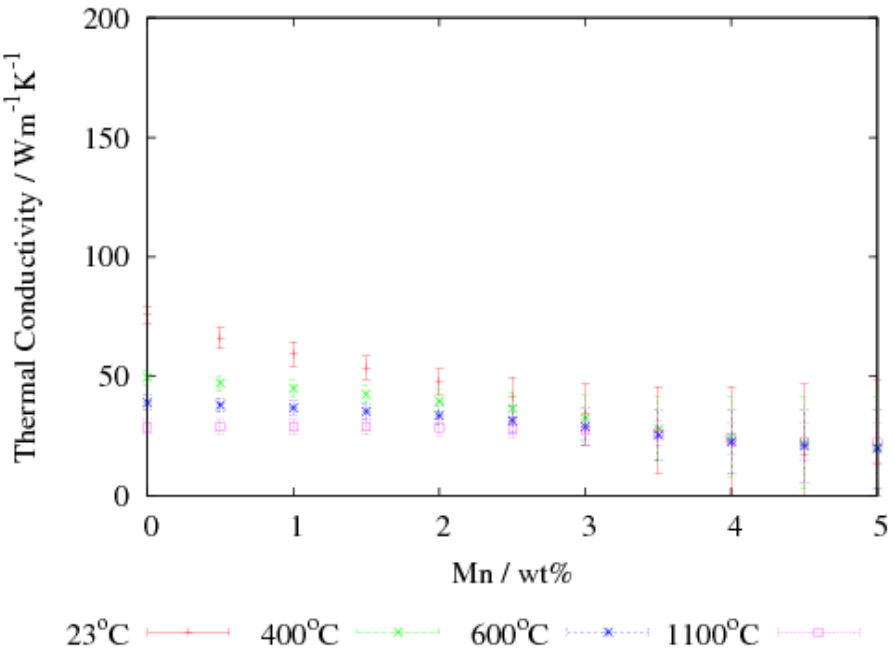

Figure 3-11: Predicted influence manganese addition to pure iron at different test temperatures.

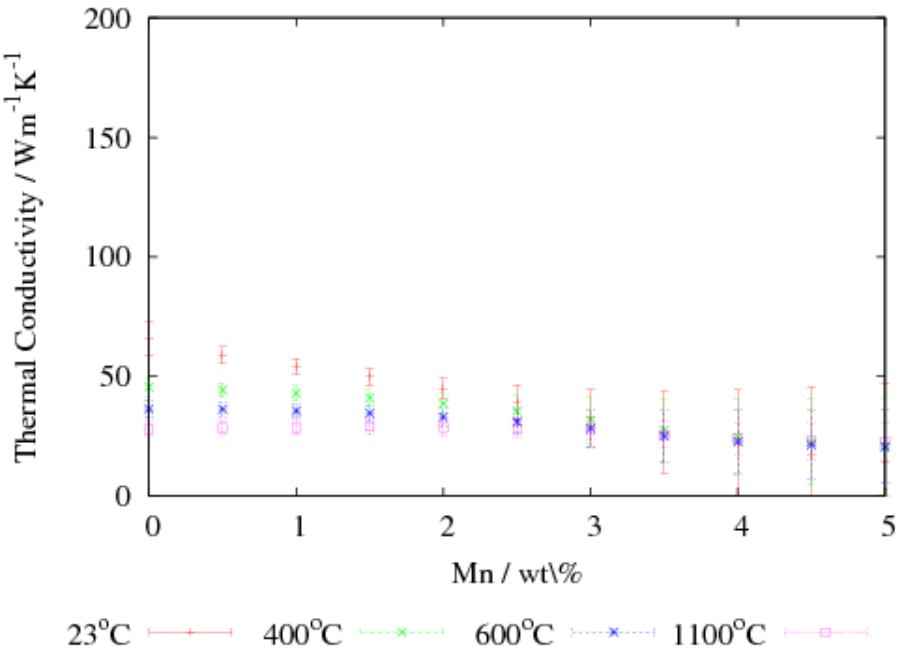

Figure 3-12: Predicted influence of manganese addition to 0.1C-1.5Mn steel at different test temperatures.

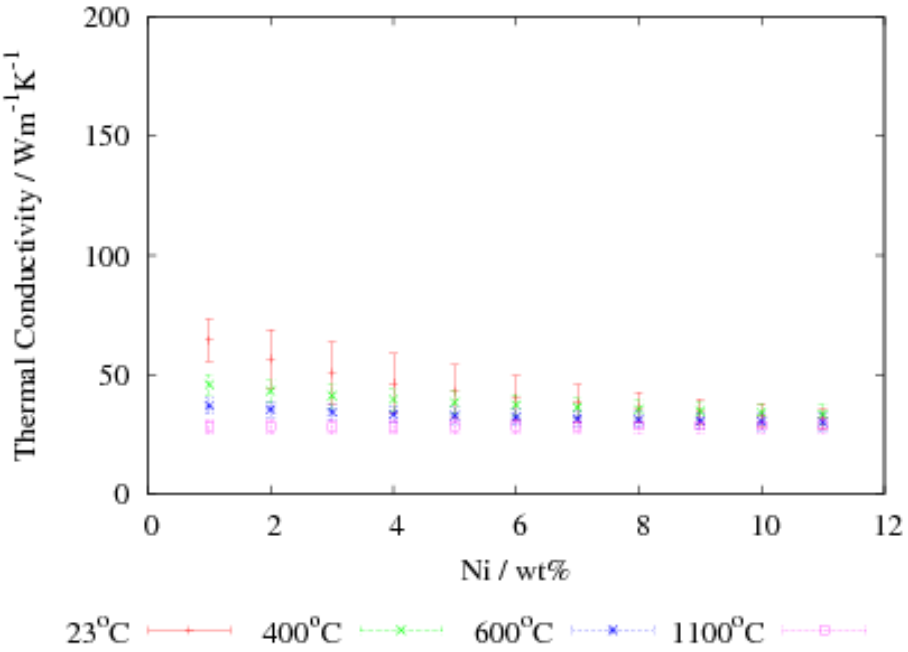

Figure 3-13: Predicted influence of nickel addition to pure iron at different test temperatures.

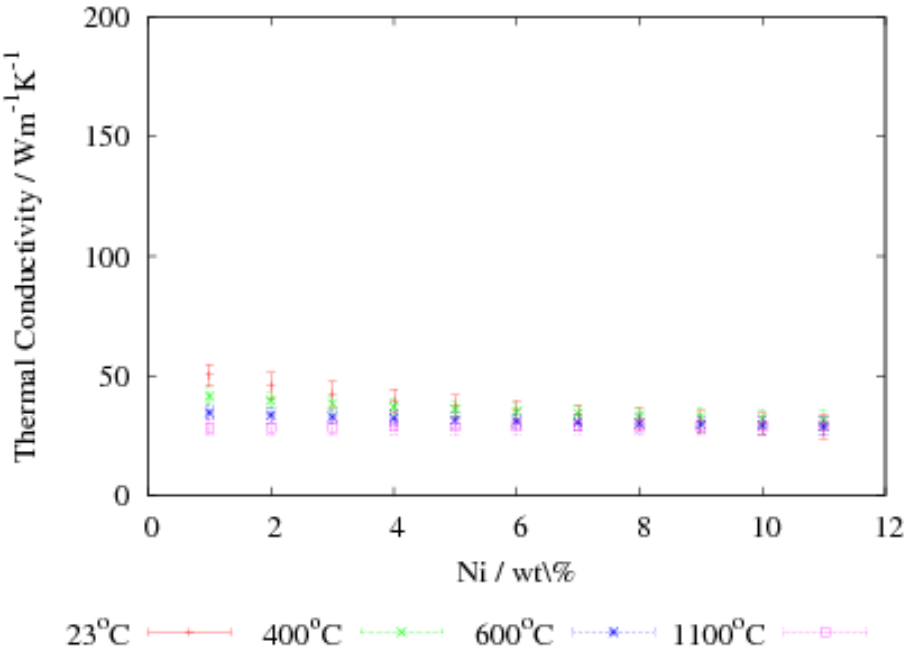

Figure 3-14: Predicted influence of nickel addition to 0.1C-1.5Mn steel at different test temperatures.

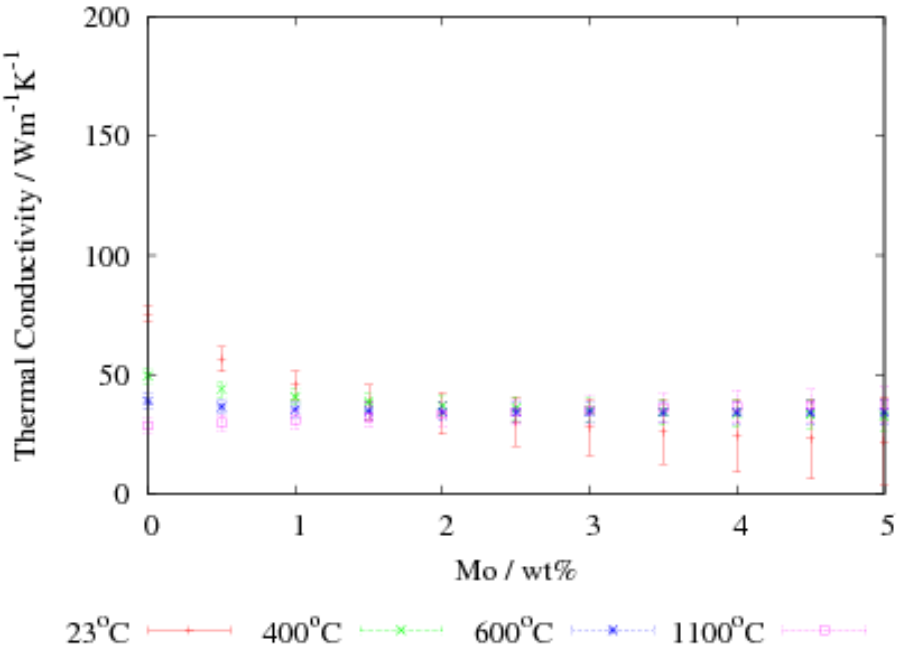

Figure 3-15: Predicted influence of molybdenum addition to pure iron at different test temperatures.

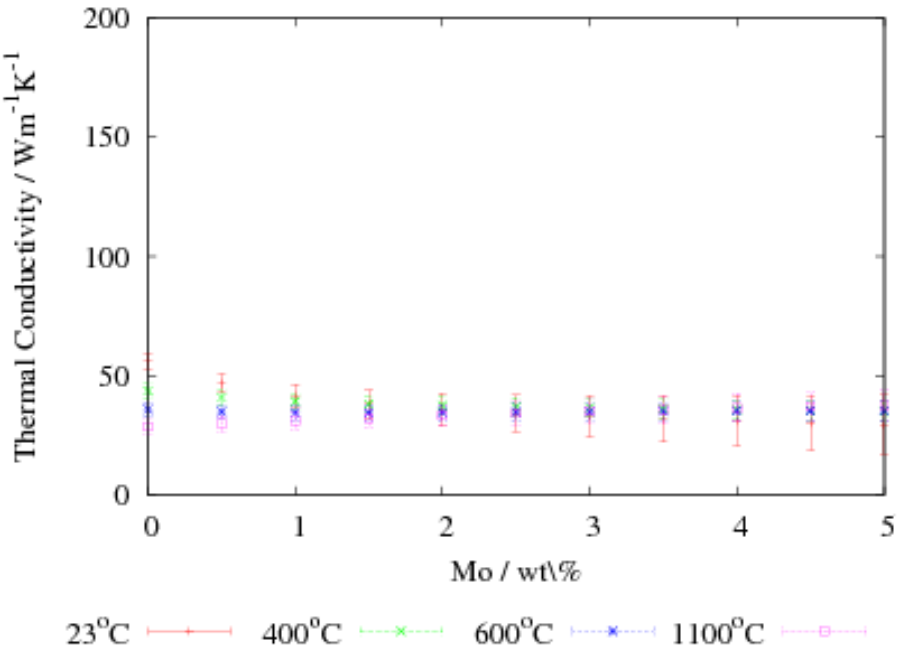

Figure 3-16: Predicted influence of molybdenum addition to 0.1C-1.5Mn steel at different test temperatures.

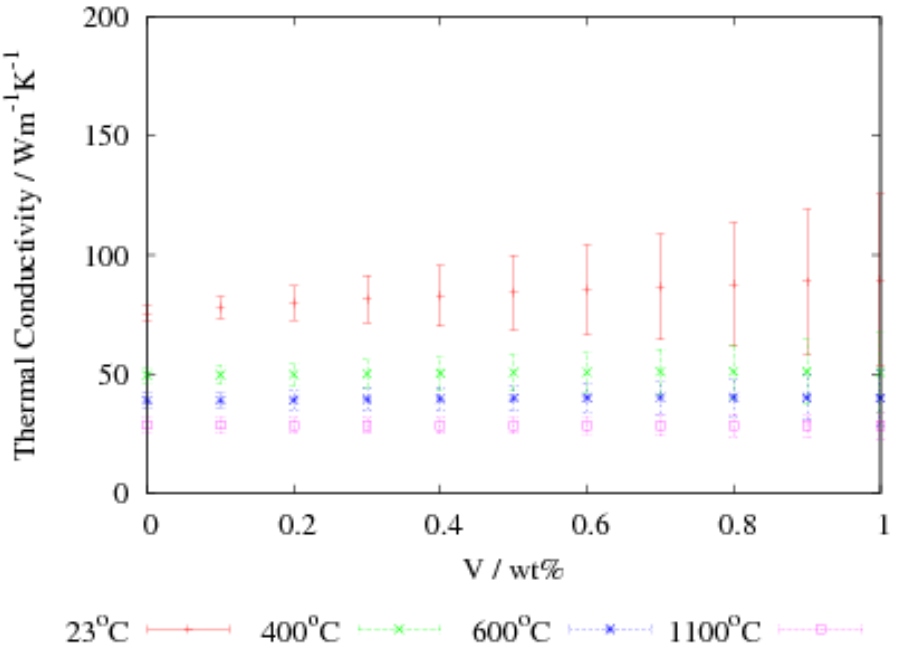

Figure 3-17: Predicted influence of vanadium addition to pure iron at different test temperatures.

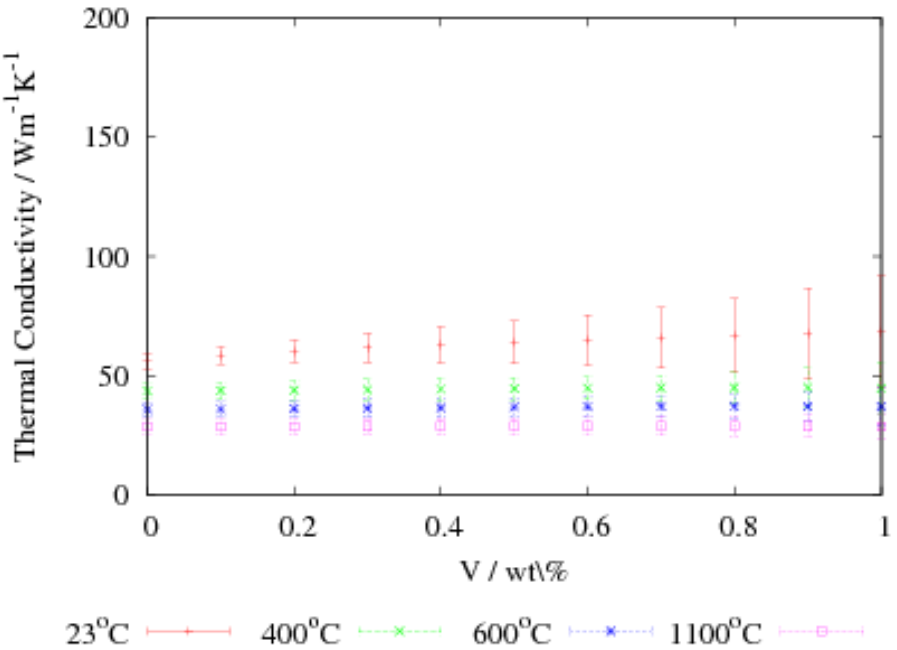

Figure 3-18: Predicted influence of vanadium addition to 0.1C-1.5Mn steel at different test temperatures.

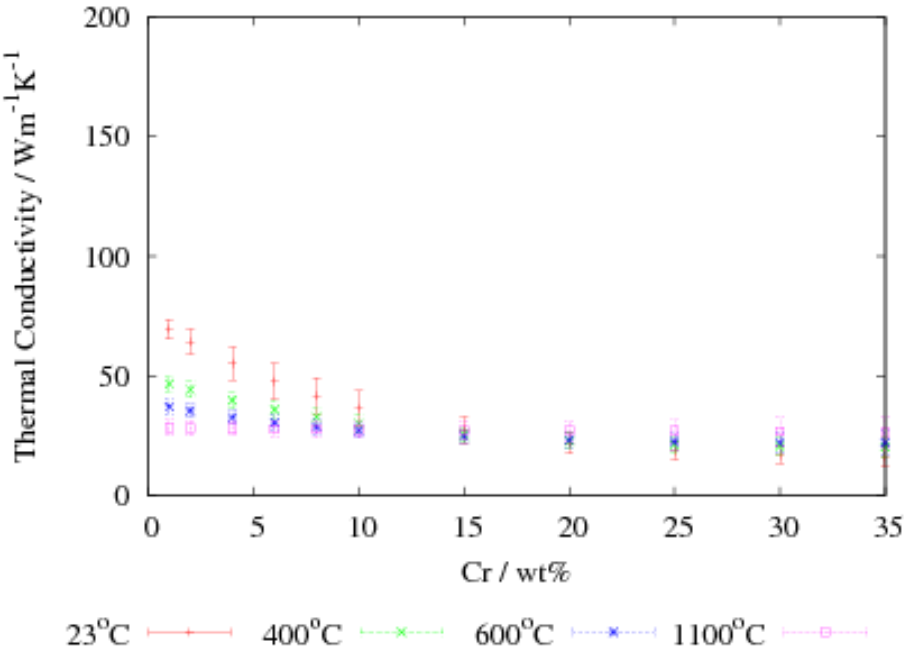

Figure 3-19: Predicted influence of chromium addition to pure iron at different test temperatures.

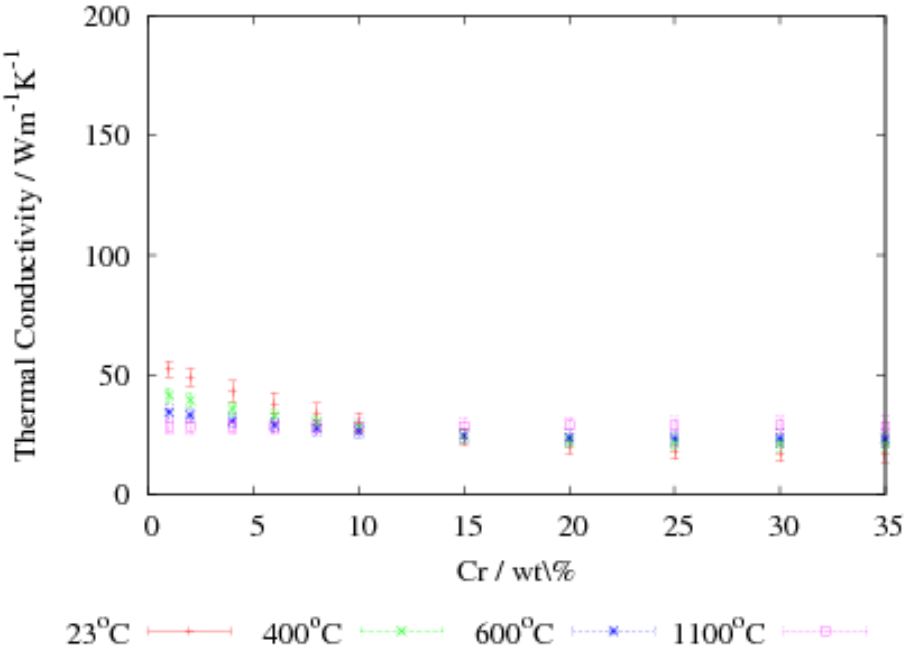

Figure 3-20: Predicted influence of chromium addition to 0.1C-1.5Mn steel at different test temperatures.

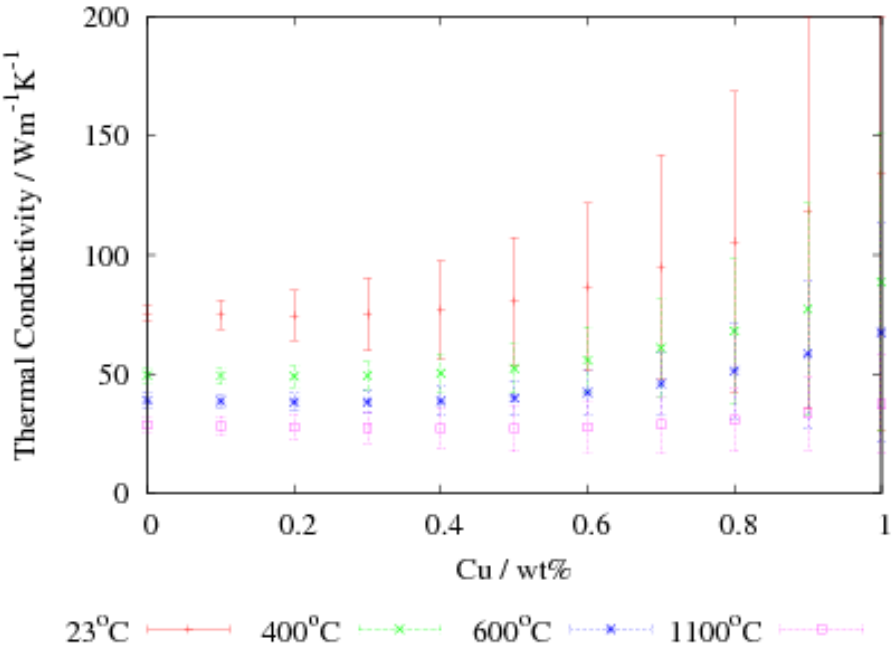

Figure 3-21: Predicted influence of copper addition to pure iron at different test temperatures.

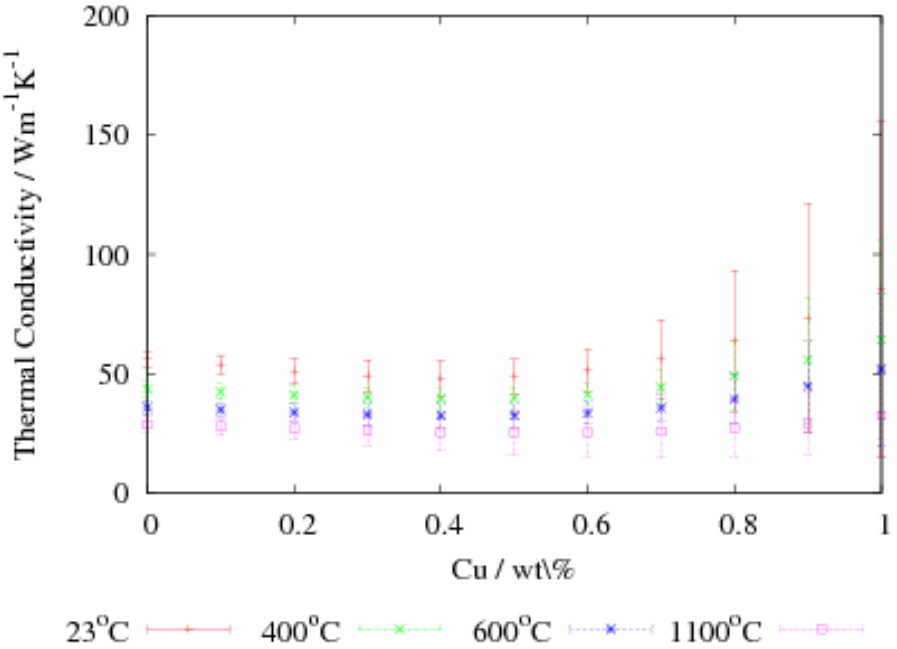

Figure 3-22: Predicted influence of copper addition to 0.1C-1.5Mn steel at different test temperatures.

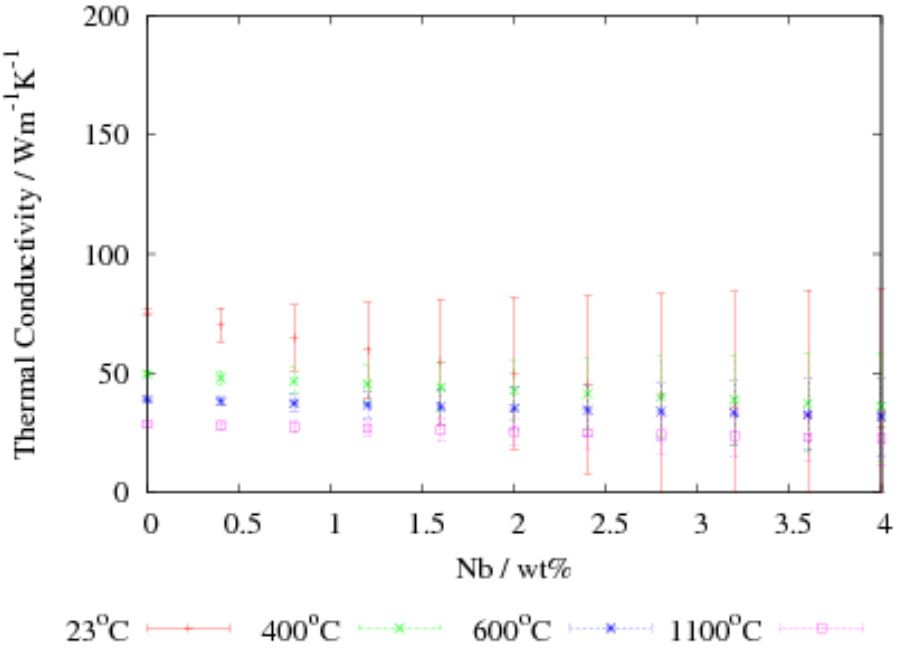

Figure 3-23: Predicted influence of niobium addition to pure iron at different test temperatures.

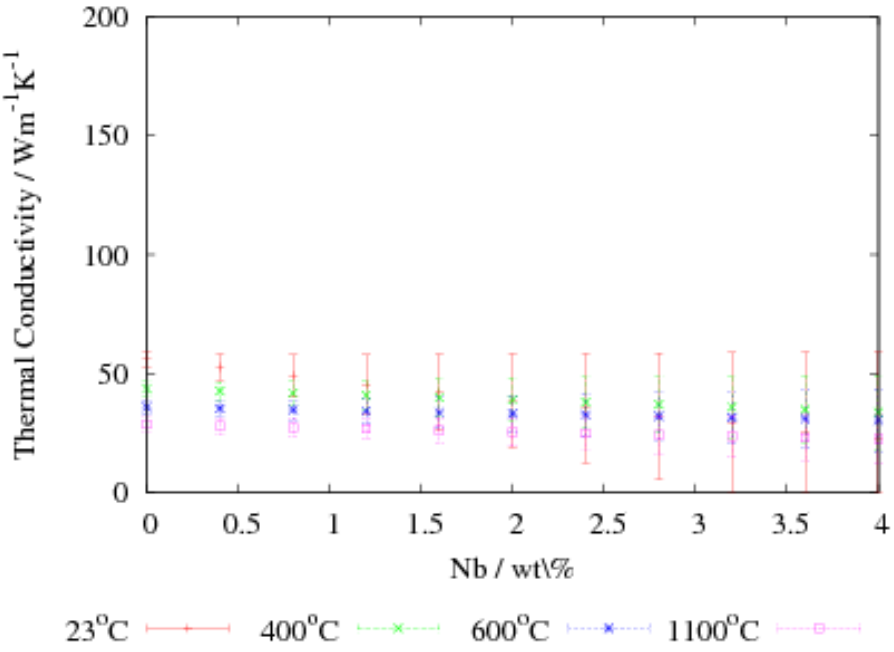

Figure 3-24: Predicted influence of niobium addition to 0.1C-1.5Mn steel at different test temperatures.

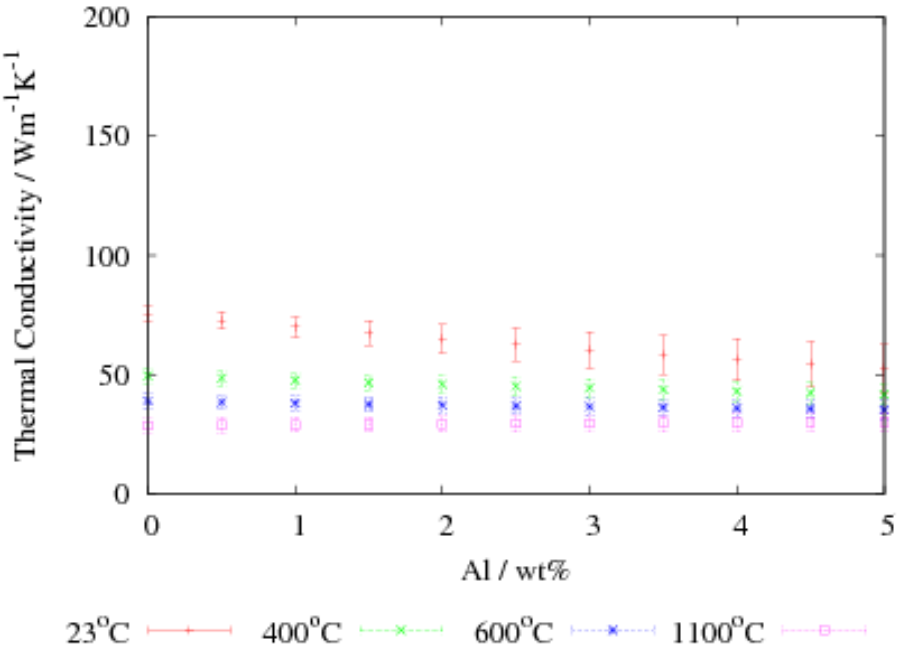

Figure 3-25: Predicted influence of aluminum addition to pure iron at different test temperatures.

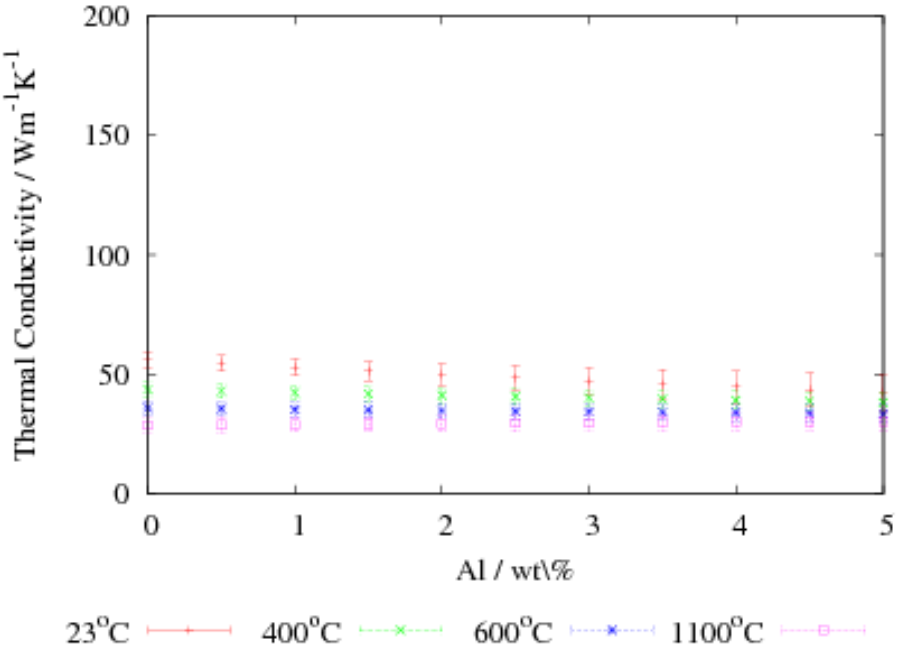

Figure 3-26: Predicted influence of aluminum addition to 0.1C-1.5Mn steel at different test temperatures.

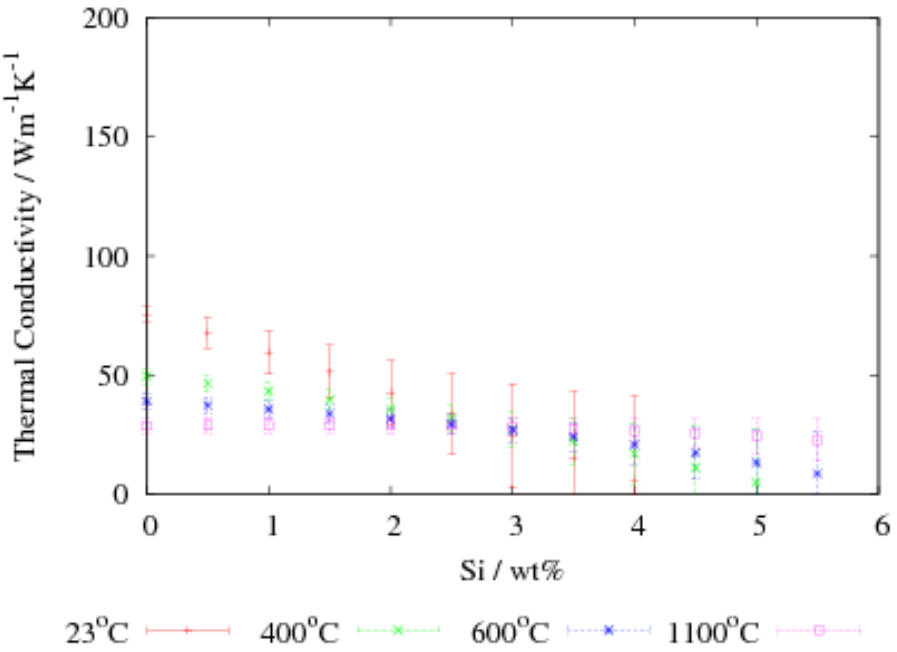

Figure 3-27: Predicted influence of silicon addition to pure iron at different test temperatures.

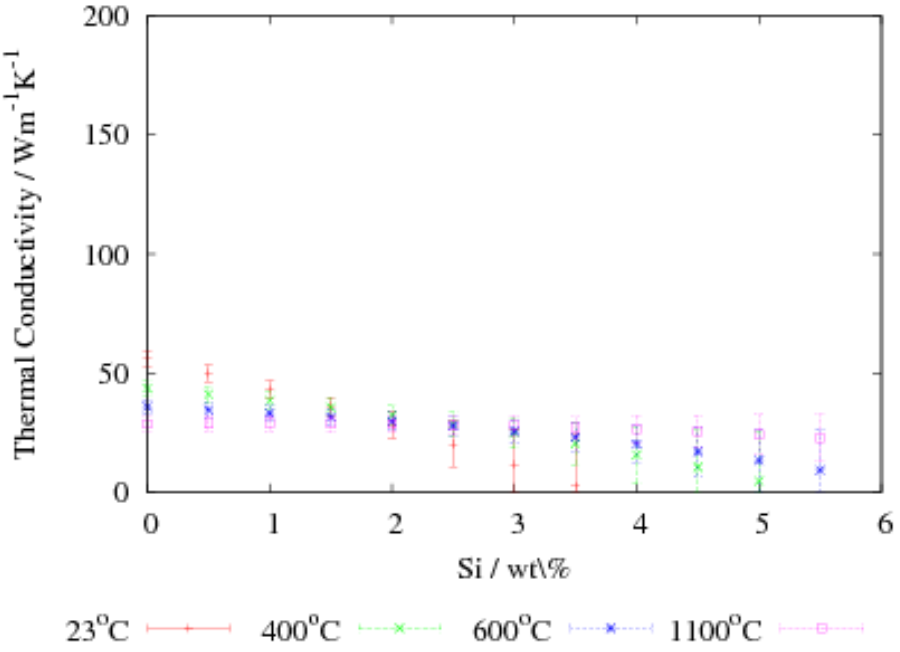

Figure 3-28: Predicted influence of silicon addition to 0.1C-1.5Mn steel at different test temperatures.

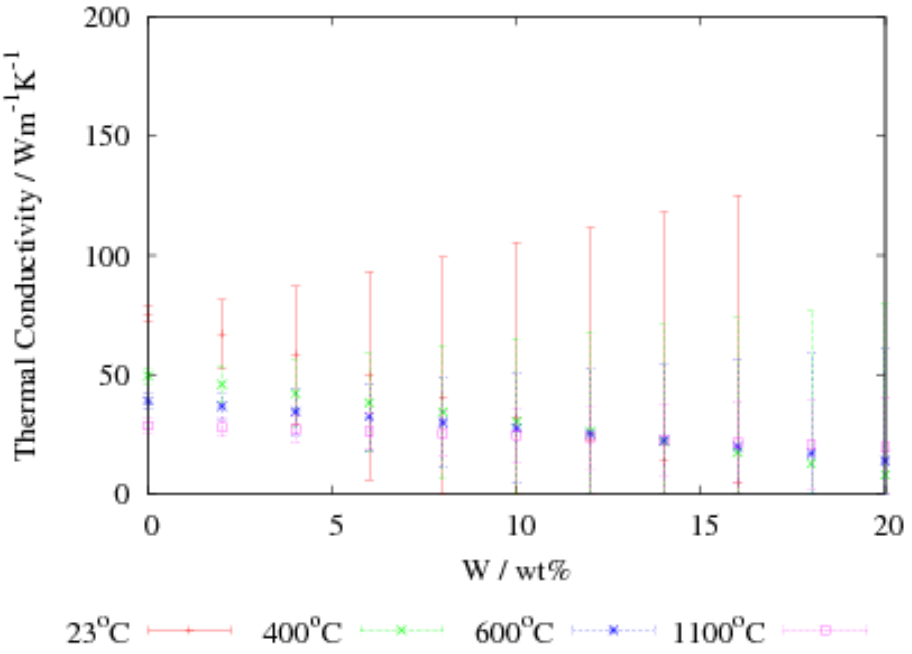

Figure 3-29: Predicted influence of tungsten addition to pure iron at different test temperatures.

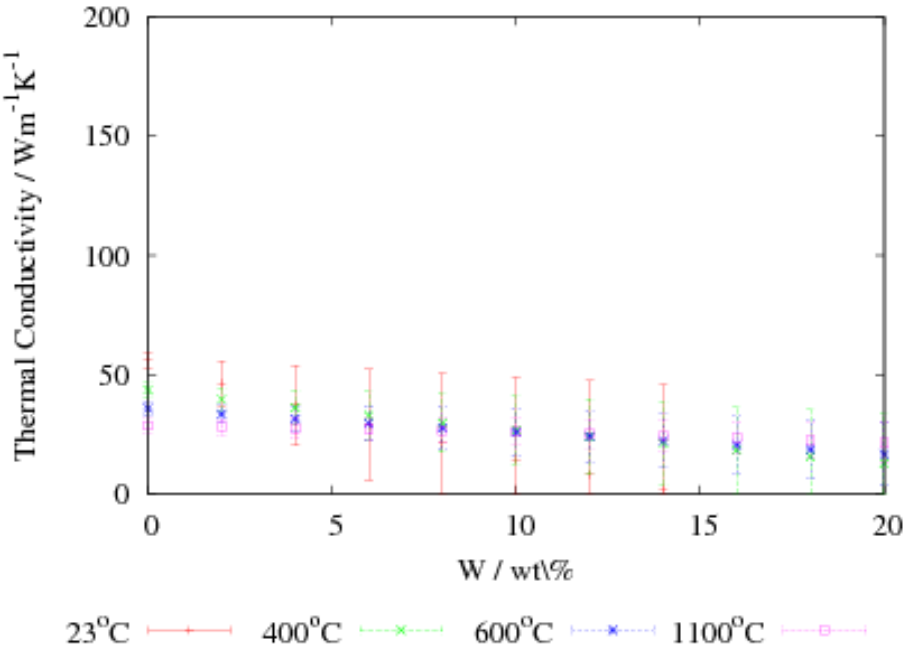

Figure 3-30: Predicted influence of tungsten addition to 0.1C-1.5Mn steel at different test temperatures.

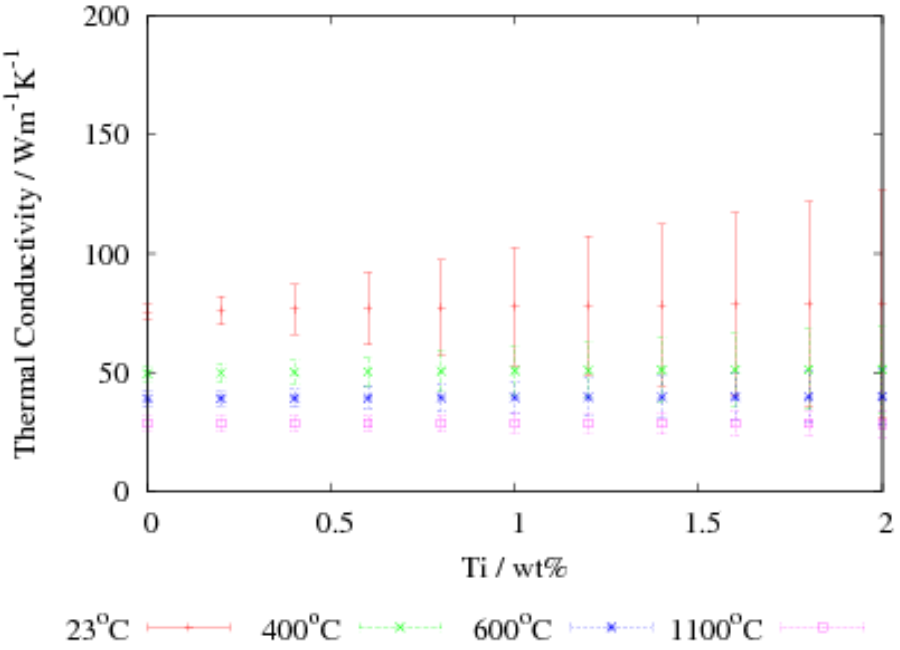

Figure 3-31: Predicted influence of titanium addition to pure iron at different test temperatures.

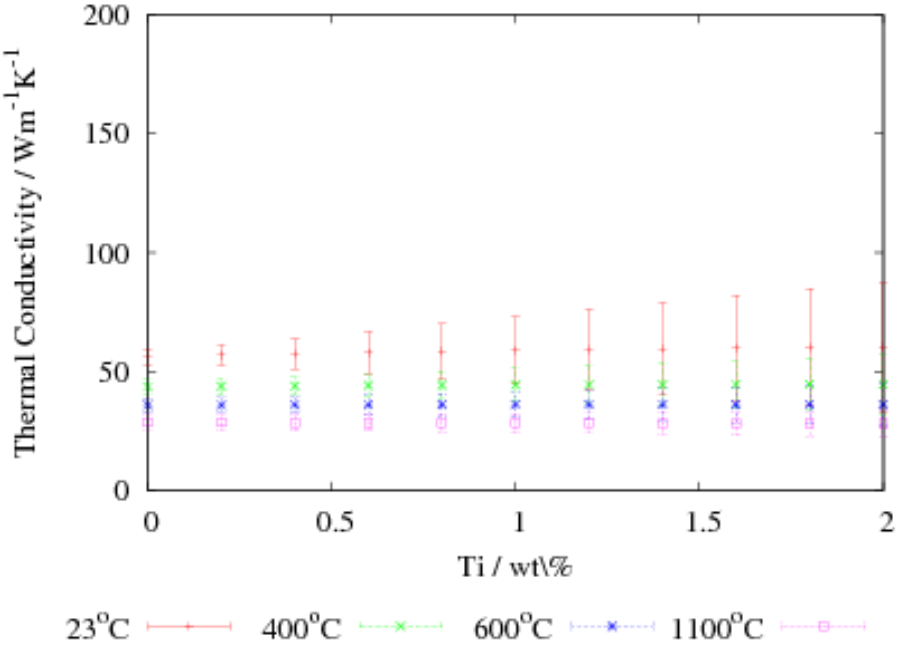

Figure 3-32: Predicted influence of titanium addition to 0.1C-1.5Mn steel at different test temperatures.

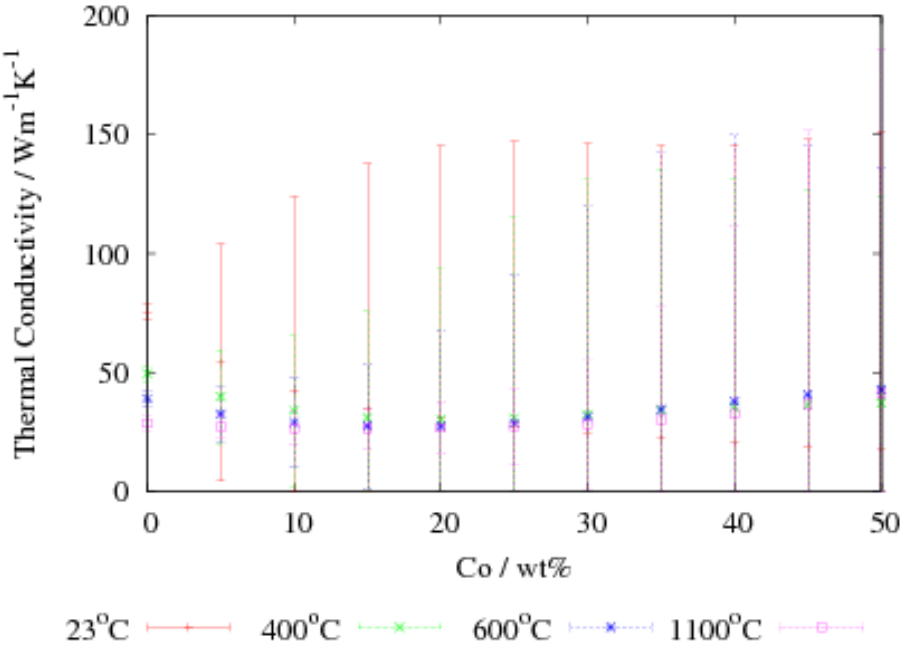

Figure 3-33: Predicted influence of cobalt addition to pure iron at different test temperatures.

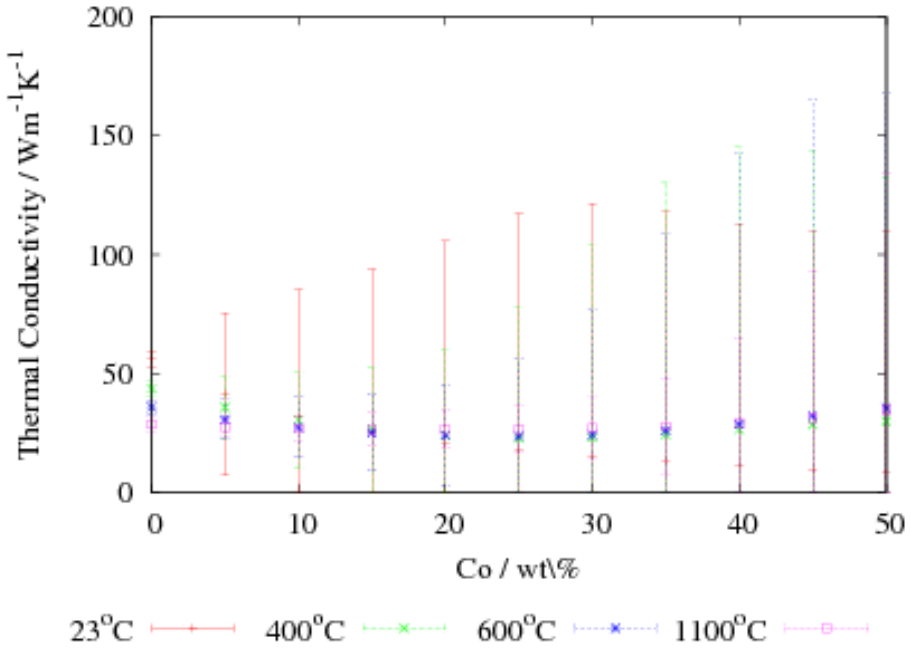

Figure 3-34: Predicted influence of cobalt addition to 0.1C-1.5Mn steel at different test temperatures.

3.7 Predictive ability

The general performance of the model can be tested by predicting on unseen data. The model is found to be able to generalize sufficiently to reproduce the basic trend in the data, and be capable of making useful predictions of unseen compositions (figures 3-35 to 3-40), these were grouped into those within the range of data used for training and those outside the range and this does not necessarily classify them as interpolation and extrapolation because it is possible to have the elements in different combinations, which were not present in the database.

3.7.1 Unseen data within the range of model

Figures 3-35 to 3-38 shows the predictions made to compare against the unseen data given by Holman [70], only the grades of steels were given by this author so some assumptions as to the composition had to be made; the compositions used are shown in table 3-3. Each element is within the ranges shown in table 3-2.

The predictions compare favorably with the reference book data, as shown in the figures, and also with the expected temperature dependence from figure 3-1, reproducing the correct dependence upon temperature for the stainless steel, medium and high carbon steels. The predictions demonstrate that model can predict the correct temperature dependence for these typical compositions of steel.

Another comparison for the prediction of the model was against data for ferritic steel and an austenitic stainless steel used in nuclear industry [107]. In these cases (figures 3-39 to 3-40) it can be seen that the measured values lie

completely within the error bars of the model, even though the exact variation as a function of temperature reported is not matched, particularly for the ferritic steel. The difference in the prediction for the ferritic steel is similar to the experimental difference reported in various papers.

Table 3-4 shows that the perceived error of the model, which represents 1 standard deviation matched well with the root mean squared error, in the ideal case the two values should be equal. The model overestimated the error for unseen data, but the fact that the model indicated the uncertainty is a useful warning.

Table 3-3: Compositions for the steels used to test predictive capability.

Steel	C	Mn	Ni	Mo	V	Cr	Cu	Al	Nb	Si	W	Ti	Co
Fe-18Cr-8Ni	0.15	0.35	8	0	0	18	0	0	0	0	0	0	0
Fe-0.5C	0.5	0.5	0	0	0	0	0	0	0	0.25	0	0	0
Fe-1C	1	0.5	0	0	0	0	0	0	0	0.25	0	0	0
Fe-1.5C	1.5	0.5	0	0	0	0	0	0	0	0.25	0	0	0
Ferritic steel	0.2	0.2	0.5	1	0.5	12	0	0	0	0.25	0.5	0	0
Austenitic steel	0.04	2	15.5	2	0	13.5	0	0	0	0.75	0	0.25	0

Table 3-4: The prediction ability of the model against the unseen data.

Data set	Perceived error	Root mean squared error
Unseen data within the range of model.	5.5	6.1
Data beyond range of model.	82.3	50.8

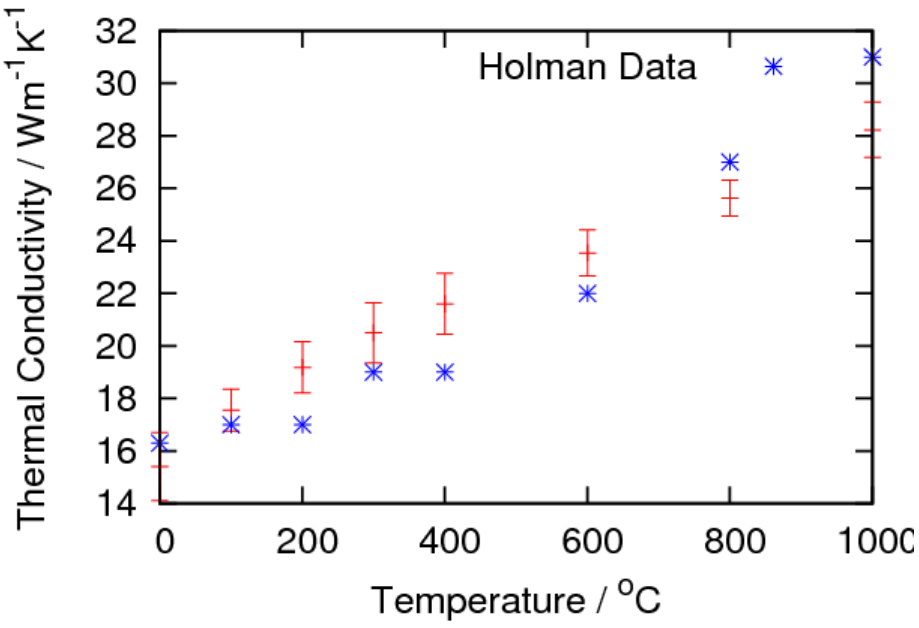

Figure 3-35: Prediction for an 18-chromium 8-nickel stainless steel.

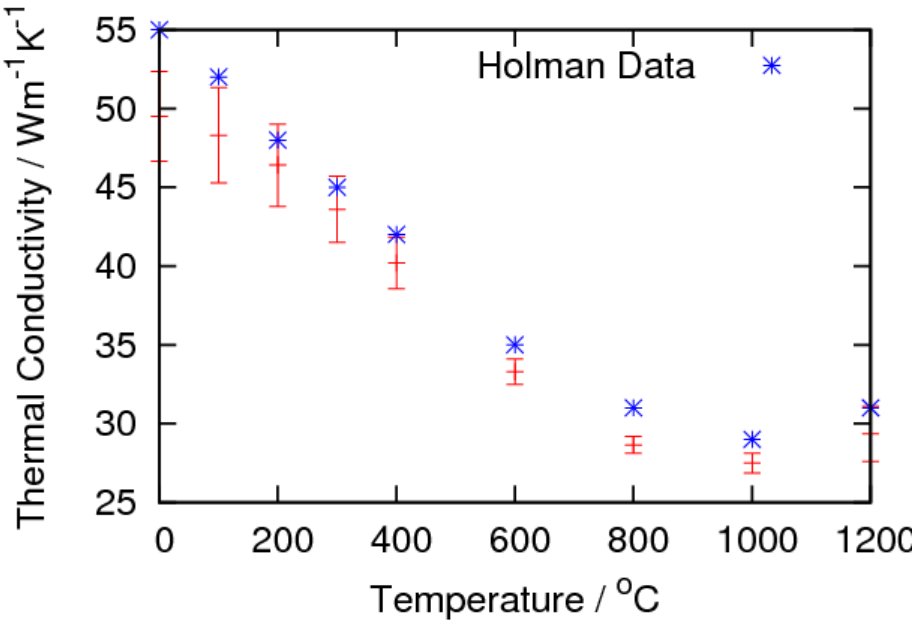

Figure 3-36: Prediction for 0.5wt% Carbon steel.

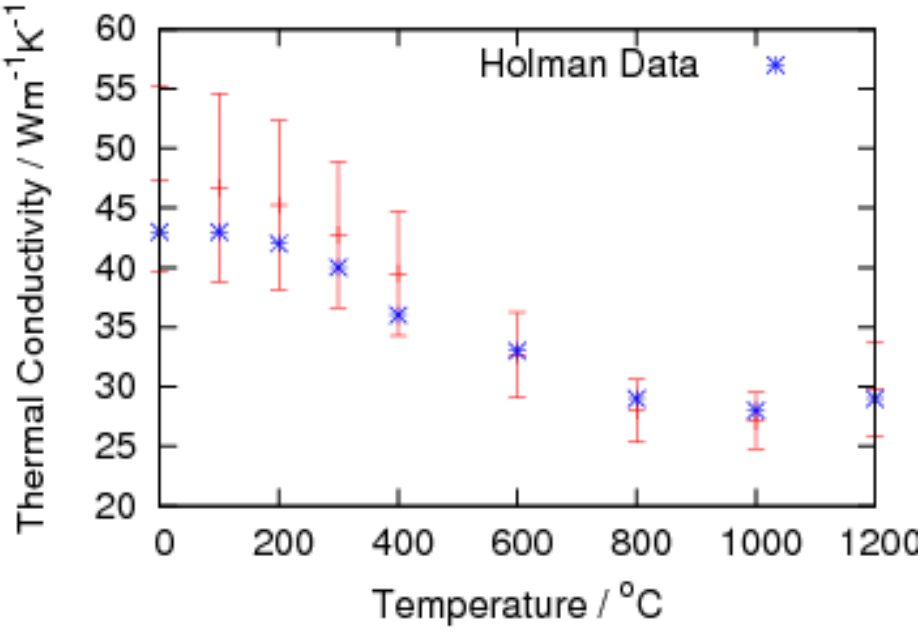

Figure 3-37: Prediction for a 1wt% carbon steel.

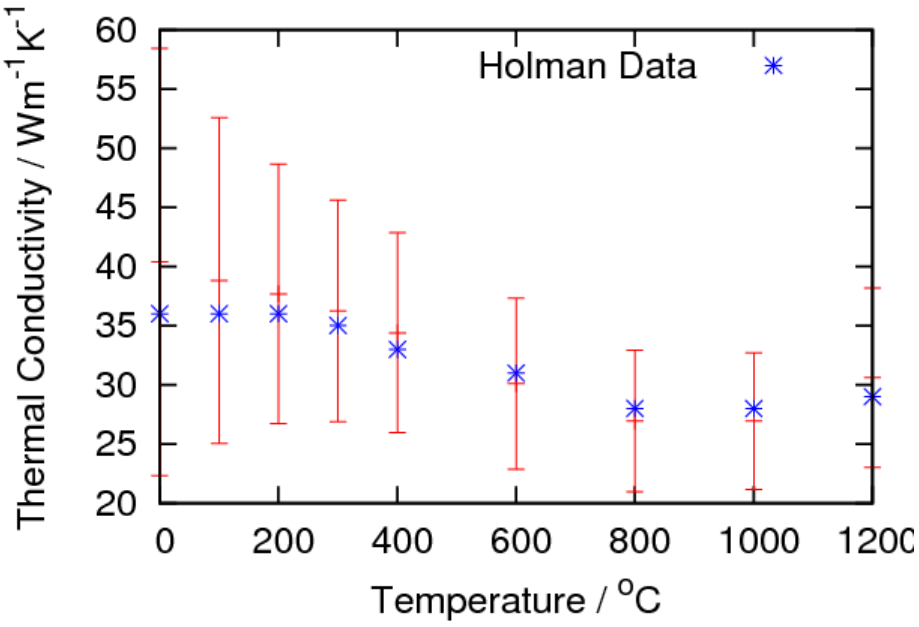

Figure 3-38: Prediction for a 1.5wt% Carbon steel.

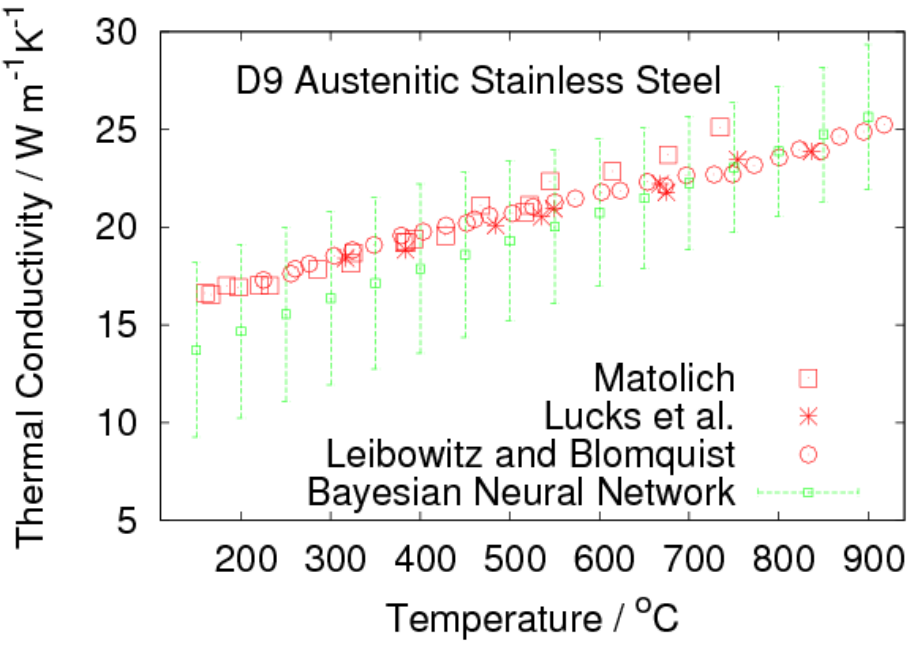

Figure 3-39: Prediction for austenitic stainless steel.

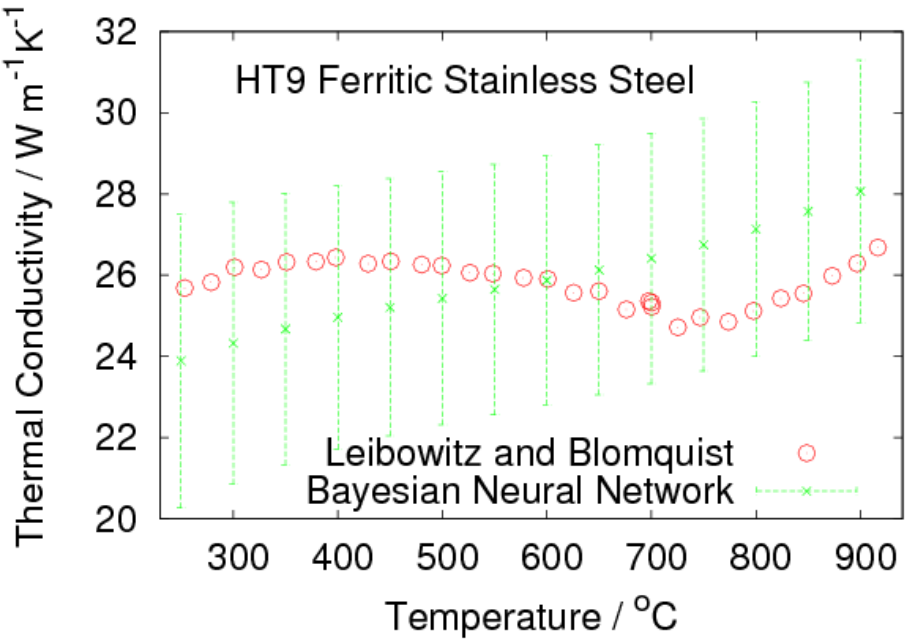

Figure 3-40: Prediction for ferritic stainless steel.

Summary

A model of thermal conductivity has been produced to provide the necessary data for general prediction of quenching behavior. The model is naive in that it has no explicit knowledge of all the physical phenomenon which should determine the thermal conductivity, the biggest omission is that no knowledge of the previous thermal history was included, which is known to affect the microstructure and therefore the thermal conductivity. This was on one hand omitted to allow simple application of the model, secondly to simplify the modelling procedure, and thirdly to allow the greatest amount of data to be incorporated in the model. The error bars of the model are a key feature, indicating the level of certainty in the values predicted.

Chapter 4

Experimental work

4.1 Introduction

A calculation of the heat transfer coefficient needs accurate data for the temperature history within the sample. In this chapter, the design of the probe and the quenching system used to generate the necessary data (cooling curves) for steels is described. Experimental details such as the preparation of the probe and the method for analysing the collected data are also described. Figure 4-1 shows the details of the experimental work as a flow chart, showing the factors considered in the design of the experiments and summarising the test conditions.

4.2 Quenching system design

Previous researchers have utilised a multitude of probe techniques to predict the heat transfer coefficient (as discussed in chapter 1), but probe dimensions of less than 10 mm are not often used because of the difficulty of temperature control during the transfer from the furnace to the quench bath.

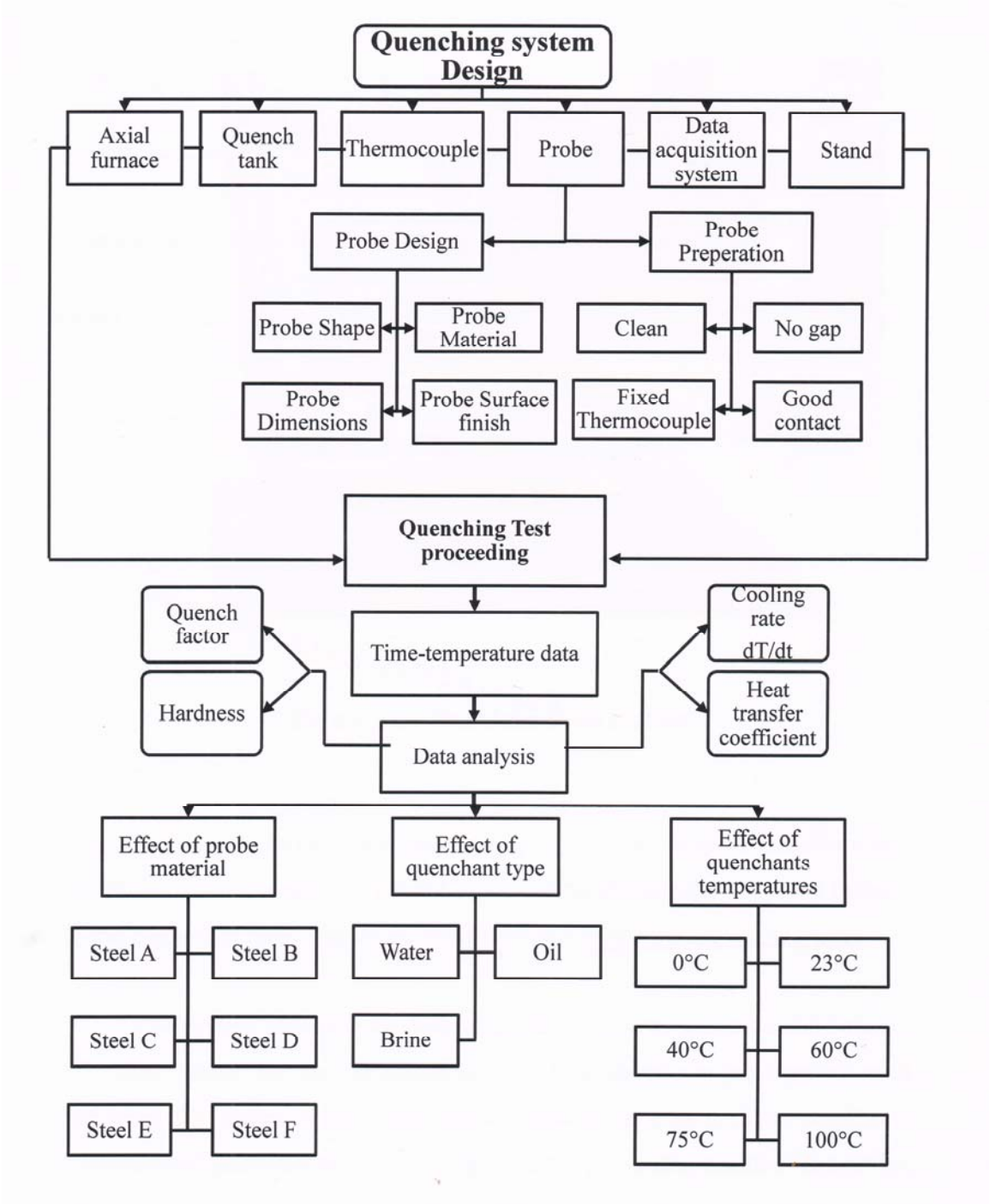

Figure 4-1: Flow chart details for the experimental work.

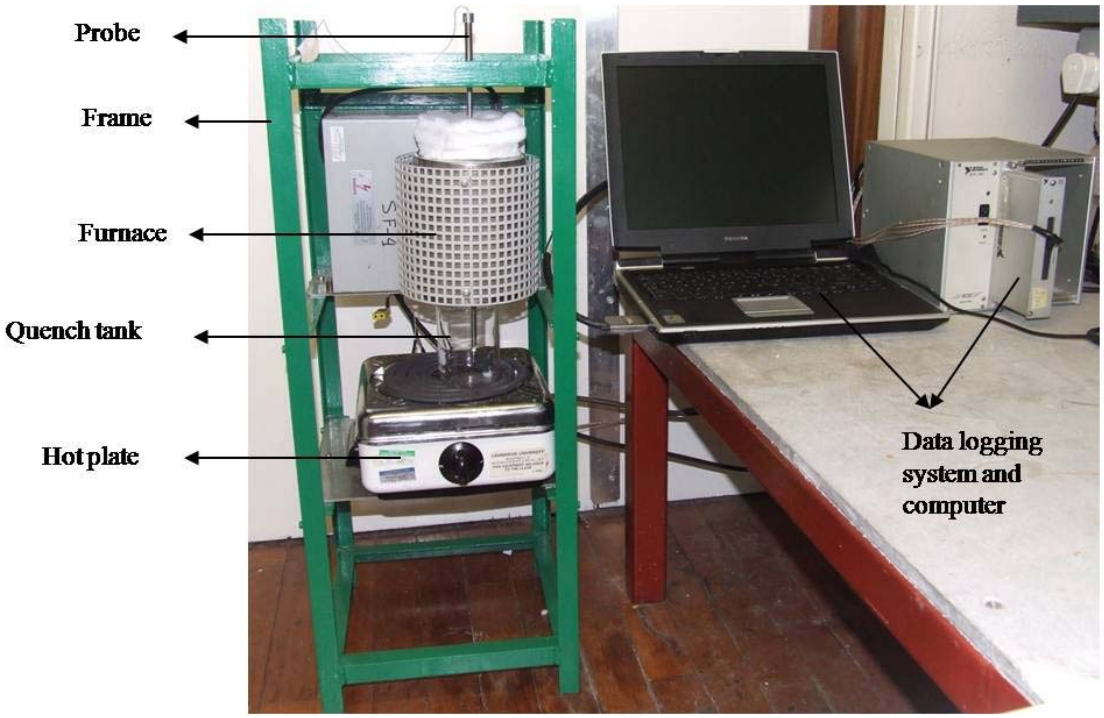

Figure 4-2: The Quenching system.

In this work, a controlled quenching system was designed to ensure that the probe is not excessively cooled in air during the transfer from the furnace to the quenchant tank. Figure 4-2 illustrates the experimental arrangement.

The system consists of a data- acquisition system, a small axial furnace, 0.25 litre beaker for the quenchant and a K-type thermocouple inserted in to the geometric centre of the probe where it is held in place by a 35 cm steel tube. This allowed temperature data to be taken at the geometric centre of the probe. The tube also acts to guide the movement of the probe as it is dropped, and increases the probe transfer speed from inside the furnace to the quenchant tank using gravity.

All components were held in place by a stand to guide the probe as it is traversed from the middle of the furnace to the middle of the quench tank, as shown in figure 4-2.

4.2.1 The furnace

Carbolite axial furnace with maximum operating temperature 1000°C, inside diameter is 2.5 cm, and heated length 13 cm is placed in the frame as shown in figure 4-2 to allow the probe to transfer from the furnace to the quench tank.

4.2.2 Quench tank

A 0.25 litre glass beaker is used as a quench tank. This size of beaker is enough to keep the quenchant temperature with no significant change during the quenching process.

4.2.3 The thermocouple

A 1 mm diameter, 1 m long K-type inconel 600 sheathed thermocouple is used for time-temperature data recording. The thermocouple is inserted to the geometric centre of the probe through a side hole at the upper end (figure 4-3). And a screw is used to fix it in position.

The response time of the thermocouple used is sufficiently short in order to register the change during quenching of the probe.

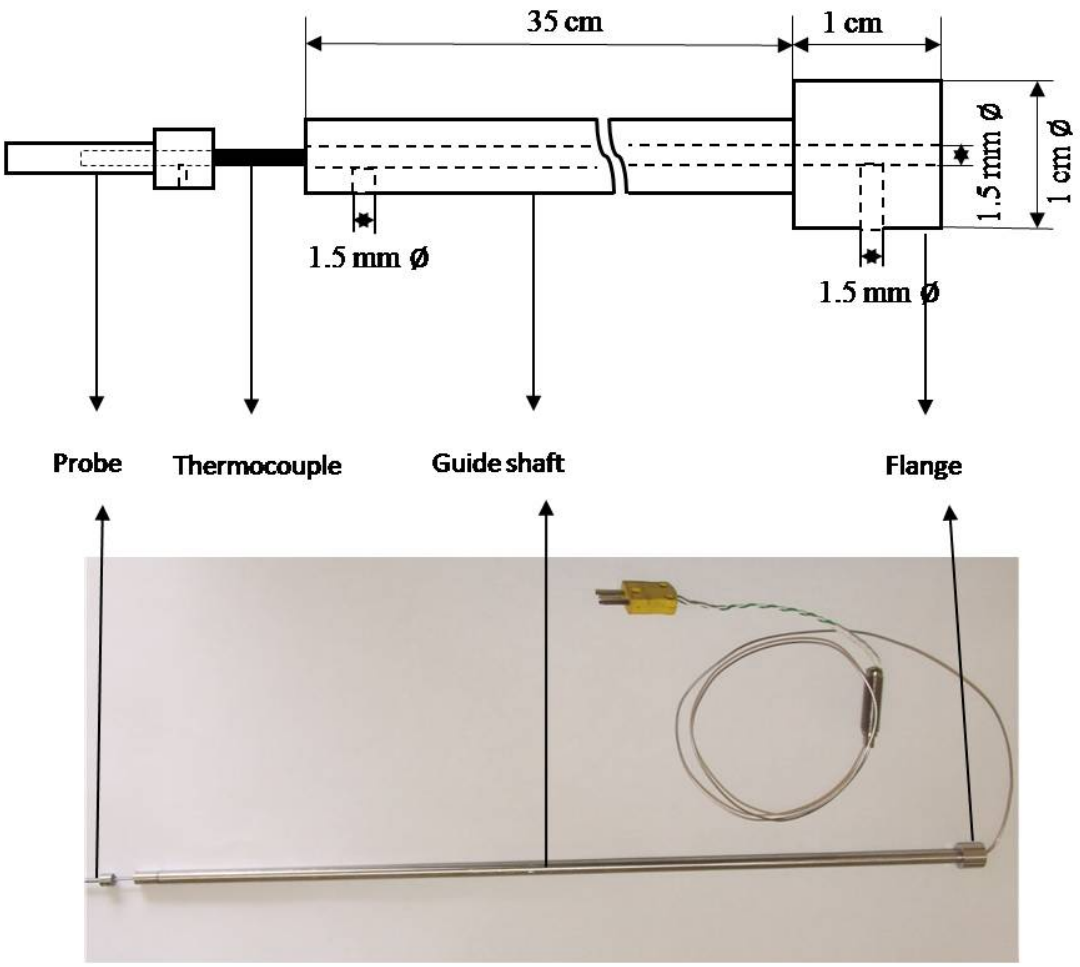

Figure 4-3: The arrangement of probe, thermocouple and guide shaft. The 1 mm shielded thermocouple passes through centre of guide shaft and into the probe.

4.2.4 Data acquisition system

National instruments SCXI-1000-1328 data acquisition system with a Virtual bench-logger software and computer was used to collect the time-temperature data from the thermocouple inside the probe during the quenching process.

The thermocouple is connected to the connector box which is connected to the computer via National Instrument DAG card- 6036E. The connector can accommodate a maximum of 4 thermocouple connections. Data were collected every 0.001 s.

4.2.5 The probe

4.2.5.1 Probe materials

The probe was made from different alloy steels (table 4-1) in order to characterise its cooling rates and the heat transfer coefficients and to ensure that the coupling of heat flow and structural transformations can be obtained.

Table 4-1: Chemical composition in wt%.

Steel	C	Si	Mn	Ni	Mo	Cr	Al	Co	Cu	V	Pb	Ti	Sb	P	S
A	0.16	0.16	0.67	0.08	0.02	0.06	-	-	-	-	-	-	-	-	-
B	0.15	1.19	1.5	0.08	0.31	1.19	0.02	-	0.136	-	-	-	-	-	-
C	0.78	1.6	2.02	-	0.25	1.01	1.37	3.87	-	-	-	-	-	-	-
D	0.55	0.22	0.77	0.15	0.05	0.2	-	-	-	0.001	-	-	-	-	-
E	0.54	0.2	0.74	0.17	0.05	0.2	-	-	-	0.001	-	-	-	-	-
F	0.16	0.22	0.3	2.93	0.389	1.47	0.28	-	0.01	0.004	0.001	0.003	0.001	0.013	0.011

4.2.5.2 Probe dimensions

The probe was designed using the lumped heat capacity method (as discussed in chapter 2) to be able to justify an assumption of uniform probe temperature during the cooling process. The dimensional quantity plays an important role in assessing the applicability of the lumped capacitance method. Essentially, with $Bi \leq 0.1$, the results are expected to yield reasonable estimates within about 5%.

$$Bi = \frac{h\, L_c}{k} \tag{2.4}$$

The thermal conductivity values for the steels are about 50 W/ m °C [17] while the maximum heat transfer coefficient value expected is 10000 W/ m^2 °C for quenching in agitated water. By using the above values for k and h, and 0.1 for the Bi number in equation 2.4, it is possible to calculate the appropriate dimensions for the probe for measuring the heat transfer coefficient for steels in different quenching conditions (figure 4-4).

The length of the probe is 5 times its diameter in order to neglect heat extraction through the ends of the cylinder, consistent with the supposition that at the half length cross-section only a radial-symmetrical heat flow exists.

Because the objective of cooling curve analysis is to measure the ability of the quenchant to attenuate heat transfer under various conditions, it is desirable that the experiment is not perturbed by the measurement process itself; therefore, a probe with “semi- infinite” dimensions is usually selected.

4.2.5.3 Probe surface finish

The surface finish of the probe is kept standard by machining and grinding all the probes surface in the same way before quenching, in order to avoid any additional effect for the surface roughness.

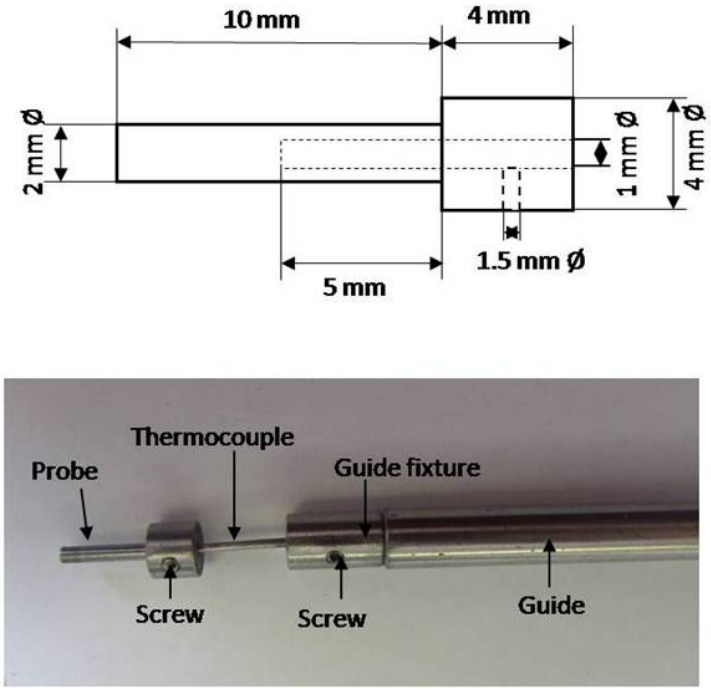

Figure 4-4: The design and the dimensions of the probe, showing positioning of thermocouple within the probe, and details of fixture.

4.3 Probe preparation and test procedure

1. The probe was cleaned using an ultrasonic cleaner for 30 min before quenching in order to avoid surface contamination between the thermocouple and the probe surface, to insure good contact to measure the necessary temperature.
2. A small amount of fine graphite powder was used in order to attain better contact between the thermocouple tip and the probe.
3. Alumina paste was used to seal the gap between the probe and the thermocouple in order to avoid the leakage of the quenchant solution into the thermocouple, which can cause the thermocouple to cool faster than the probe and result in erroneous readings. The alumina was applied and furnace hardened for 8 h at 200°C.
4. The furnace was set to 850°C and held there for 10 min, which is the time needed to reach 850°C.
5. The probe and guide shaft was inserted through the guide hole holding the thermocouple in the centre of the furnace for 4 min, this period of time is enough to reach the designed quenching temperature.
6. The thermocouple is connected to the data logging system and the data logging is started with scan rate 1000 scan/s.
7. The probe and guide shaft assembly is released and falls under gravity until the probe enters the quenching tank when the stopping flange reaches the guide hole in the holding frame.
8. The data logging system was switched off after the thermocouple reading reached the quenchant temperature.
9. The used probe was removed from the end of the guide shaft, replaced with an unused probe for the next test.

4.4 Data analysis

A minimum of three quenching experiments were performed to test the repeatability of probe for each condition. In each experiment, many thousands of data points were collected; to avoid the effect of noise, the data were smoothed using a rolling average of 11 points before plotting or using in the analysis. The smoothed data were used to calculate the cooling rate which is the first derivative as a function of temperature. The cooling rate is then used as an input in the inverse heat conduction model to estimate the heat transfer coefficient at the metal/quenchant interface.

4.5 Experimental plan

4.5.1 Different steel compositions

The quench test was repeated many times using probes made from different steels to show the dependence of the heat transfer coefficient on steel composition.

4.5.2 Different quenchant type and quenchant temperatures

Different quenchant type and different quenchant temperatures were used to determined the effect of the type and the temperature on the results, table 4-2 shows the testing conditions during the experimental work.

Table 4-2: Quenching test conditions.

Quenchant type	Quenchant temperature / °C					
Water	0	23	42	60	75	100
Oil	20	85	150			
Brine	20	70	100			

4.5.3 Case study

A cylindrical sample was used to demonstrate the validity of the calculated heat transfer coefficient using the modelling techniques and to assess its applicability to different dimensions. The sample was with 52 mm diameter and 20 mm length, and with three K-type thermocouples inserted as illustrated in figure 4-5 (geometric centre-midpoint between the centre and the surface –1 mm from the surface). The thermocouples were connected to the data logger to record the cooling curves during the quenching process. The cooling curves were then analysed to predict the hardness profile in the sample.

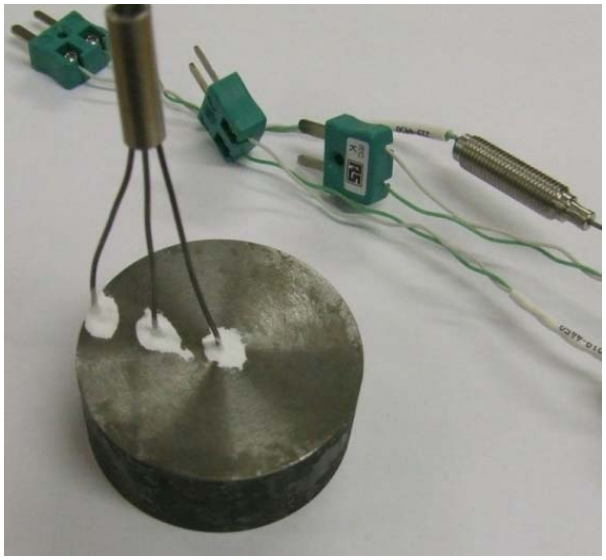

Figure 4-5: The cylindrical sample with three inserted thermocouples.

Chapter 5

Results and discussion

5.1 Calculating of cooling rates and heat transfer coefficients for different composition steels:

Accurate modelling of quenching process necessitates that the heat transfer coefficient must be treated as a function of the surface temperature as previously shown in Chapter 3. To investigate the generality of the methods developed in the work described in Chapter 4, different composition steel probes were used to record the cooling curves during quenching into water at 23°C as shown in table 4-1.

Figure 5-1 shows the recorded cooling curve of the probe made of steel A, along with the corresponding cooling rate curve (*dT/dt*). Data were collected with a resolution of 0.001 s. To deal with noise the data were smoothed using a rolling average of 11 points before plotting.

The cooling curve was used to calculate the cooling rate and the heat transfer coefficient as a function of surface temperature, as described in Chapter 2.

Used in the simplest way, the heat transfer coefficient at a fixed temperature represents the potency of the quenchant and can be used as a convenient comparison of different media or quenching conditions. However, by representing the heat transfer coefficient by a function dependant on temperature; it can be used as a boundary condition in the simulation of cooling processes, as will be demonstrated later in this Chapter.

From figure 5-2 it is evident that the maximum heat transfer coefficient (h_{max}) during the quenching of steel A in water at 23°C occurs at around 200°C while the highest heat transfer coefficient in the pearlite transformation temperature range between 700 and 500°C is 3500 W m^{-2} K^{-1} .

Figures 5-3 to 5-12 show the recorded cooling curves and the heat transfer coefficients as a function of the surface temperature for different steel probes during quenching in water at 23°C.

Steel A

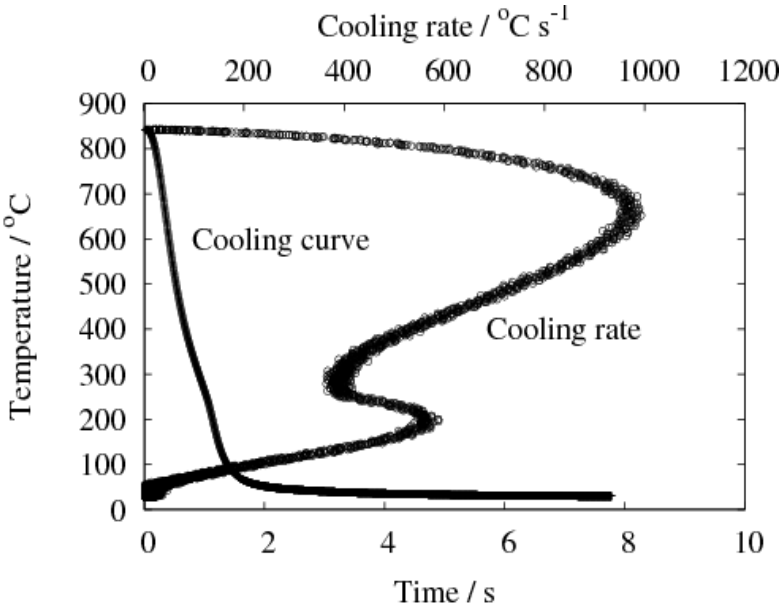

Figure 5-1: Cooling curve and derived cooling rate curve for steel A quenched in 23 °C water.

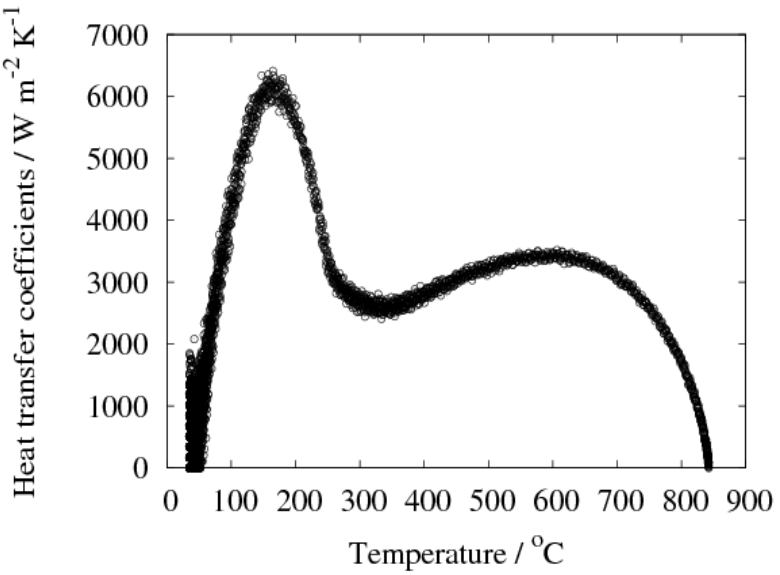

Figure 5-2: Heat transfer coefficient for steel A as a function of surface temperature during quenching in water at 23°C.

Steel B

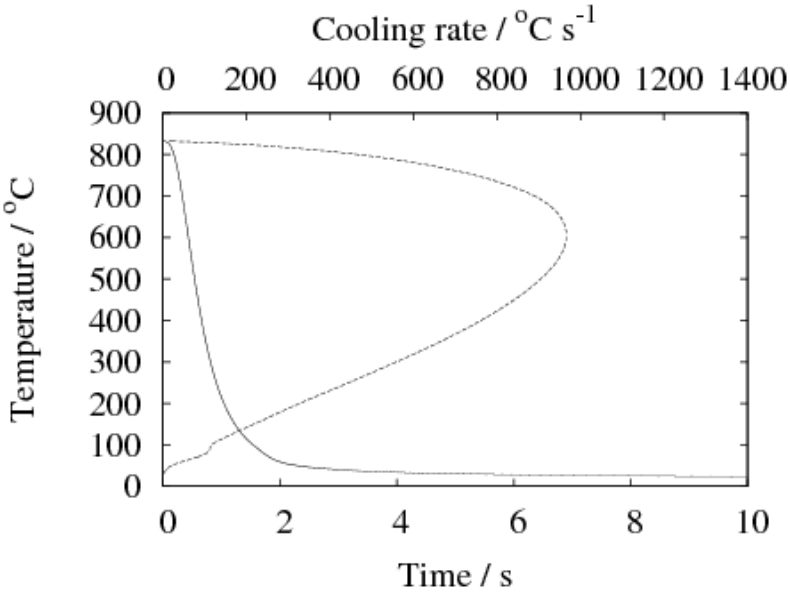

Figure 5-3: Cooling curve (solid) and derived cooling rate curve for steel B quenched in 23 °C water.

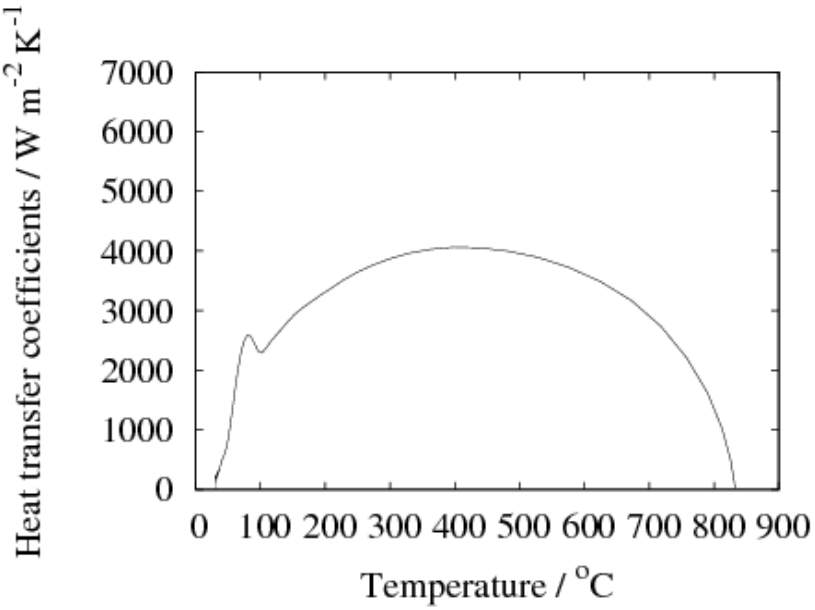

Figure 5-4: Heat transfer coefficient for steel B as a function of surface temperature during quenching in water at 23 °C.

Steel C

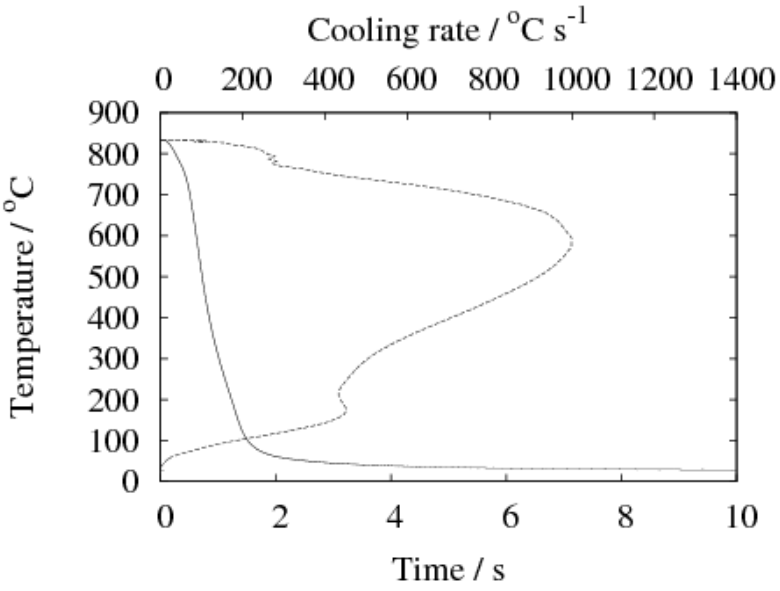

Figure 5-5: Cooling curve (solid) and derived cooling rate curve for steel C quenched in 23 °C water.

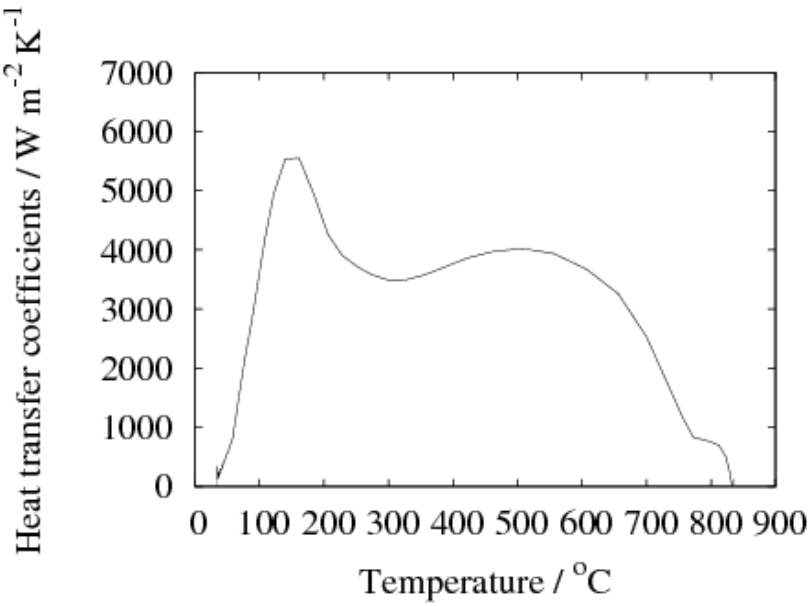

Figure 5-6: Heat transfer coefficient for steel C as a function of surface temperature during quenching in water at 23 °C.

Steel D

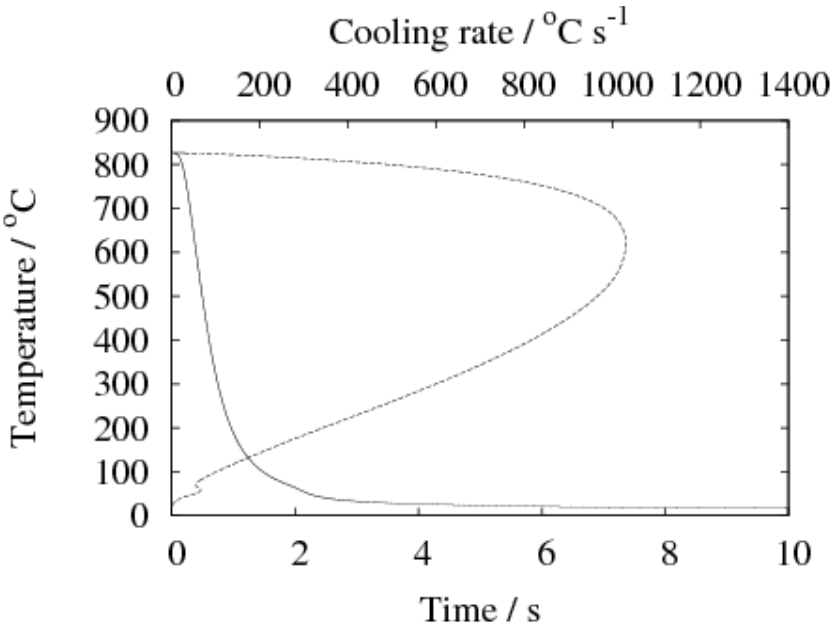

Figure 5-7: Cooling curve (solid) and derived cooling rate curve for steel D quenched in 23 °C water.

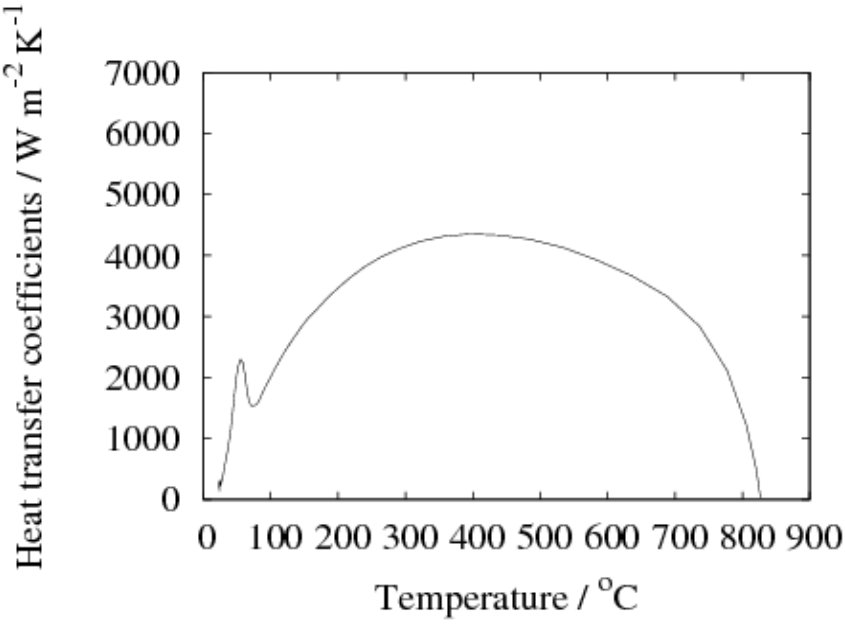

Figure 5-8: Heat transfer coefficient for steel D as a function of surface temperature during quenching in water at 23 °C.

Steel E

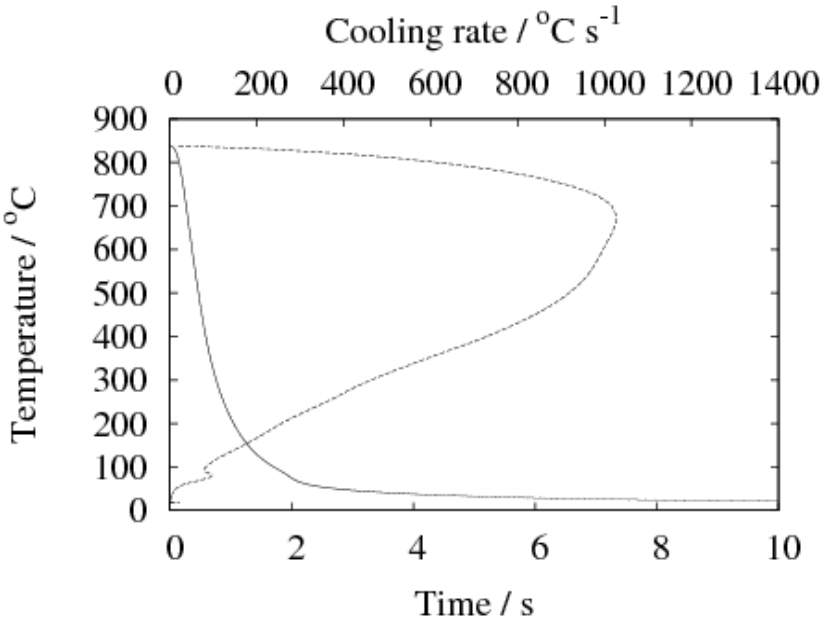

Figure 5-9: Cooling curve (solid) and derived cooling rate curve for steel E quenched in 23 °C water.

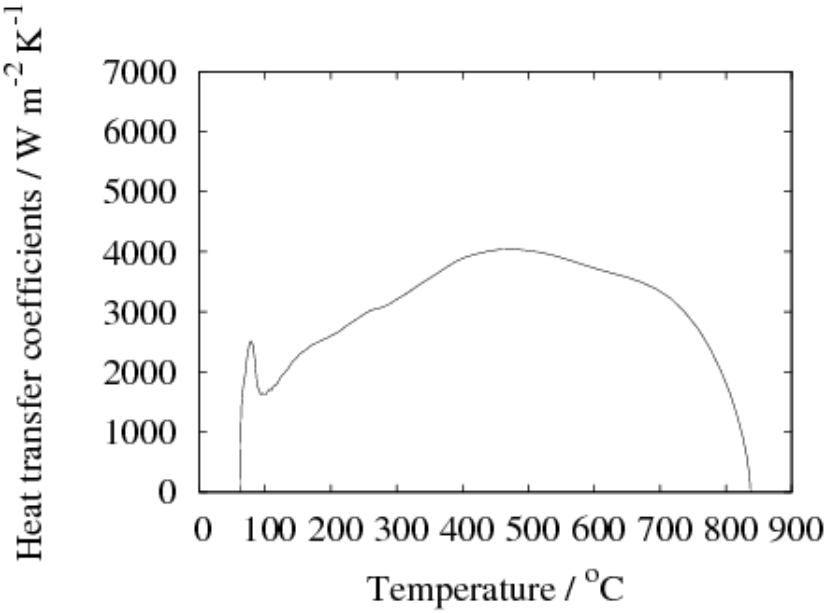

Figure 5-10: Heat transfer coefficient for steel E as a function of surface temperature during quenching in water at 23°C.

Steel F

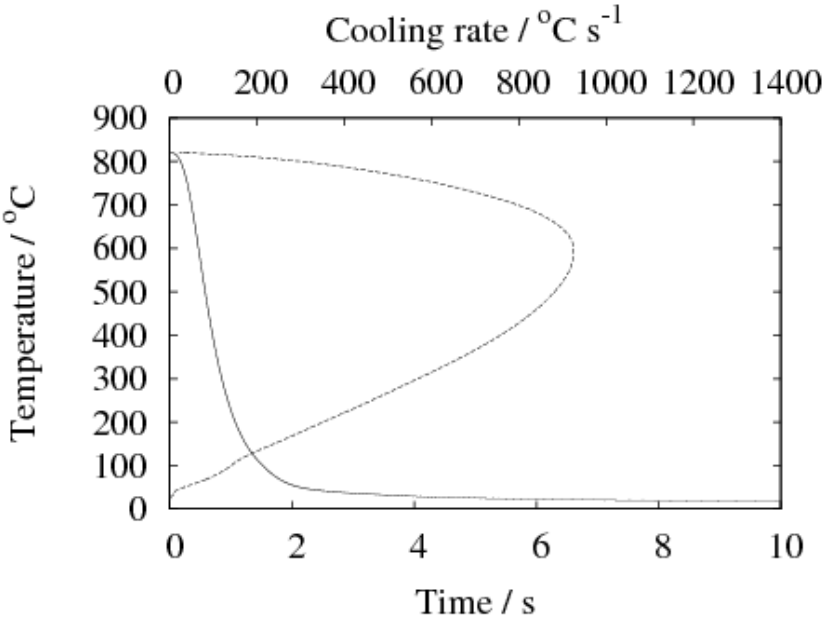

Figure 5-11: Cooling curve (solid) and derived cooling rate curve for steel F quenched in 23 °C water.

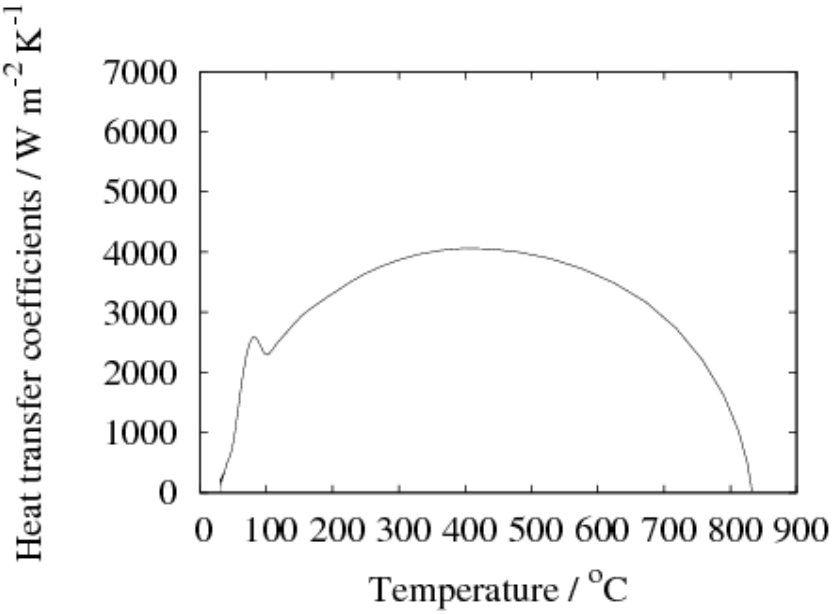

Figure 5-12: Heat transfer coefficient for steel F as a function of surface temperature during quenching in water at 23 °C.

Figure 5-13 shows all the derived cooling rate curves for the steels used together with the heat transfer coefficients; The essential characteristics of these curves are similar, especially in the range 600 to 850 °C where usually pearlite forms; Steel A has a lower heat transfer coefficient than the other steels indicating ferrite formation due to its low carbon steel.

However, there are important differences with respect to alloys A and C, both of which have exhibited a high cooling rate during the quench at temperatures below about 400°C (Fig. 5-13). Alloy A does not have sufficient hardenability in order to ensure a fully martensitic microstructure on quenching (Fig. 5-14. a); the sample has a hardness of only 260 HV in its final state (Table 5-1). Allotriomorphic ferrite forms at high temperatures, so that the amount of austenite which undergoes martensitic transformation is reduced, resulting in a smaller enthalpy change and hence a faster cooling rate (relative to those alloys which become fully martensitic) at low temperatures during the quench.

In the case of alloy C, the hardenability is sufficient to yield a martensitic microstructure (Fig. 5-14. a); with a hardness of 753 HV (30 kg), but calculations using MTDATA software revealed that the enthalpy change at the M_S = 202 °C for alloy C is ΔH = 4600 J mol^{-1}, which compares with ΔH = 6000–7000 J mol^{-1} for the other steels (Fig. 5-15) The smaller release in heat on transformation is consistent with the more rapid cooling rate at low temperatures for alloy C.

In steel B and F although the carbon content is the same as steel A but the alloying elements are much higher which increase their hardenability as shown in the hardness results in table 5-1; In these steels the hardness of the probe is almost the same as the hardness of the fully martensitic structure (the measurement of the fully martensitic structure hardness is described in section

5.2.1.4). Figure 5-14. b shows also that the microstructures for these steels are martensite.

Table 5-1: Hardness results and the critical temperatures for the steels.

Steel type	M_s/°C	Hardness	Maximum Hardness	A_{e1}/°C	A_{e3}/°C	% Austenite at 830 °C[1]
Steel A	455	260± 8.6	351±7.6	705	835	96
Steel B	435	456±33.8	471±5.9	725	875	100
Steel C	202	753±2	748±7.3	780	915	100
Steel D	269	728±13	731±0	715	750	100
Steel E	276	735±15	720±5.5	715	750	100
Steel F	405	458±6.8	473±13.4	700	770	100

Actually the latent heat of transformation is not taken into account in this research, although this is less than associated with melting and solidification, it does affect the temperature field and transformation through thermal transients extending throughout the body of the sample, even at positions away from the quenchant. The latent heat and the phase-transformation fraction affect each other (figure 1-1), and may be a suitable topic for future research to improve the model by including the latent heat in the calculations, in this case the equation for heat transfer coefficient should represent always the maximum values we observed.

With the current model the problem is solved by using a probe from the same material of interest to obtain the equation of heat transfer coefficient as a function of temperature, which is needed as a boundary condition to simulate

[1] The values for A_{e1}, A_{e3} and % Austenite at 830 (the thermpcouple reading) are calculated using the MTDATA software depending on their chemical compositions (section 2-4-1). Steels B and C made without silicon since MTDATA has been found to give silicon an excessively strong ferrite-forming tendency in the systems of concern [108], these results also verified by mucg program [66].

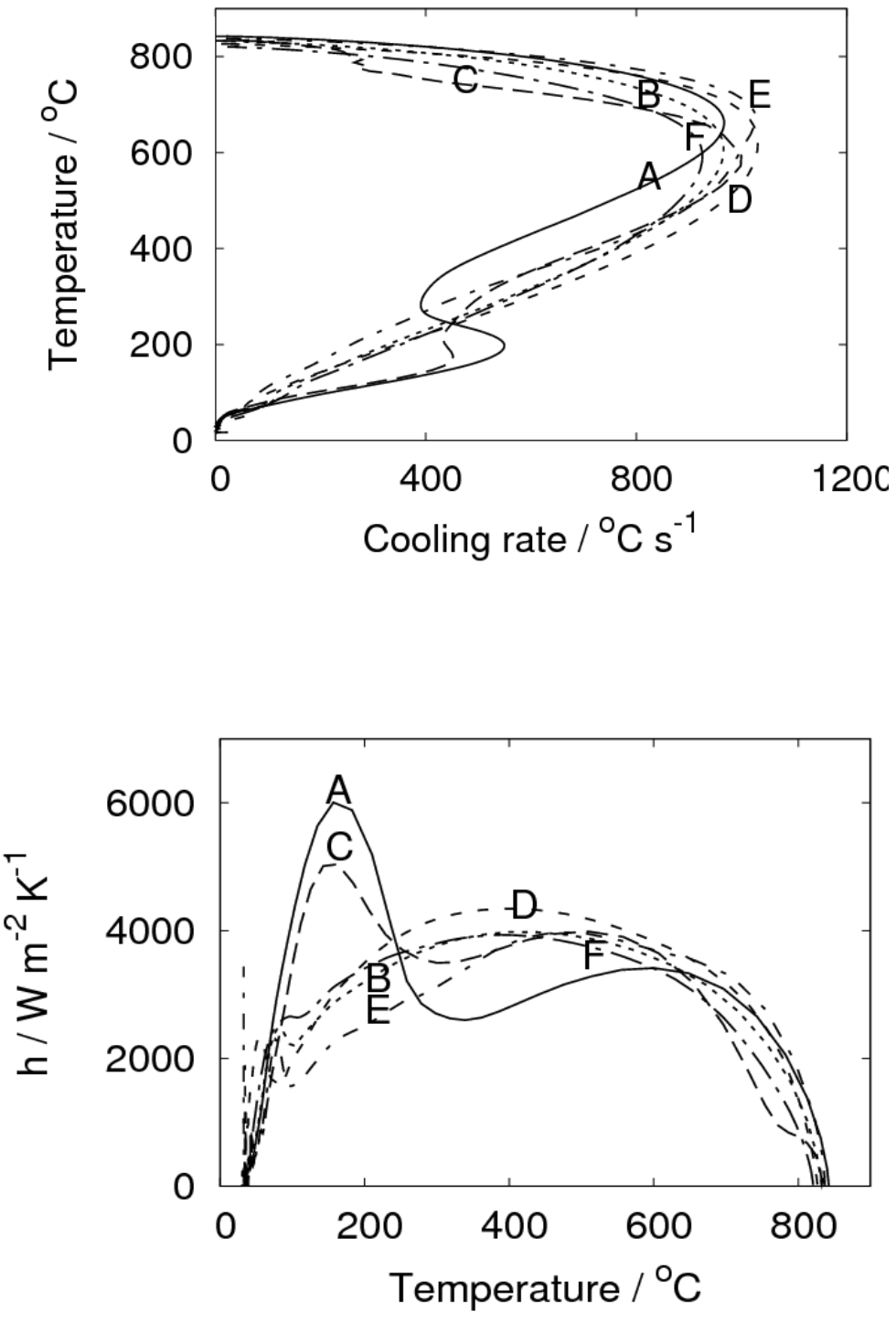

Figure 5-13: Derived cooling rate curves and heat transfer coefficients for different compositions steel probes quenched in 23 °C water.

the quenching process. Otherwise, acceptable results can be obtained by using the equation from any one from the steels (B, D, E, F) in table 4-1.

Figure 5-16 shows the heat transfer coefficient as a function of surface temperature obtained using three different probes: Inconel 600, JIS [31], and the probe designed in this work.

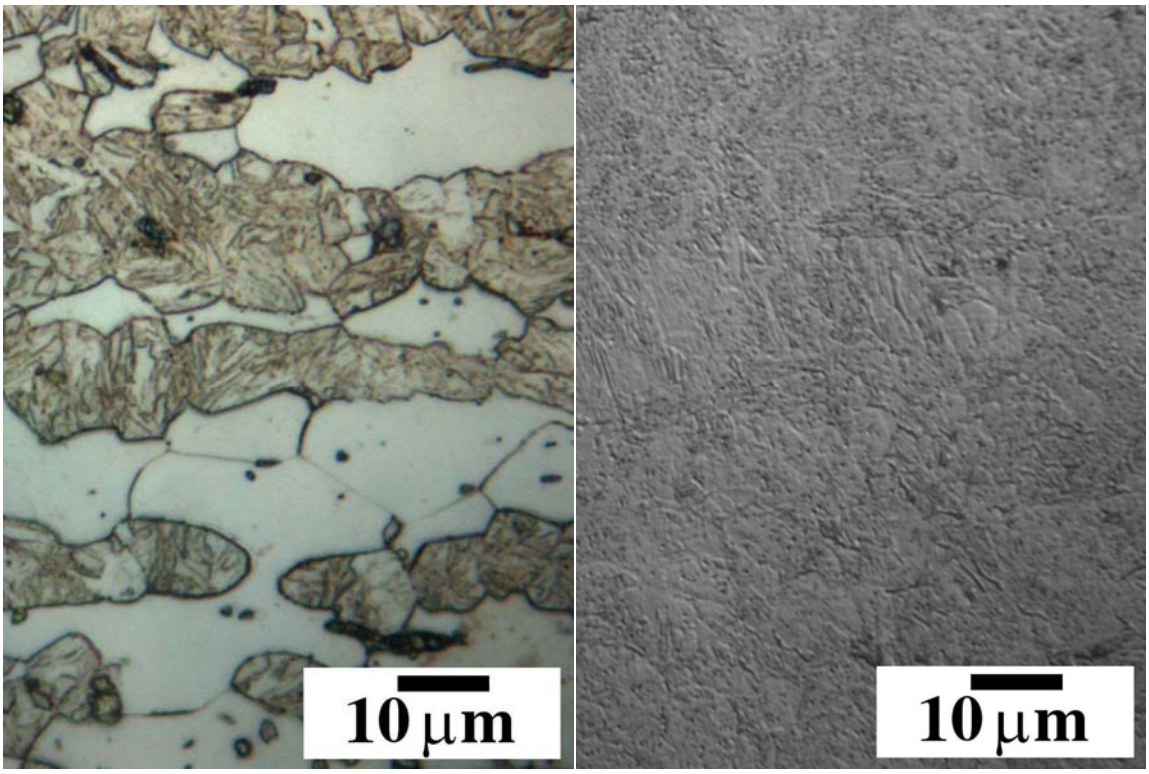

Steel A **Steel C**

a

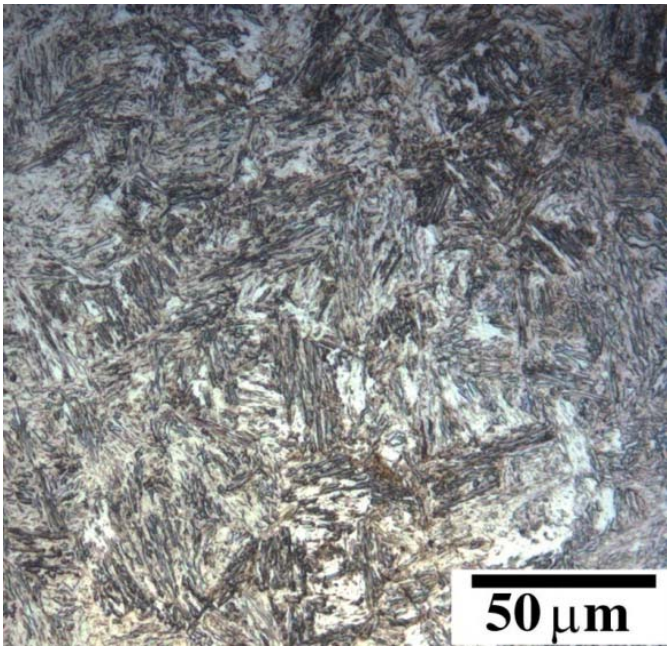

Steel B

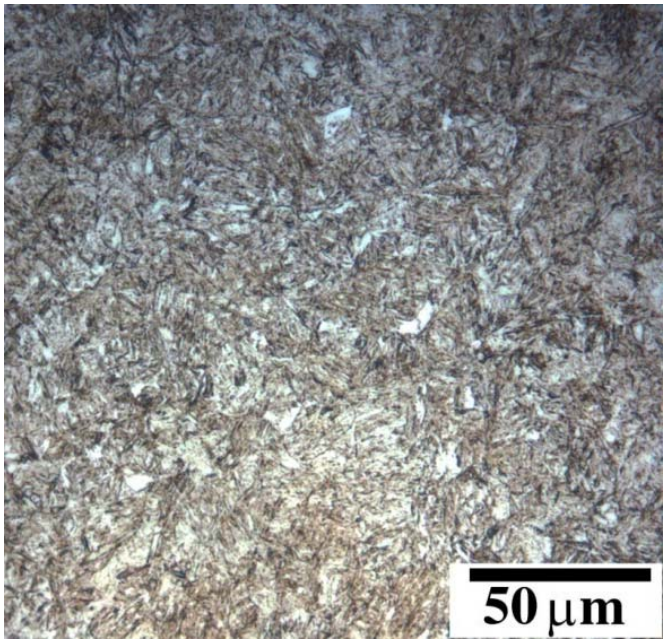

Steel D

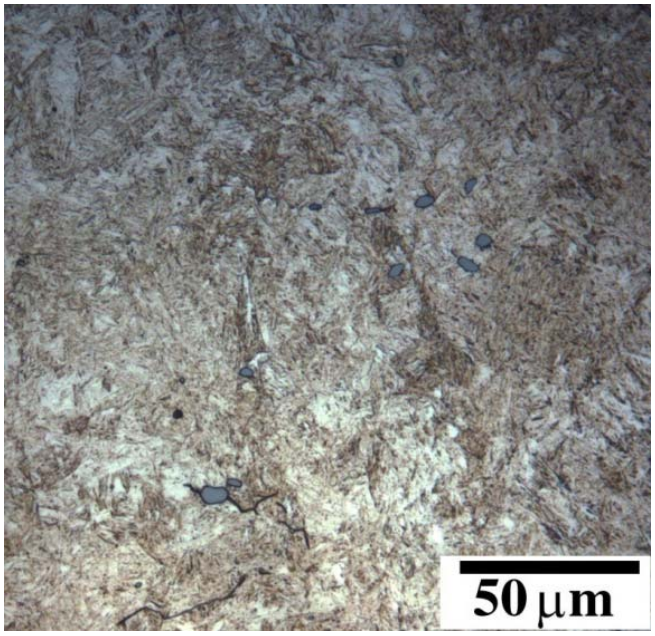

Steel E

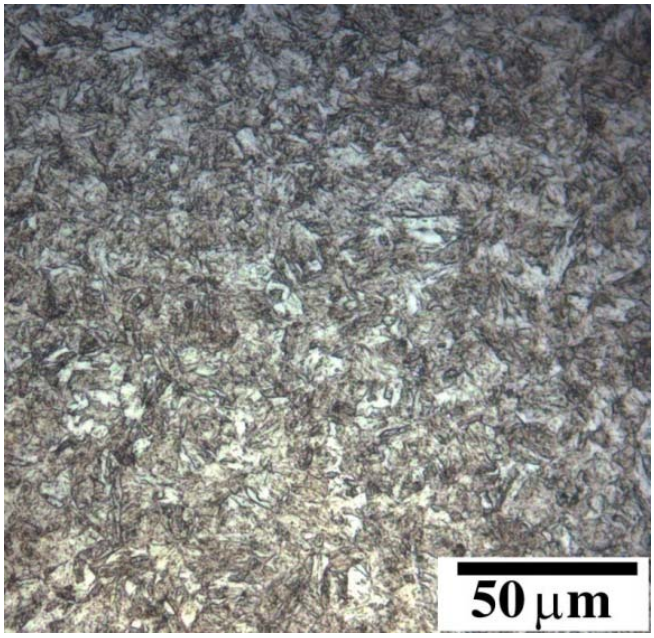

Steel F

b

Figure 5-14: Microstructures for the different steel probes.

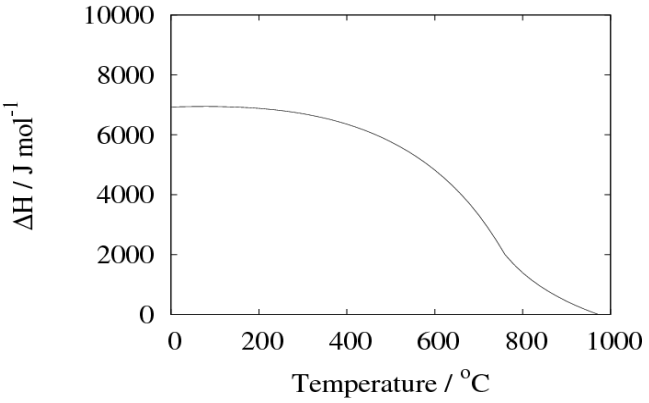

Steel A. M_S=455 °C

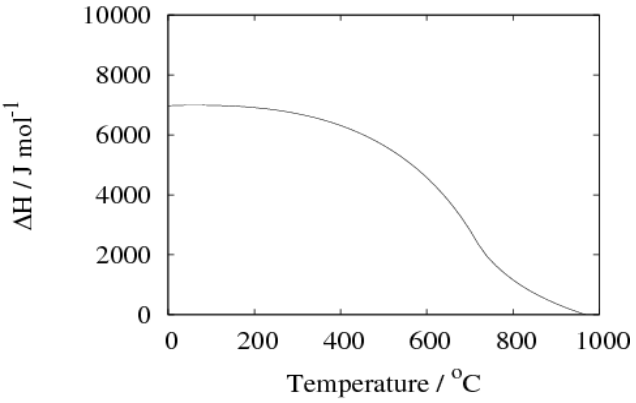

Steel B. M_S =435 °C

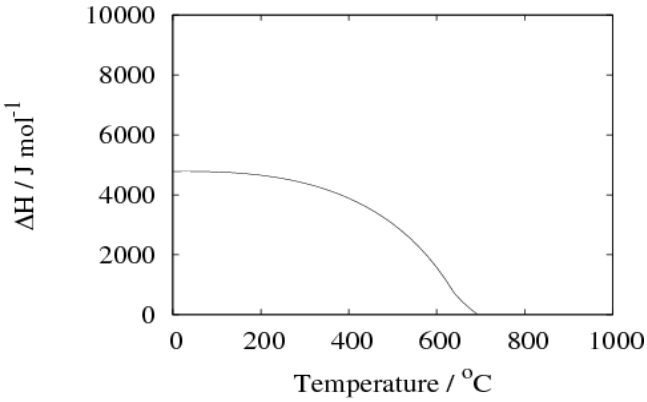

Steel C, M_S =202 °C

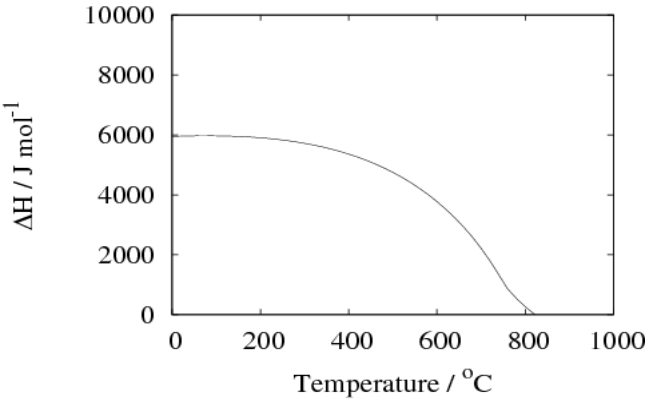

Steel D, M_S =269 °C

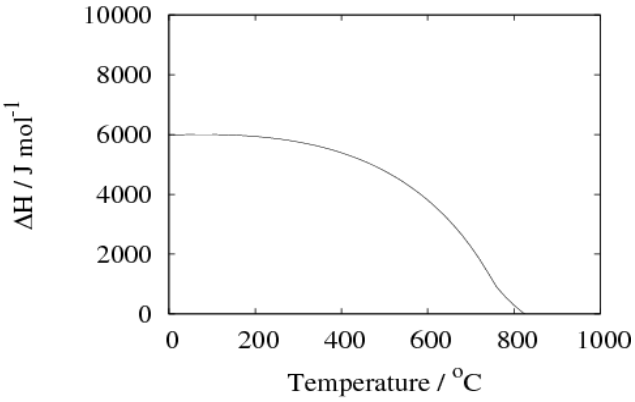

Steel E, M_S =276 °C

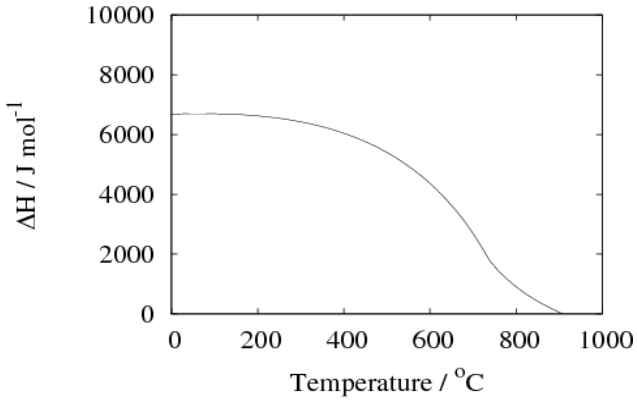

Steel F, M_S =405 °C

Figure 5-15: Calculated enthalpy change for transformation from austenite to ferrite for the different steels.

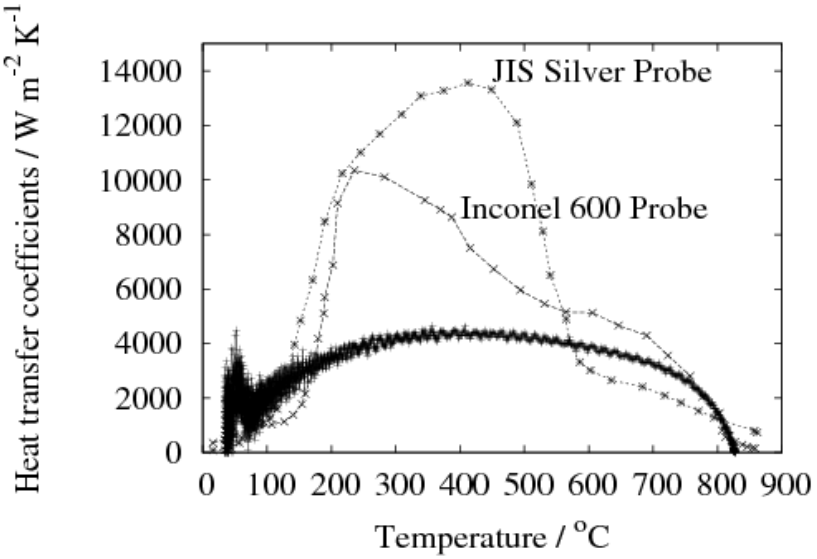

Figure 5-16: Heat transfer coefficient as a function of surface temperature obtained using different probes types quenched in water at room temperature: JIS and Inconel 600 which are previously published work [31], and the probe designed in this work.

5.2 Demonstration of model:

The purpose of the work presented in this section is to demonstrate the success of the modelling techniques previously developed using a control volume method to simulate the quenching process. The modelling techniques are presented here as a case study and validated by comparison against experimental results. It was also believed important to assess the models applicability to other steels with different composition (steel D in table 4-1).

The cooling curves are first estimated together with the hardness profile resulting from quenching a large cylinder, with 52 mm diameter and 20 mm length, of a 0.55 wt % carbon alloy into water at 23 °C. The second section details the experimental work.

5.2.1 Modelling technique:

The procedure for modelling the quenching process is as follows:

1. The thermal conductivity and specific heat for the steel are estimated as a function of temperature using a neural network model and MTDATA thermodynamic calculations.
2. The surface heat transfer coefficient is calculated as a function of the surface temperature from the measured cooling curves using a probe technique.
3. These properties are used along with the dimensions of the sample and the austenitisation and quenchant temperatures to calculate the temperature at each point in the sample as a function of time.
4. Calculation of time-temperature-transformation data if unknown, these are used as inputs to calculate the quench factor.

5. Calculation of the quench factor using equation 2.2 in combination with the TTT-curve and the C-curve.
6. The quench factor can be converted into hardness using equation 2.3 and the measured maximum and minimum hardness value.

5.2.1.1 Physical properties

Thermodynamic calculations were carried out using MTDATA with SGTE database to calculate the specific heat for steel D as a function of temperature in two conditions as discussed in chapter 2.

$$C_p(T) = 458.3 - 0.143\,T \qquad \text{J kg}^{-1}\,\text{K}^{-1} \qquad (5.1)$$

Equation 5.1 was used to represent the specific heat value as a function of temperature ($C_p(T)$) in the calculation of the surface heat transfer coefficient during the quenching process for the probe. This equation covers the temperature range shown in figure 5-17 (1200 °C > T > 0°C).

$$C_p(T) = 481.96 + 0.157\,T - 1.547 \times 10^{-3}\,T^2 + 1.168 \times 10^{-5}\,T^3 - 1.92 \times 10^{-8}\,T^4 + 9.05 \times 10^{-12}\,T^5 \qquad \text{J kg}^{-1}\,\text{K}^{-1} \qquad (5.2)$$

Equation 5.2 was used in the program to represent the specific heat value as a function of temperature ($C_p(T)$) in the calculation of the temperature distribution inside the sample. This equation covers the temperature range shown in figure 5-17 (1200 °C > T > 0°C).

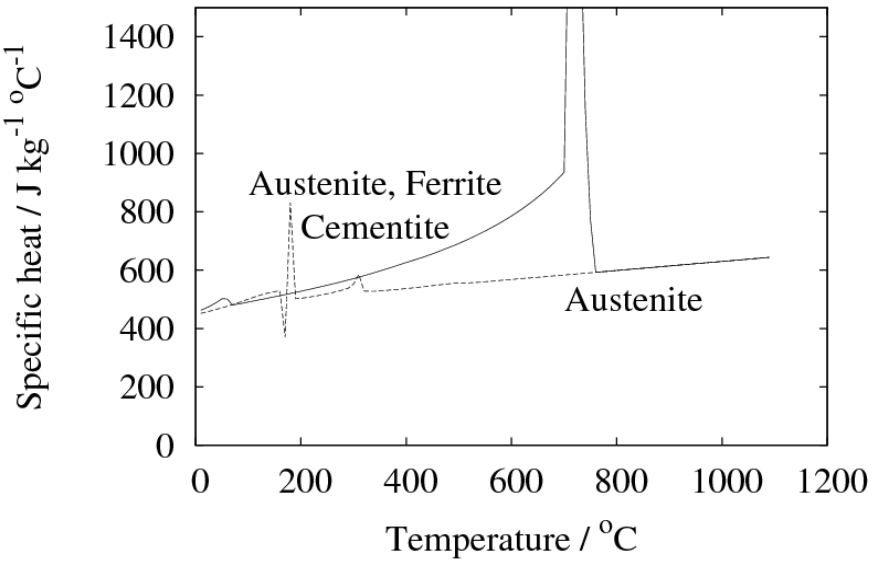

Figure 5-17: Calculated specific heat capacity of steel D as a function of temperature using MTDATA.

The neural network model of thermal conductivity was used to predict the dependence on temperature. This was summarized by fitting an arbitrary polynomial equation for inclusion in the program. Equation 5.3 allows calculation of the temperature distribution inside the sample. This equation covers the temperature range shown in figure 5-18 (1000 °C > T > 0°C).

$$k(T) = 44.98 + 5 \times 10^{-3} T - 7 \times 10^{-5} T^2 + 5 \times 10^{-8} T^3$$

$$\text{W m}^{-1}\text{ K}^{-1} \qquad (5.3)$$

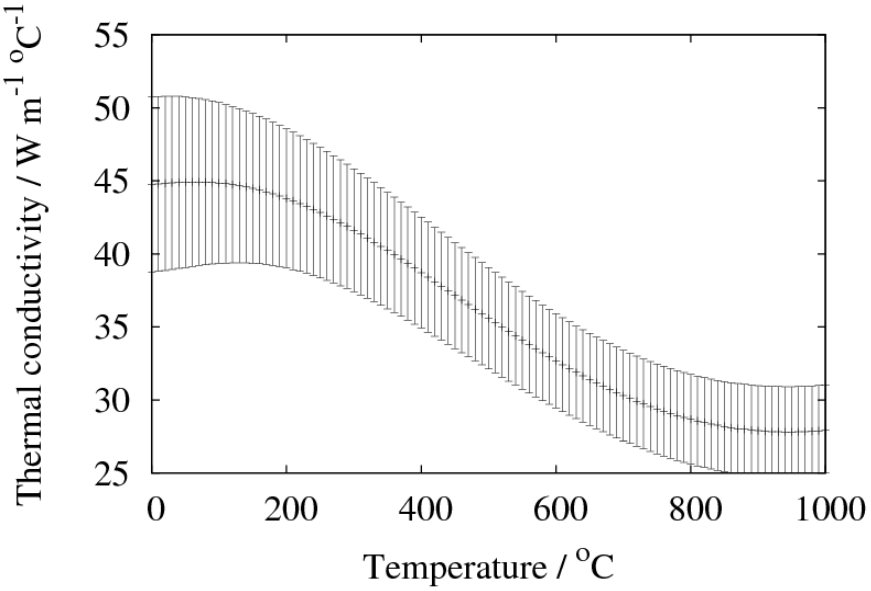

Figure 5-18: Thermal conductivity of steel D as a function of temperature predicted by neural network.

5.2.1.2 Heat transfer coefficient

The temperature history was measured using a 2 mm diameter probe with 1 mm diameter thermocouple inserted inside the probe, the design of which is discussed in chapter 2. The temperature history was used to calculate the cooling rate *(dT/dt)* (figure 5-19) which can be used as an input to the inverse heat conduction model to estimate the heat transfer coefficient at the metal/ quenchant interface.

$$h = \frac{\rho V C_p(T)\frac{dT}{dt}}{A_S(T_S - T_\infty)} \tag{2.10}$$

Figure 5-20 shows the dependency of the estimated heat transfer coefficient on the surface temperature.

Figure 5-21 shows the heat transfer coefficient of Fe- 0.55 C- 0.22 Si- 0.77 Mn- 0.2 Cr- 0.15 Ni wt % steel as a function of time during quenching in water at 23°C.

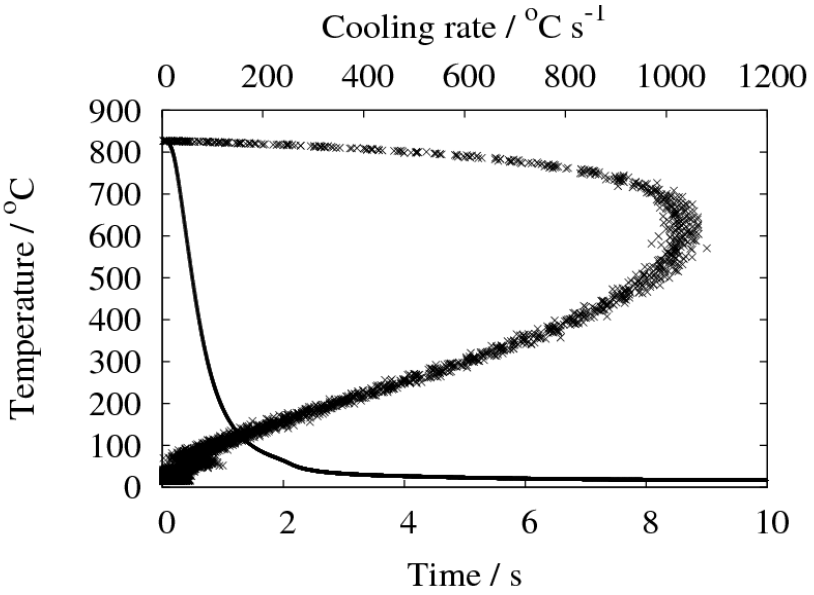

Figure 5-19: Cooling curve and calculated cooling rate curve of steel D probe quenched in 23°C water.

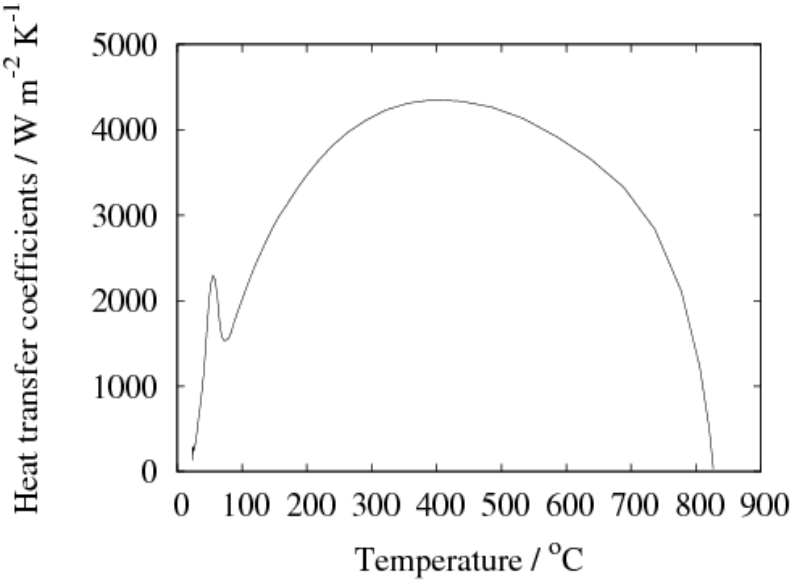

Figure 5-20: Heat transfer coefficient as a function of surface temperature of steel D probe during quenching in water at 23°C.

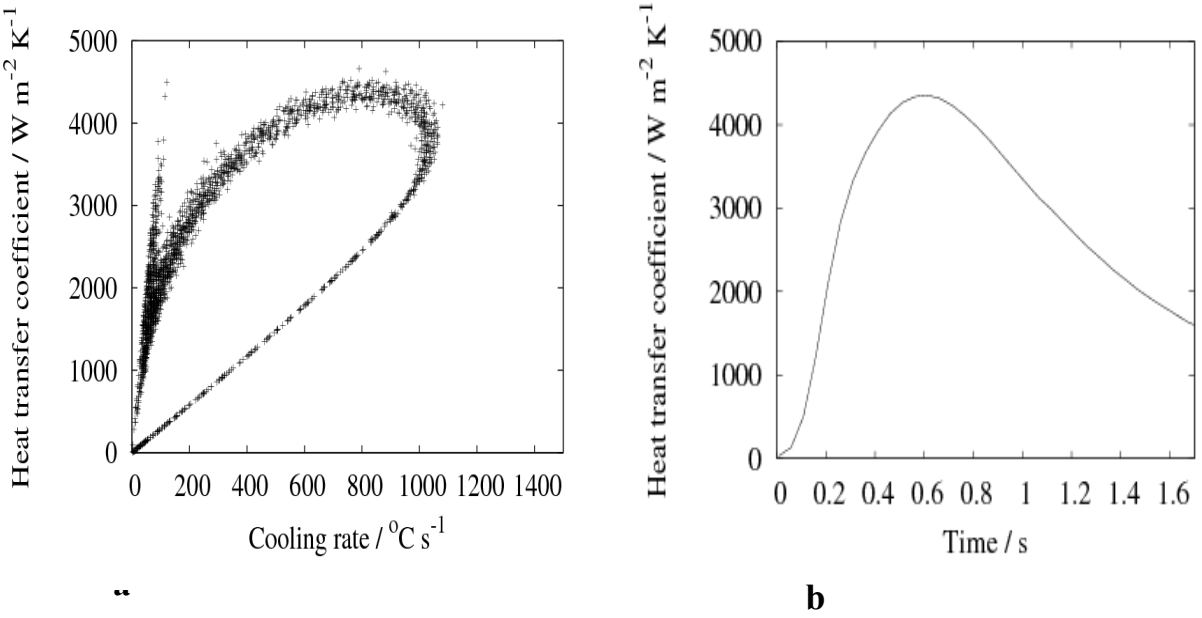

Figure 5-21: Heat transfer coefficient as a function of (a) Cooling rate, (b) time, during quenching in water at 23°C.

5.2.1.3 Modelling results

The cooling curves and the cooling rates were calculated at 3 positions within a sample with 52 mm diameter and 20 mm length (the centre, the midpoint between the centre and the surface, the surface) as shown in figure 5-22 using the control volume program described in chapter 2. Figure 5-23 shows the results of the modelling program.

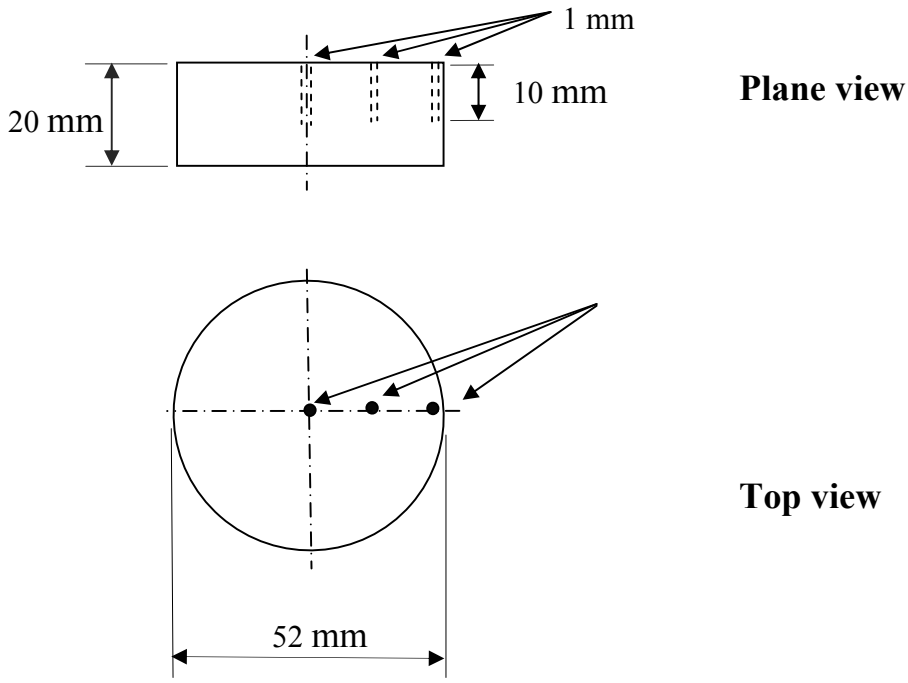

Figure 5-22: steel cylinder sample with the 3 positions in which the cooling curves were calculated.

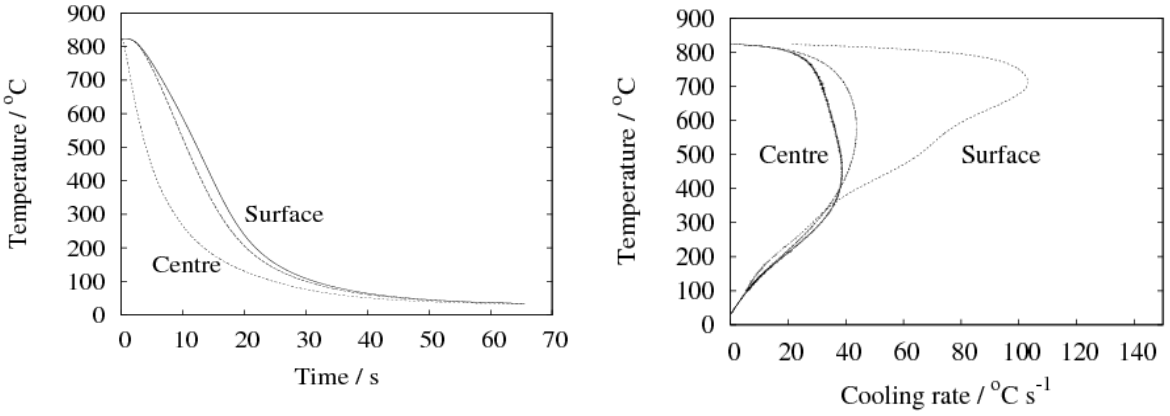

Figure 5-23: Calculated cooling curves and cooling rate curves for different points (from left: centre-mid way to the surface-surface) inside 52 mm diameter and 20 mm length round disc during quenching in water at 23°C.

5.2.1.4 Quench factor and hardness profile

To predict the hardness profile, it is necessary to calculate the quench factor from the estimated cooling curves and the TTT curve as mentioned in chapter 2 (figure 5-24). TTT curve was calculated using the MUCG83 program and equation 2.2 was used to calculate the quench factor.

$$Q = \sum_{T=M_S}^{T=A_{r3}} \frac{\Delta t}{t_c} \qquad (2.2)$$

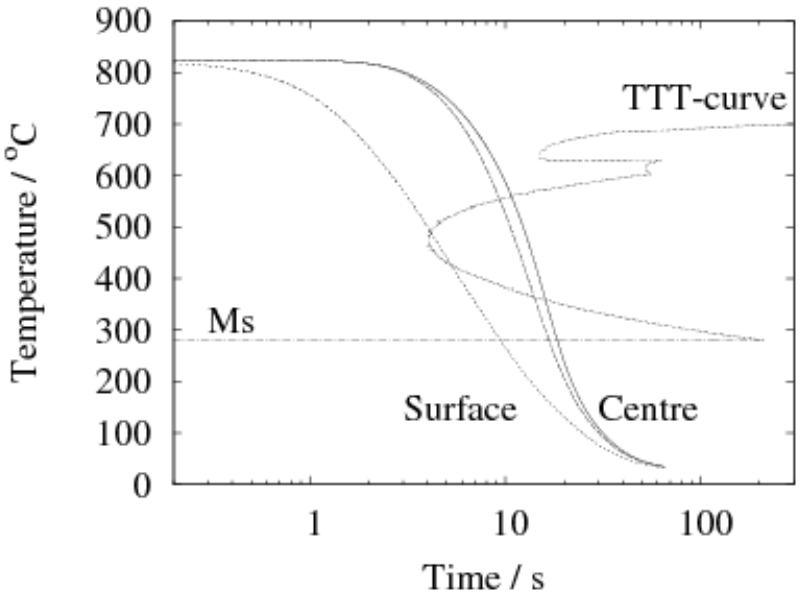

Figure 5-24: Calculated TTT diagram of steel D with cooling curves in different points inside 52 mm diameter round disc and 20mm length during quenching in water at 23°C. Heat transfer equations were used to calculate temperature distribution inside the sample.

Then the quench factor value was converted into hardness using equation 2.3 with the measured maximum and minimum Vickers hardness values for this steel (martensite and ferrite + pearlite structures) (figure 5-25).

$$Hp = H_{min} + (H_{max} - H_{min})\exp(K_1 Q) \qquad (2.3)$$

Figure 5-26 shows the change in the quench factor with the distance from the centre to the surface while figure 5-27 shows the corresponding difference in the calculated hardness.

Measurement of maximum and minimum hardness

To measure the maximum hardness a martensitic microstructure was obtained by austenizing a sample 4 mm diameter and 4 mm length, at 950 °C for 30 min followed by quenching in water. The specimen was sealed during austenitisation in an evacuated quartz tube back filled with pure argon to protect the sample against oxidation. The minimum hardness was obtained by similarly austenizing the sample at 950 °C for 30 min but with an isothermal dwell at 650 °C for 2 h followed by slow cooling inside the furnace to ensure the formation of pearlite. The maximum hardness was 731 ± 0 HV50 and the minimum hardness was 185 ± 0.7 HV50.

Martensitic microstructure

HV50kg = 731

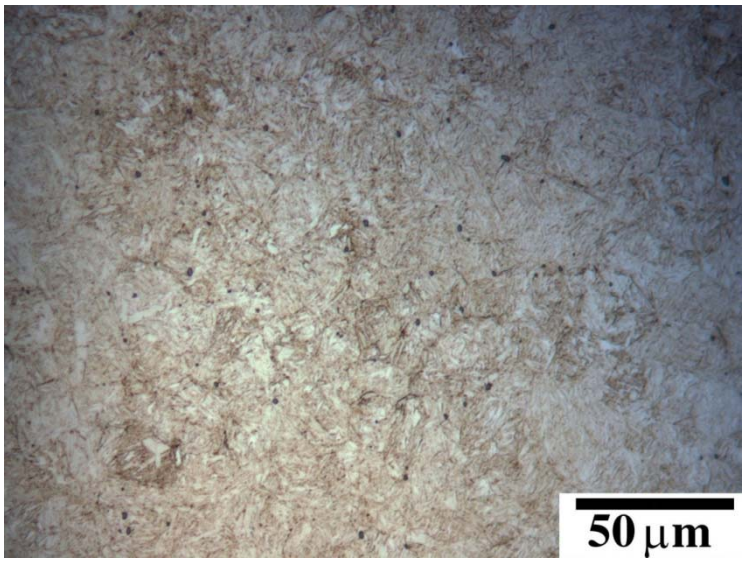

Ferrite + pearlite microstructure

HV50kg = 185 ± 0.7

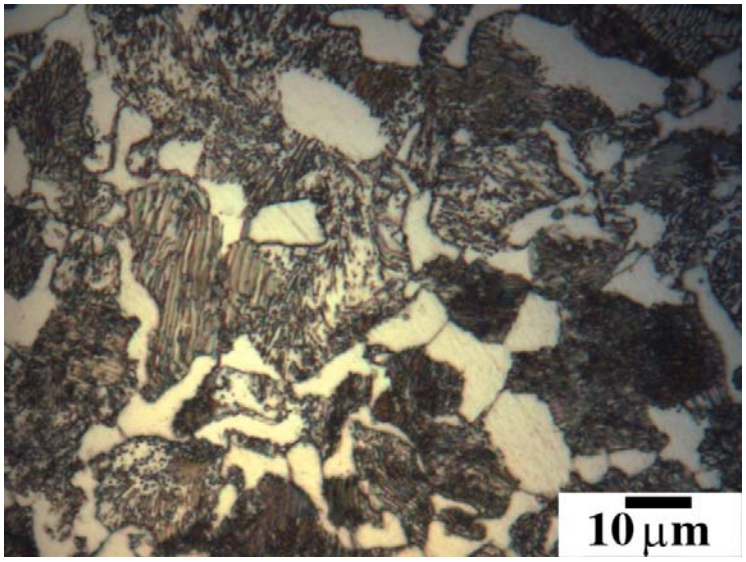

Figure 5-25: Martensite and ferrite-pearlite structures produced to measure the maximum and the minimum hardness.

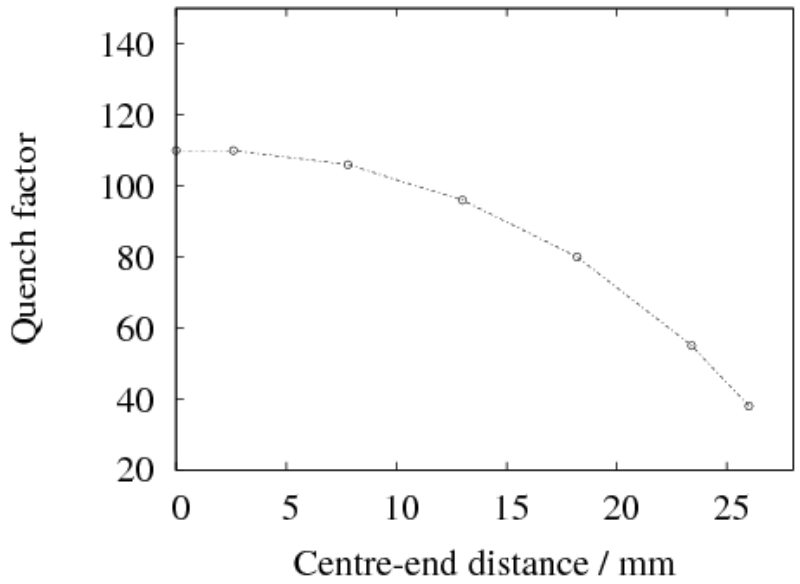

Figure 5-26: Calculated quench factor as a function of distance from the centre to the surface.

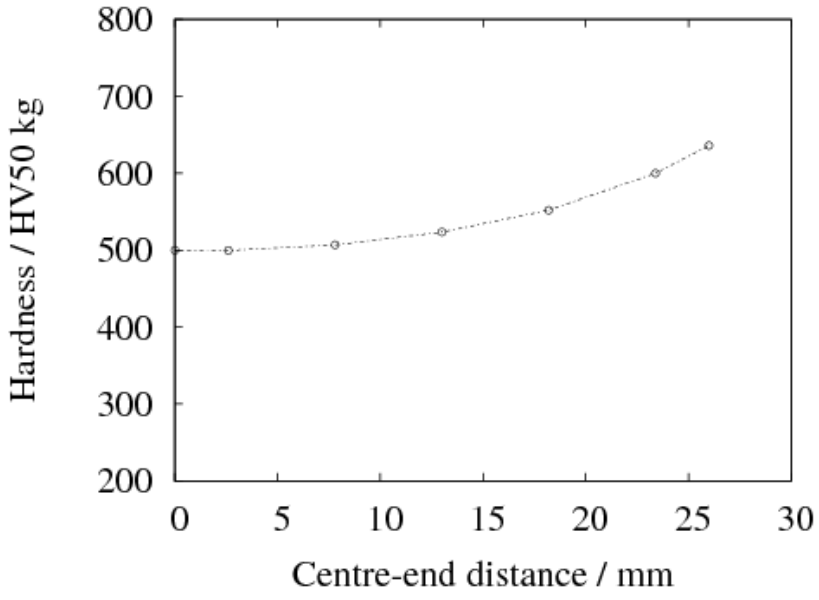

Figure 5-27: Calculated hardness as a function of distance from the centre to the surface.

5.2.2 Experimental investigation

A cylindrical sample was used with three K-type thermocouples inserted as illustrated in figure 5- 5 (geometric centre-midpoint between the centre and the surface –1 mm to the surface). The sample dimensions are the same as the dimensions in the modelling program (52 mm diameter and 20 mm length). The thermocouples were connected to the data logger to record the cooling curves during the quenching process. The cooling curves were used to predict the hardness profile in the sample using the same procedure as in section 5.2.1. Figure 5-28 shows the curves and the corresponding cooling rate as a function of temperature at the three locations. While figure 5-29 shows the TTT diagram of steel D with superposed cooling curves at different positions inside the sample; And figure 5-30 shows the experimentally measured hardness as a function of distance from the centre to the surface of the sample. Figure 5-31 shows the microstructure of the sample as a function of distance from the centre to the surface for the same sample.

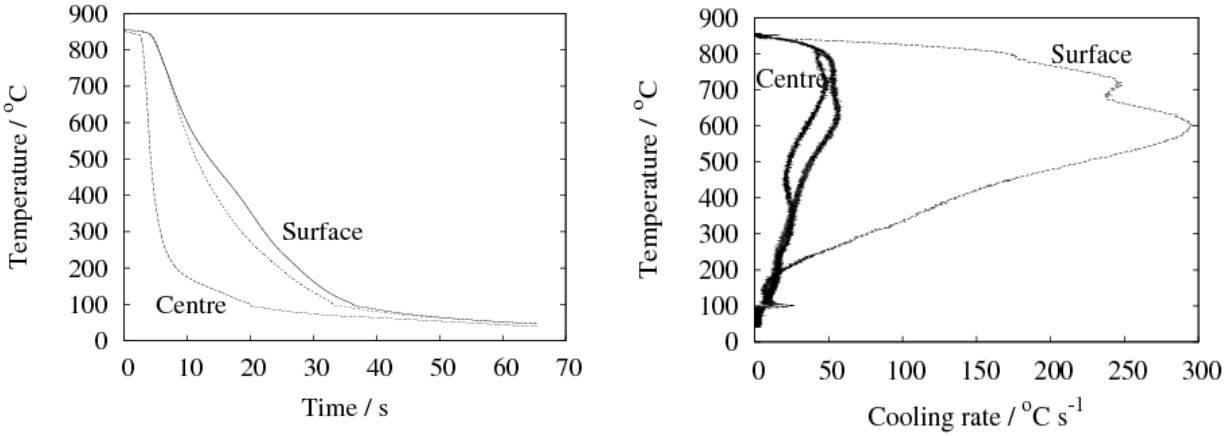

Figure 5-28: Experimental cooling curves and cooling rate curves for different points (from left: centre-mid way to the surface-surface).

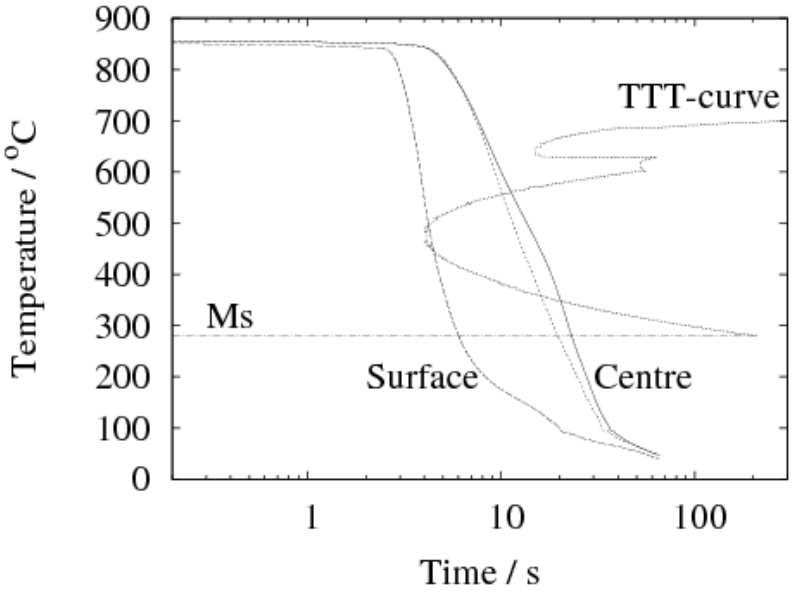

Figure 5-29: TTT diagram of steel D with superposed cooling curves at different positions inside the sample.

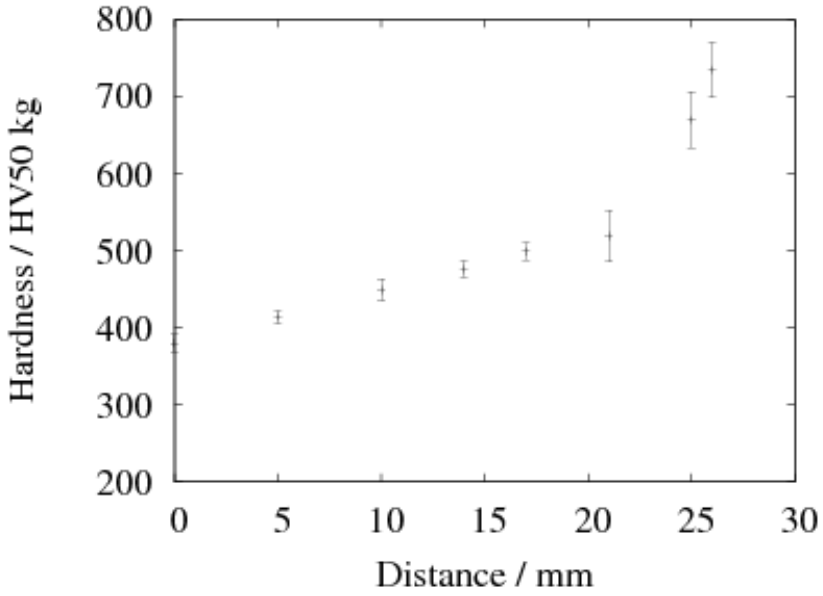

Figure 5-30: Measured hardness as a function of distance from the centre to the surface.

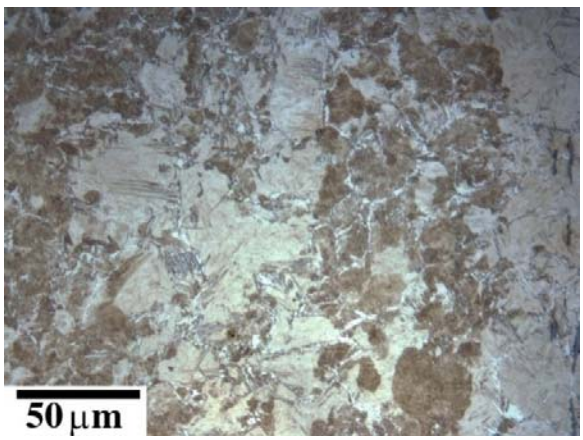

0 mm

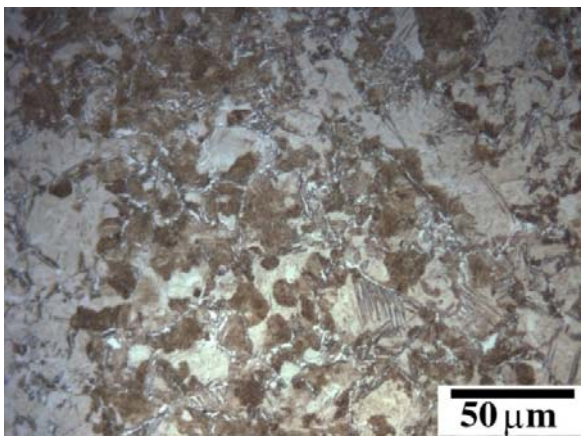

4 mm

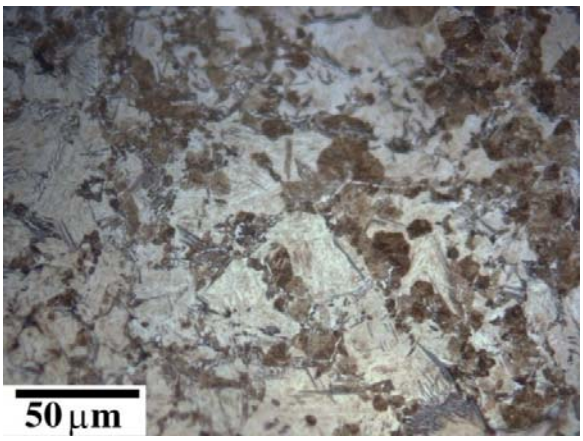

8 mm

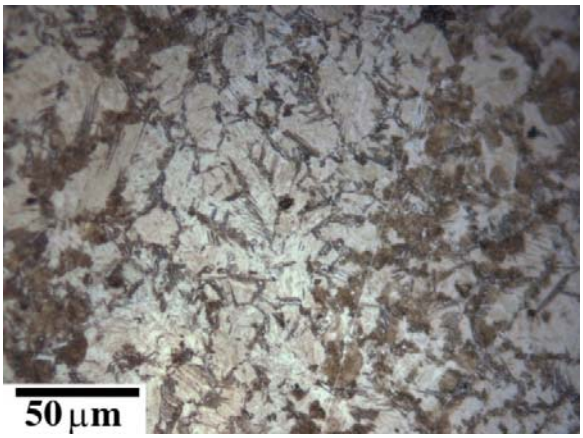

12 mm

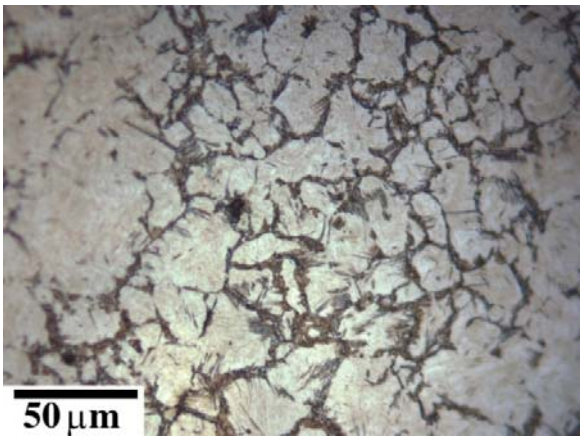

18 mm

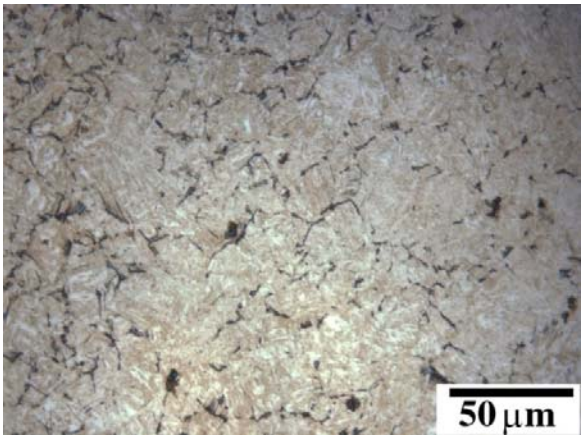

24 mm

Figure 5-31: Microstructures as a function of distance from the centre to the surface.

5.2.3 Comparison between the modelling program results and the experimental results

Figure 5-32 shows a comparison between the calculated cooling curves by using the heat transfer coefficient in figure 5-20 and the measured cooling curves with the TTT diagram of the steel. The comparison shows good agreement between the two curves.

Figure 5-33 shows the calculated hardness using quench factor analysis and experimental measured hardness. Reasonable agreement was found between both of them especially at the surface, and then the difference between them will increase with the decrease in the hardness value. In fact, the error in the calculated hardness using quench factor analysis include the difference of the size between the steel specimen and the probe and all the possible error during the estimation of thermal conductivity and the specific heat for the steel using neural network model and MTDATA thermodynamic calculation; In addition, the heat transfer coefficient applied in the modelling program includes the coupled effect of temperature changing within the probe and the latent heat for the martensite transformation because the probe with the 2 mm diameter structure was fully martensitic after the quenching test, which makes the prediction more accurate when the structure is mostly martensitic.

These results are in agreement with those of Totten *et al*. [31], who also found that the predicted hardness using quench factor analysis and the experimental measured hardness for AISI 1045 steel agree closely until the martensite content falls below 50% at a hardness of approximately 32 HRC. The inability of quench factor analysis to predict hardness successfully over the whole range of hardness arises because it is very difficult to model the

extremely rapid transitions from softer ferritic-pearlitic structures to martensite.

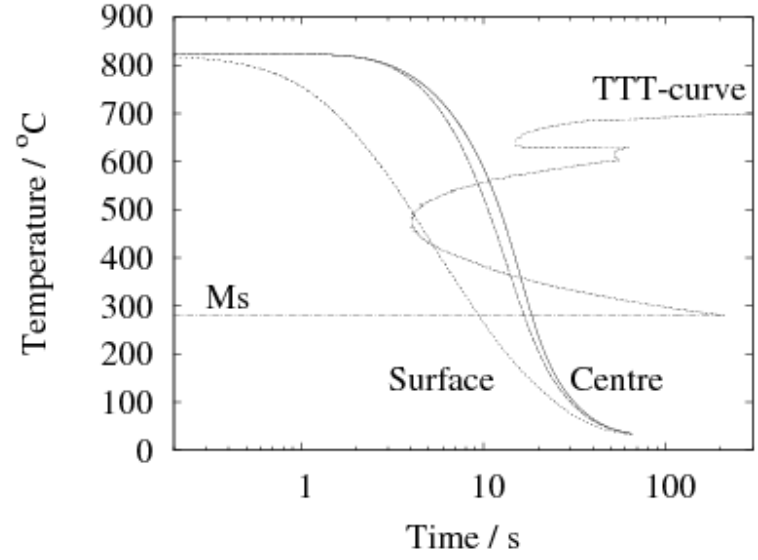

(a)

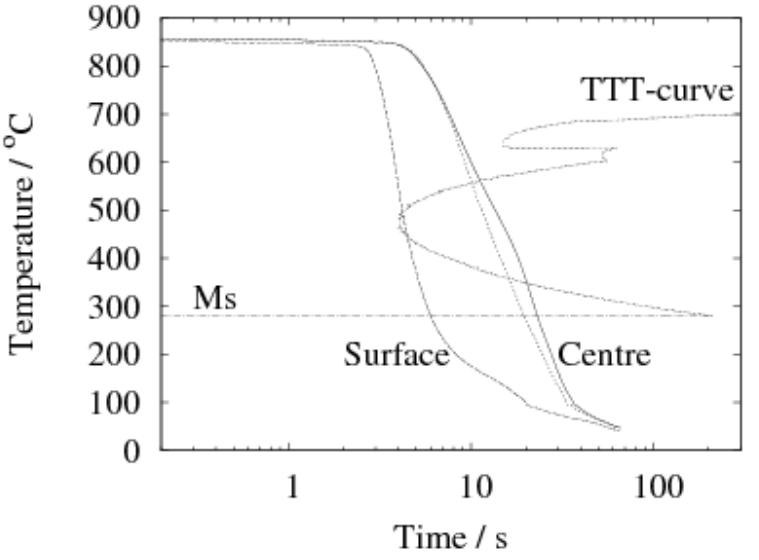

(b)

Figure 5-32: Comparison between the calculated (a) and the measured (b) cooling curves with the TTT diagram of Fe-0.55 C-0.22 Si-0.77Mn-0.2 Cr-0.15 Ni wt % steel.

	Centre		Middle		Surface	
	QF	**Hardness**	**QF**	**Hardness**	**QF**	**Hardness**
Prediction from measured cooling curves.	110	500	96	523	38	636
Prediction from calculated cooling curves.	126	476	105	507	38	638
Measured hardness	380 ± 12.14		476 ± 10.72		670 ± 36.24	

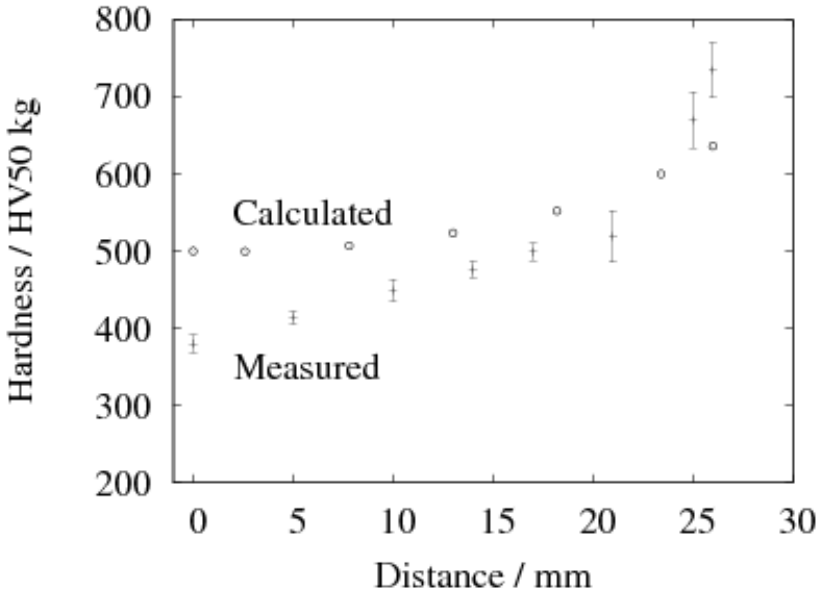

Figure 5-33: Calculated and measured hardness as a function of distance from the centre to the surface.

5.2.4 Comparison between the measured hardness and the predicted hardness using different probes

In order to compare between the probe designed in the present work and the other two standard probes shown in the figures 1-2 and 1-3 (JIS probe and Inconel 600 probe), the heat transfer coefficient estimated using JIS and Inconel 600 probes (figure 5-16) were applied as a boundary condition to the modelling program to predict the hardness distribution within the sample in figure 5-22. Figure 5-34 shows the results for the measured and the estimated hardness using three different probs. This figure shows that the hardness prediction using Inconel 600 and JIS probes are close to each other while the closest prediction to the measured hardness was using the probe designed in this work. The values for the heat transfer coefficient for the JIS and Inconel 600 probes were taken from reference [1] using a plot digitizer program.

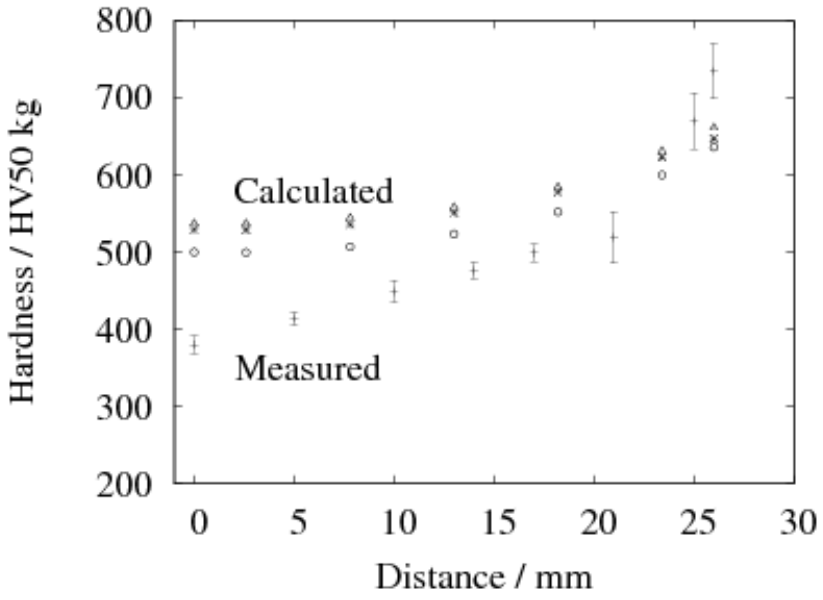

Figure 5-34: Measured and calculated hardness as a function of distance from the centre to the surface using three different probes: JIS (×), Inconel 600 (△), and the designed probe (○).

5.3 Effect of quenchant temperature on heat transfer of steels in water, brine and oil

The effect of quenchant temperature on the cooling curve, cooling rate and heat transfer coefficient is described in this section. The common quenchants studied include water, oil and brine.

5.3.1 Cooling curves and cooling rates results

5.3.1.1 Water quenching

Figures 5-1 and 5-2 show the cooling curve, cooling rate and heat transfer coefficient for steel "A" probe. Figure 5-35 shows the microstructure of the probe after quenching in water at 23°C; it is banded and is not fully martensitic, consistent with the hardness of 259 HV. The hardness of a fully martensite structure in this steel is 351±8 HV50, obtained by quenching an 8 mm × 12 mm cylinder directly from 850 °C into water and measuring the hardness of the surface; the sample was in a quartz tube during transfer from the furnace to the quenchant with the tube broken immediately it reached the quenching tank.

Figures 5-36 to 5-43 show the recorded cooling curves, derived cooling rate curves and the heat transfer coefficients as a function of the surface temperature during quenching in water at different temperatures (42, 60, 75 and 100°C). The variation that occurs for quenching into water at 0°C can be seen in Figures 5-44 and 5-45. The experiment was repeated three times with the same conditions, but different behaviour was noticed on each occasion. This indicates there is some uncontrolled variable which is affecting the quenching at 0 °C, which uses a mixture of ice and water.

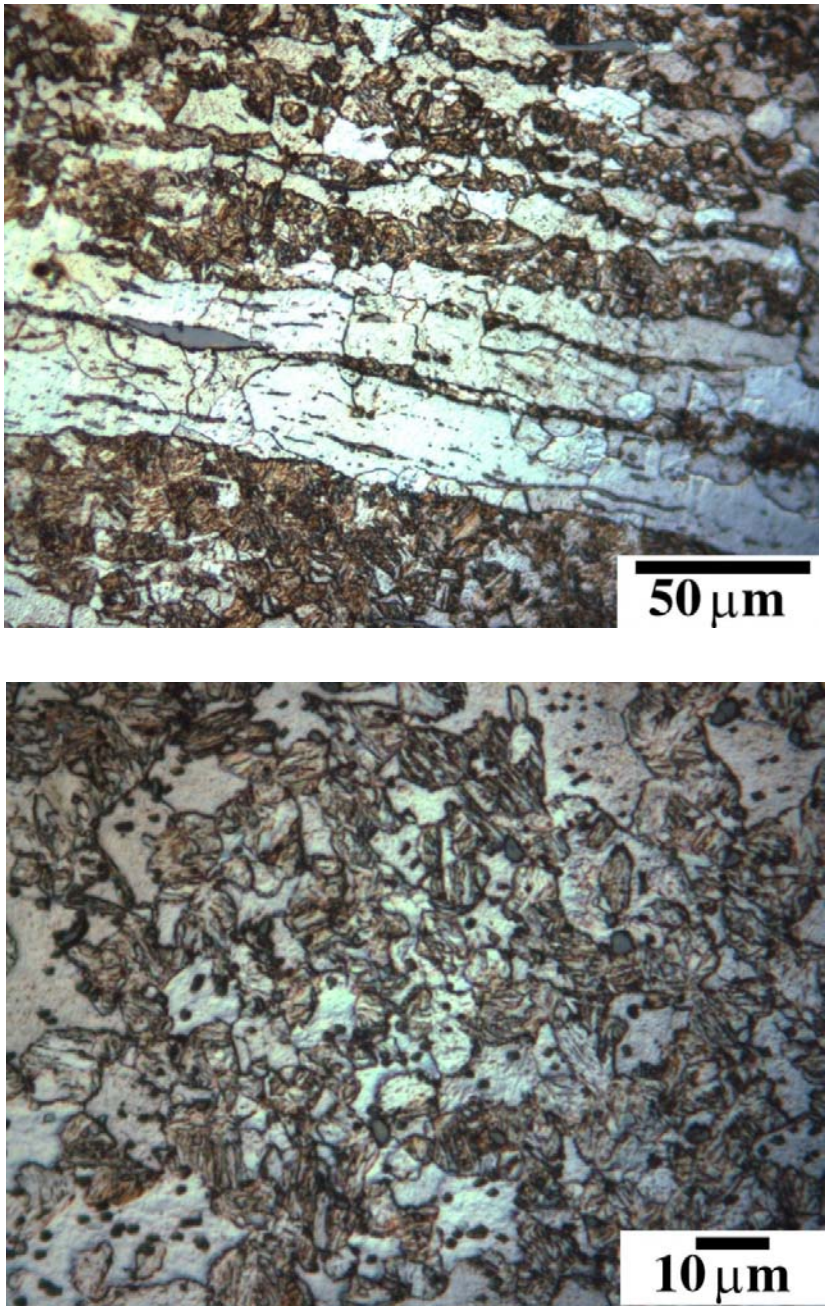

Figure 5-35: Microstructure of the probe after quenching in water with 23 °C. (a) Longitudinal section. (b) Transverse section.

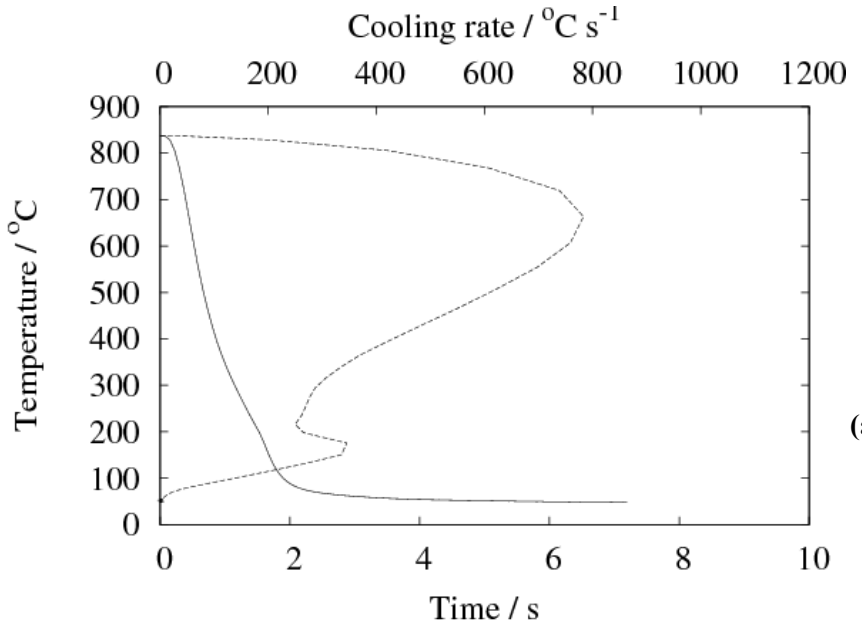

Figure 5-36: Cooling curve (solid) and derived cooling rate curve (dashed) for steel A quenched in 42°C water.

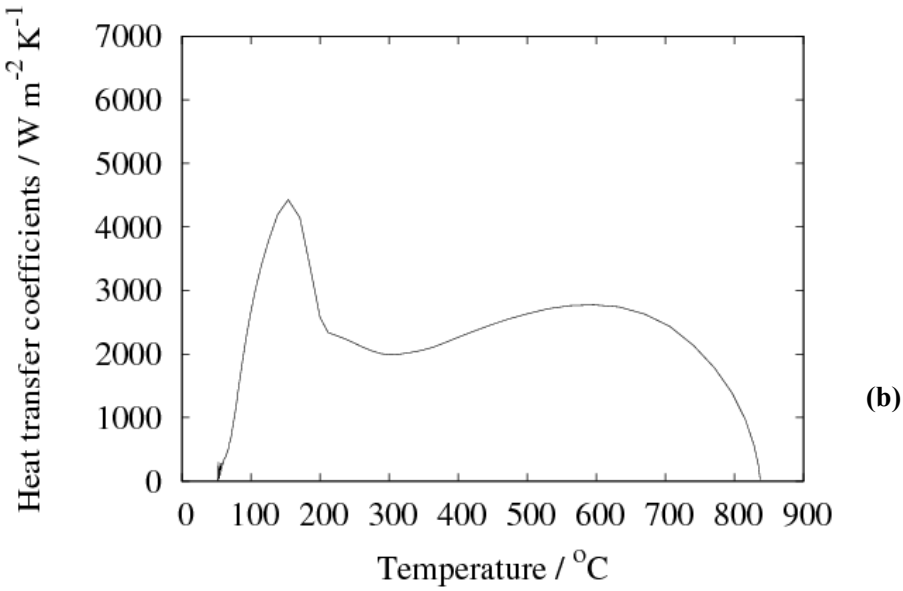

Figure 5-37: Heat transfer coefficient as a function of surface temperature during quenching in water at 42°C.

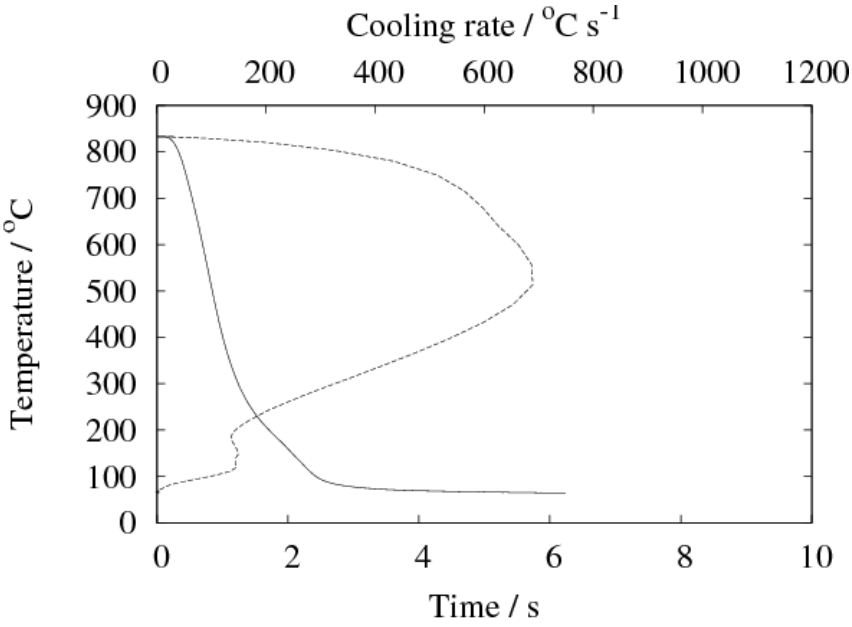

Figure 5-38: Cooling curve (solid) and derived cooling rate curve (dashed) for steel A quenched in 60°C water.

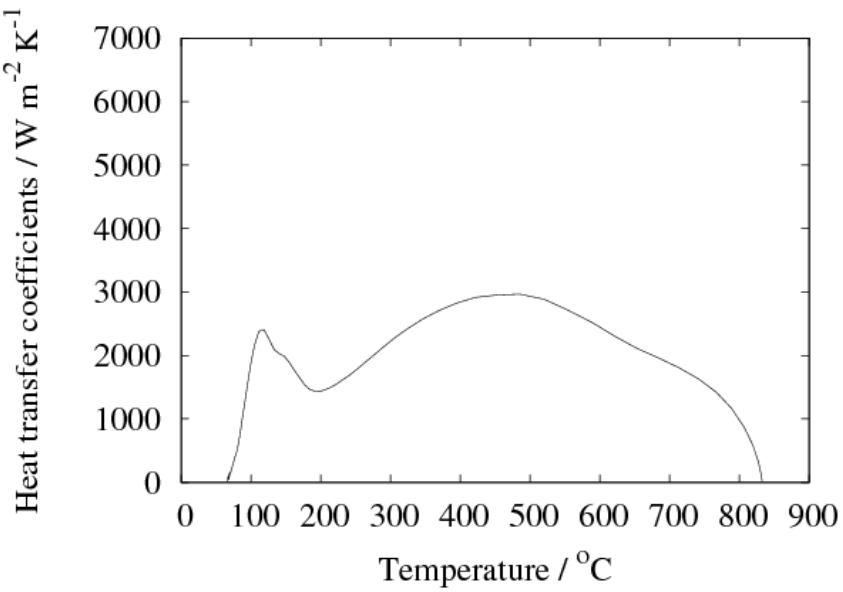

Figure 5-39: Heat transfer coefficient as a function of surface temperature during quenching in water at 60°C.

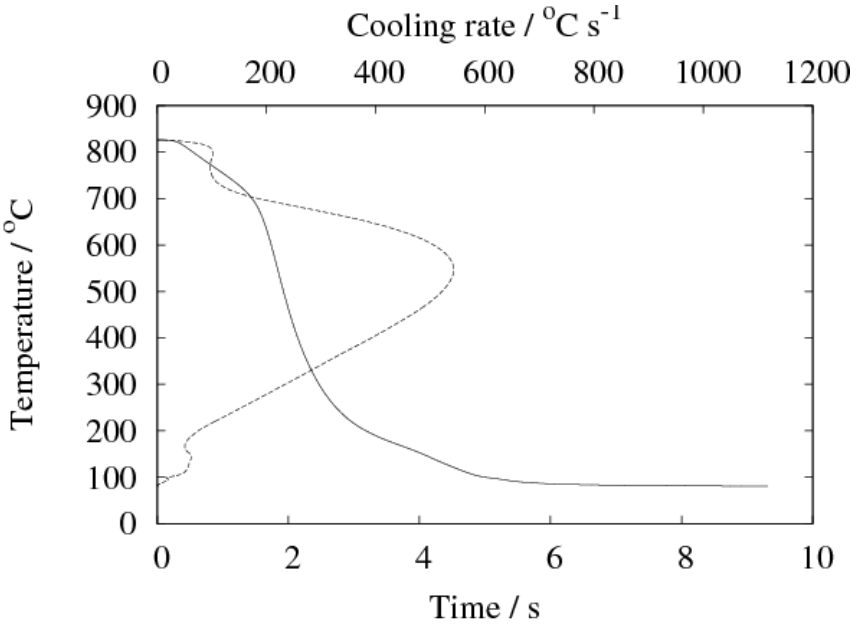

Figure 5-40: Cooling curve (solid) and derived cooling rate curve (dashed) for steel A quenched in 75°C water.

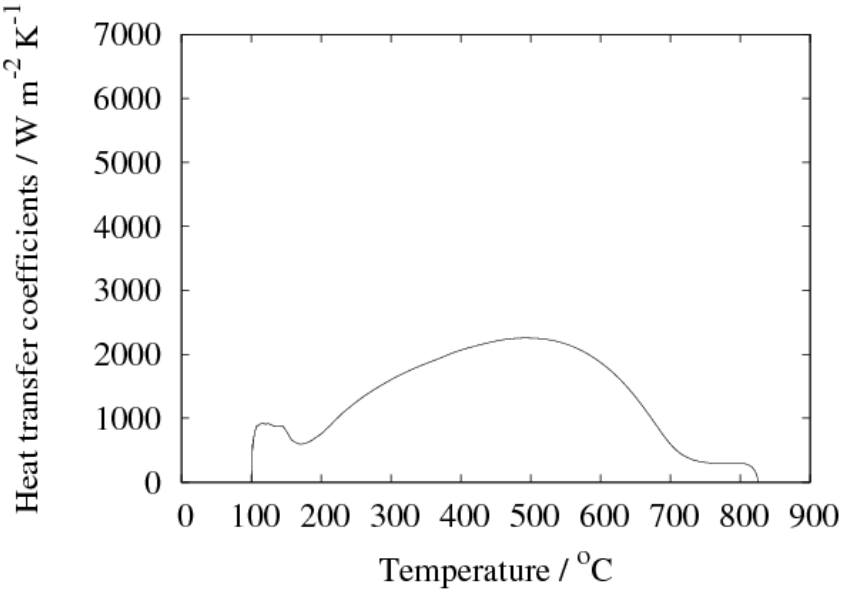

Figure 5-41: Heat transfer coefficient as a function of surface temperature during quenching in water at 75°C.

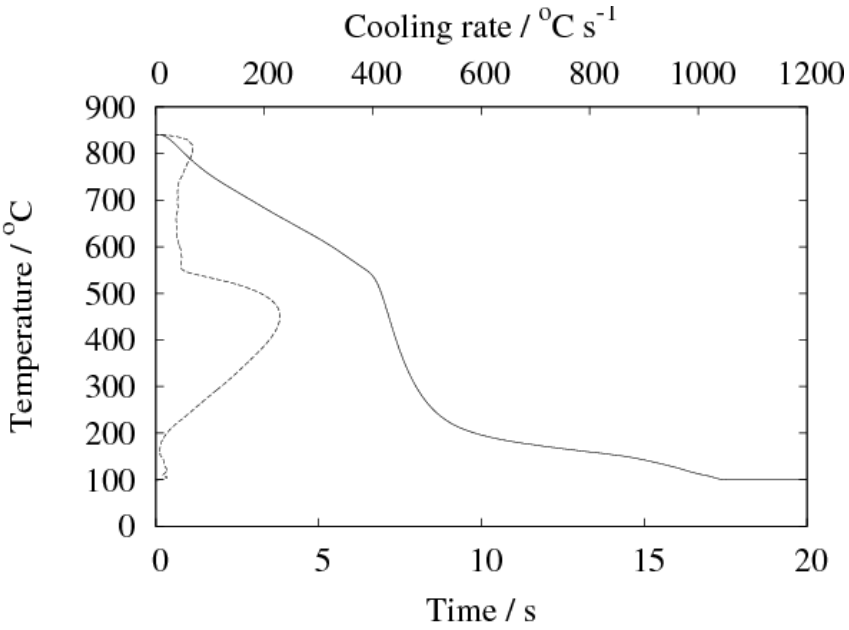

Figure 5-42: Cooling curve (solid) and derived cooling rate curve (dashed) for steel A quenched in 100°C water.

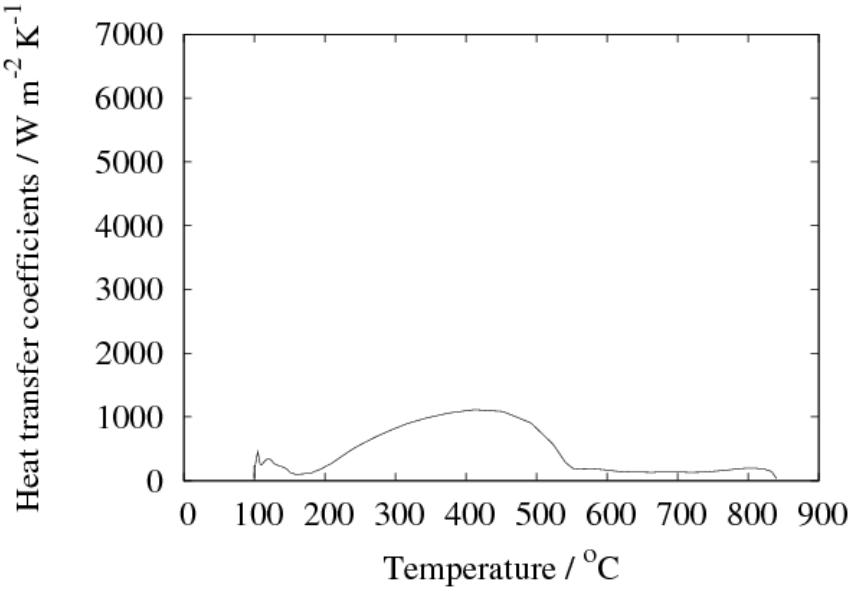

Figure 5-43: Heat transfer coefficient as a function of surface temperature during quenching in water at 100°C.

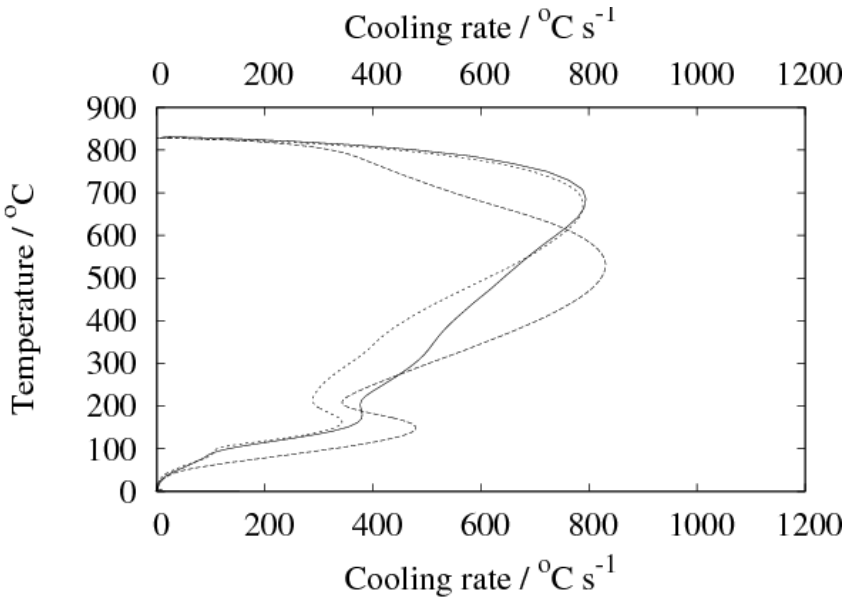

Figure 5-44: Derived cooling rate curve from three different experiments for steel A quenched in 0°C water.

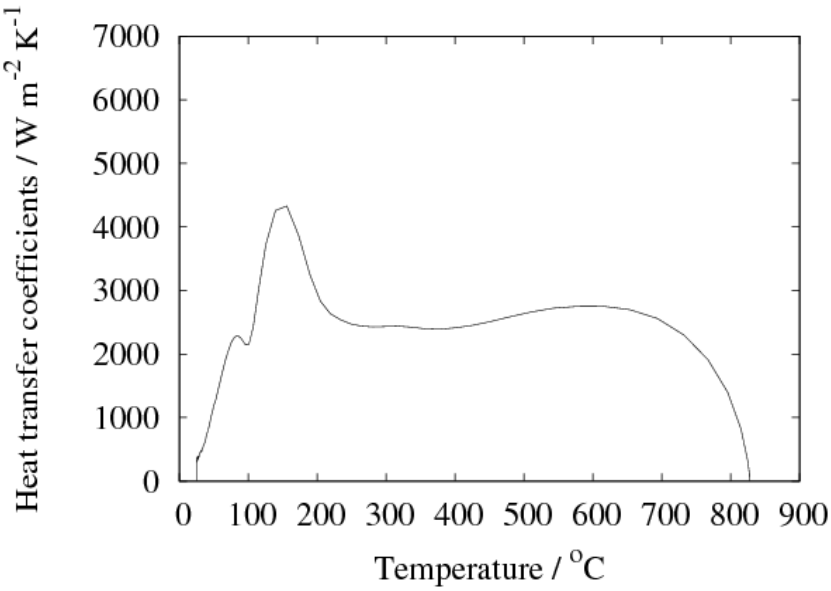

Figure 5-45: Heat transfer coefficient as a function of surface temperature during quenching in water at 0°C.

Figure 5-46 shows the cooling and the calculated cooling rate curves for a 2 mm probe quenched in water at a variety of temperatures. The quenching ability systematically increases as the water temperature is reduced. The cooling rate rapidly increases and its maximum shifts towards higher temperatures (pearlite transformation region) when the quenchant temperature is reduced from 100 to 23°C. The effect of the appearance of the vapour blanket is evident; at temperatures close to the boiling point of the water, an increase in the temperature of the quenching water reduces the energy required to evaporate the water and makes the vapour blanket stage range (stage C) to widen to about 540 °C during quenching in water at 100 °C comparing with 700 °C in water at 75°C. This would make it difficult to harden large diameter components. It is therefore not normal to control the cooling rates by adjusting quenchant temperature. Figure 5- 46 also shows that the main disadvantage of using plain water in quenching the steels is that the rapid cooling rate persists to lower temperatures, this will lead to large temperature and stress gradients and make distortion and cracking more likely to occur.

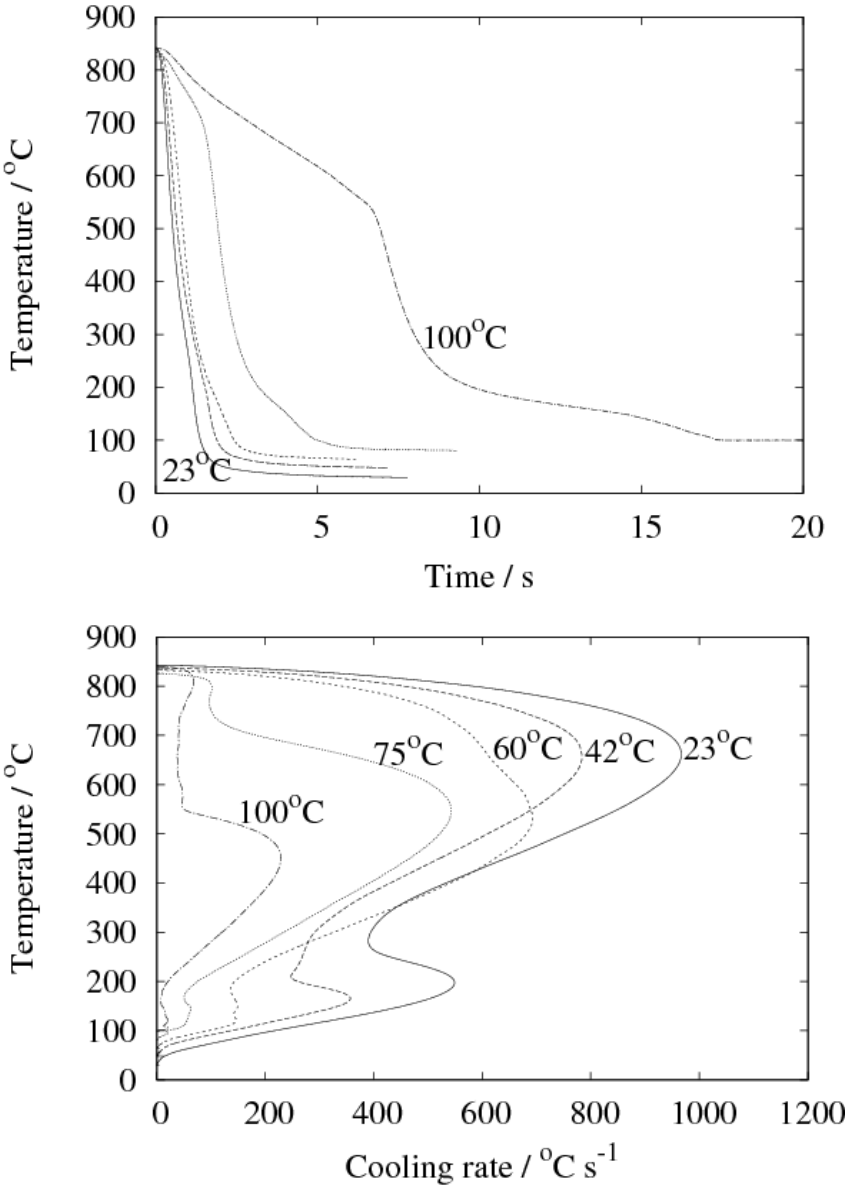

Figure 5-46: Cooling curves and cooling rates for steel A probe at different quenchant (water) temperatures.

Figure 5-47 shows the heat transfer coefficient for quenching into water at temperature in the range 23 to 100 °C. The coefficient is sensitive to the temperature difference between the quenchant and the surface of the material. Depending on the type of quenchant, different factors can dominate heat transfer mechanism; conduction, convection and radiation. Usually the heat transfer by conduction is small in comparison to that by convection and radiation mechanisms.

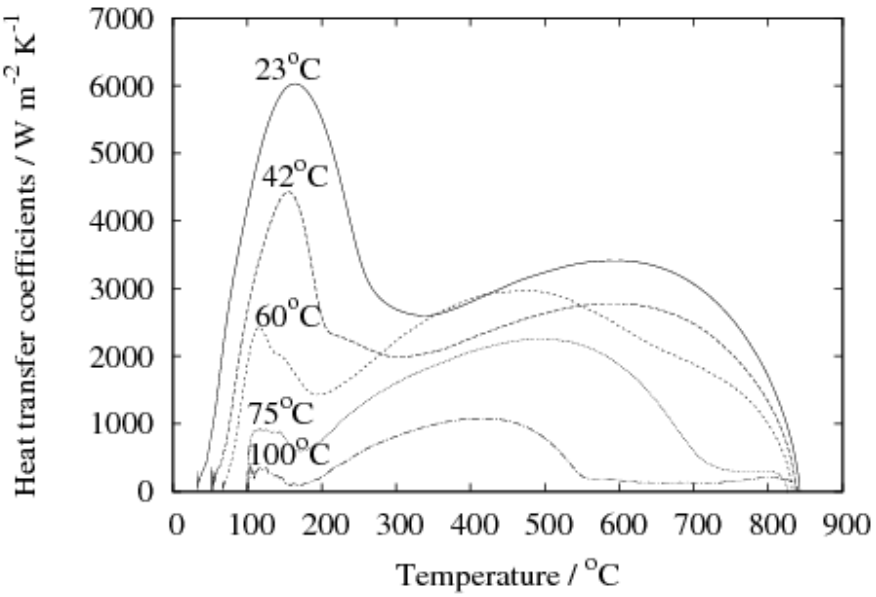

Figure 5-47: Heat transfer coefficient as a function of surface temperature during quenching at different water temperatures.

5.3.1.2 Oil quenching

Micron GP 460 mineral oil was used to study the effect of oil temperature on the heat transfer properties of steel A**.** The oil has 245 °C flash point and 462 mm^2 s^{-1} kinematic viscosity at 40°C.

Figure 5-48 shows the cooling curve and the cooling rate curve for steel A probe quenched in oil at 20°C. The main advantage with oil is the ability to produce relatively high cooling rates during the initial stage of the quenching process, thus avoiding the formation of soft pearlite followed by a lower cooling rate as the steel approaches the martensitic transformation temperature, M_s (461 °C in this steel) which helps to avoid cracking and distortion.

Figure 5-49 shows the calculated heat transfer coefficient as a function of the surface temperature. The maximum heat transfer coefficient during the quenching process is 700 W $m^{-2}K^{-1}$ at 750°C. Figure 5-50 to 5-53 show the recorded cooling and cooling rate curves, and the heat transfer coefficients as a function of surface temperature during quenching in oil at different temperatures (85 and 150°C).

Figures 5-54 to 5-56 show the effect of oil temperature on its heat transfer properties. The quenching severity is hardly dependant on the oil temperature; this is one of the characteristic features of quenching oils. Figure 5-55 also shows that the cooling rate is only slightly affected by increasing the oil temperature in the range below 100°C while the difference becomes greater at 150°C because of the high reduction in viscosity. In fact, the quench severity of a particular oil is directly related to its ability to wet the part surface, which increases with decreasing viscosity. A decrease in viscosity should also increase convection rates and lead to greater ability to quench.

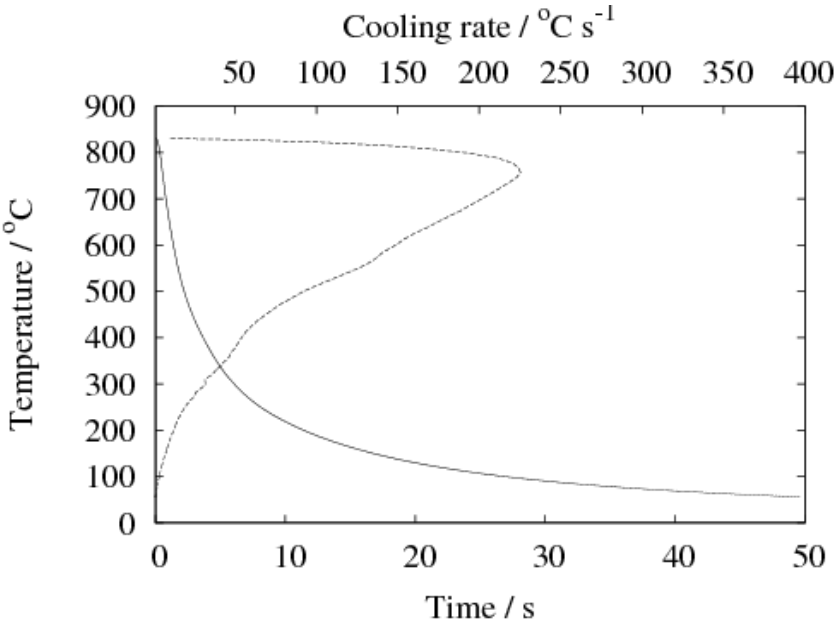

Figure 5-48: Cooling curve (solid) and calculated cooling rate curve (dashed) for steel A quenched in 20°C oil.

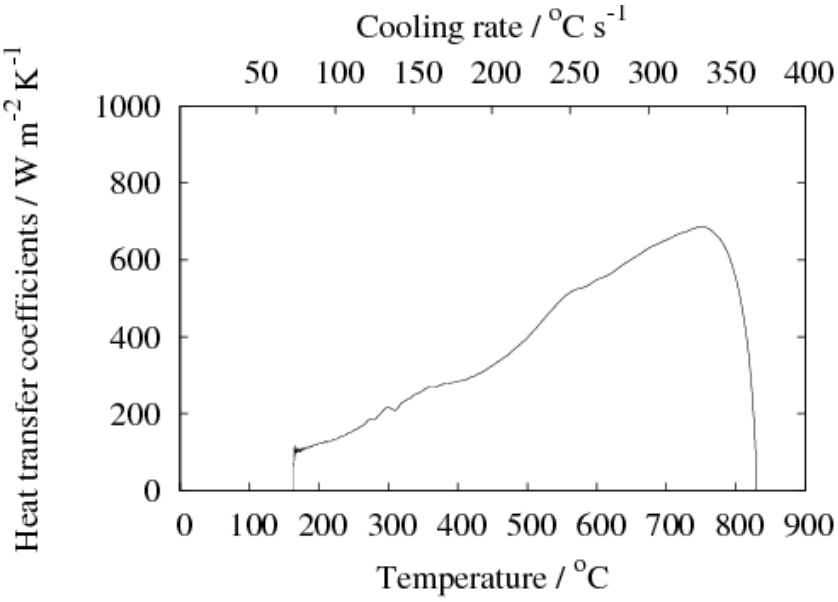

Figure 5-49: Heat transfer coefficient as a function of surface temperature during quenching in oil at 20°C.

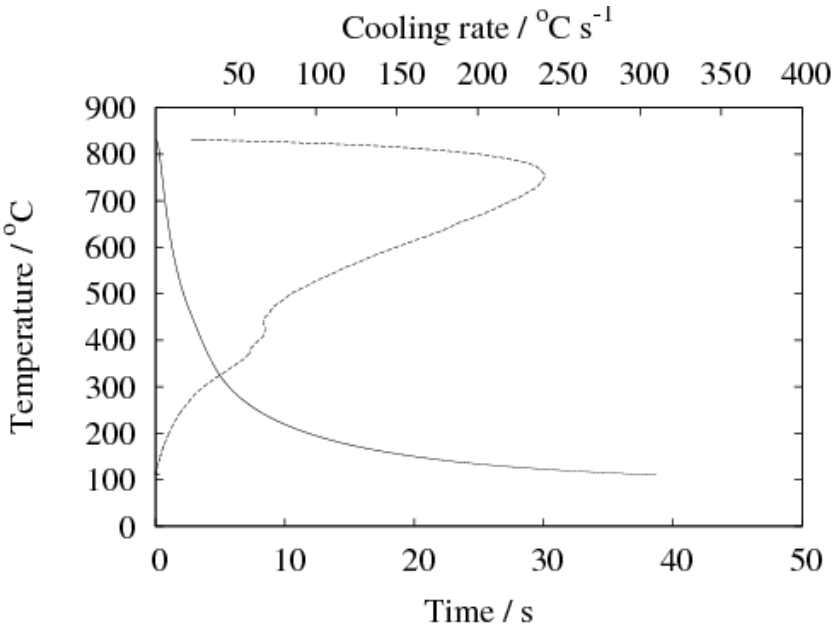

Figure 5-50: Cooling curve (solid) and calculated cooling rate curve (dashed) for steel A quenched in 85°C oil.

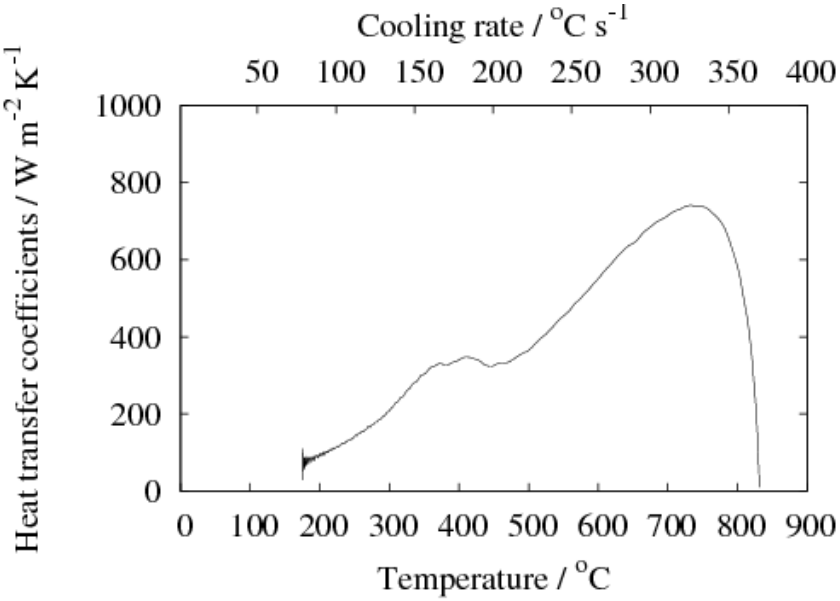

Figure 5-51: Heat transfer coefficient as a function of surface temperature during quenching in oil at 85°C.

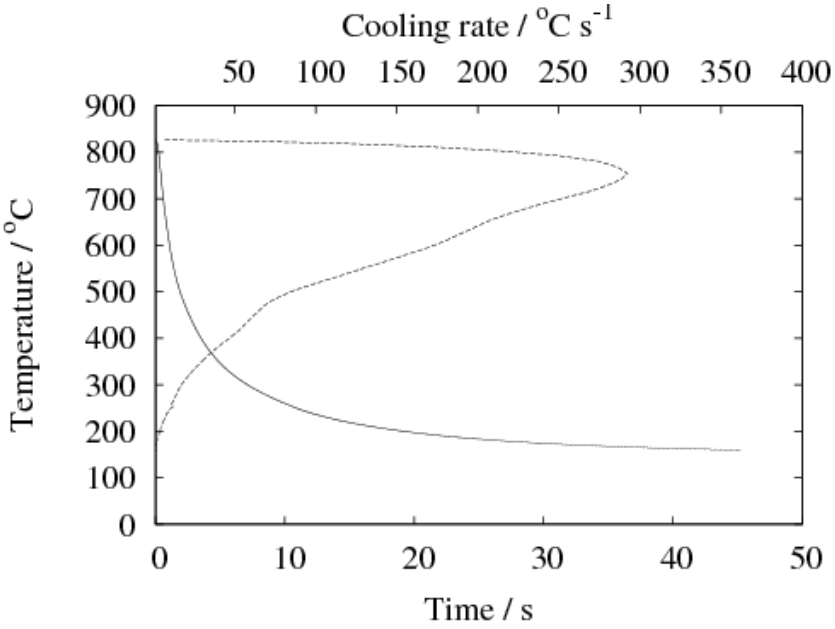

Figure 5-52: Cooling curve (solid) and calculated cooling rate curve (dashed) for steel A quenched in 150°C oil.

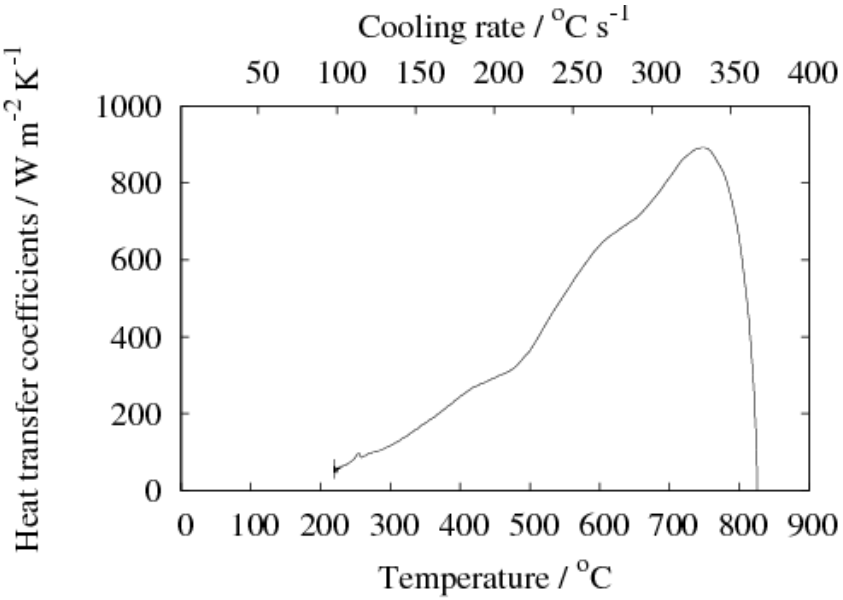

Figure 5-53: Heat transfer coefficient as a function of surface temperature during quenching in oil at 150°C.

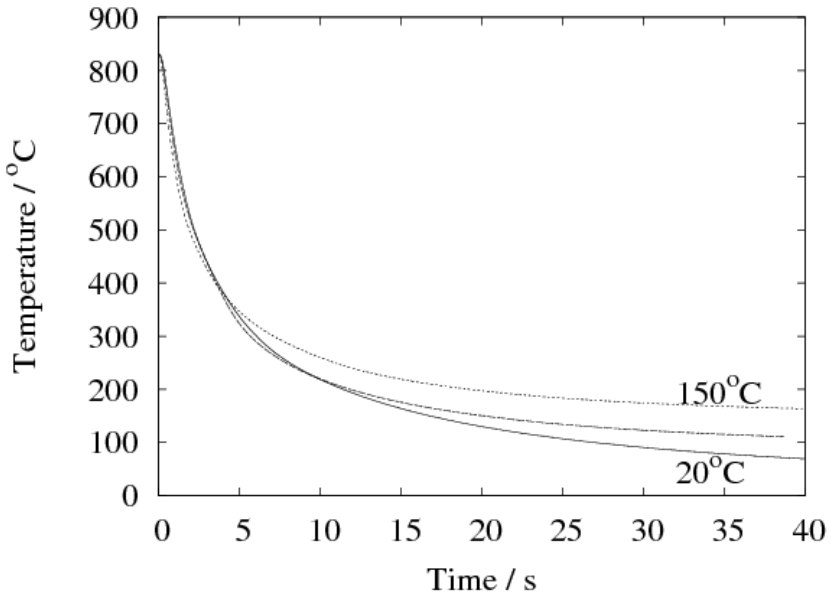

Figure 5-54: Cooling curves for steel A probes at different quenchant (oil) temperatures.

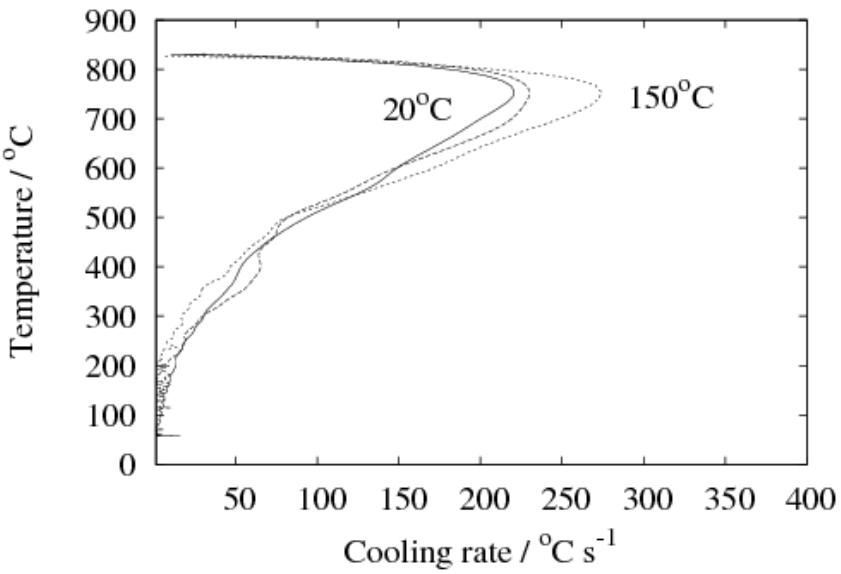

Figure 5-55: Effect of quenchant temperature (oil) on cooling rate for steel A probes.

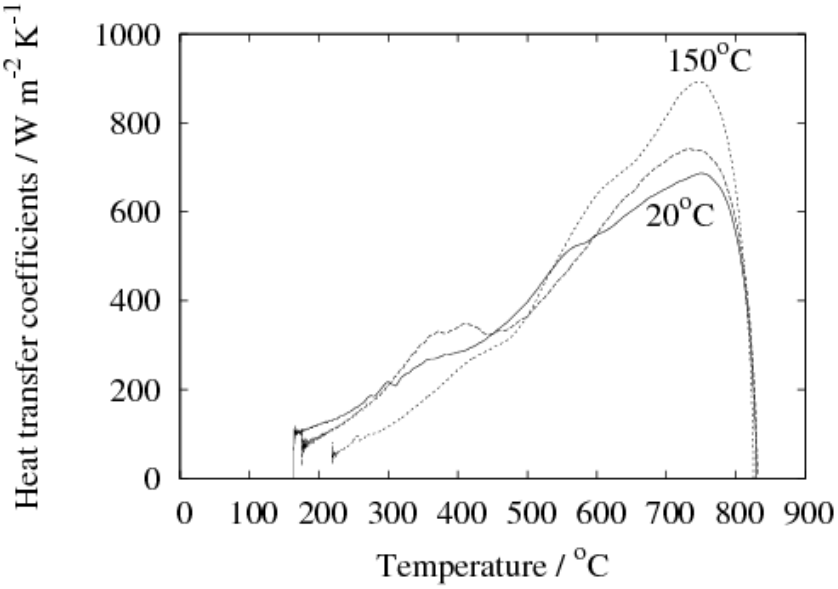

Figure 5-56: Heat transfer coefficient as a function of surface temperature during quenching at different quenchant temperatures (oil).

5.3.1.3 Brine quenching

Aqueous salt solution containing 0.1 volume fraction of salt (NaCl) was used as quenchant at 3 different temperatures 20, 70 and 100°C to study the effect of brine temperature on the heat transfer properties of steel A probe.

Figure 5-57 shows the cooling and cooling rate curve for quenching the steel probe in brine at 20°C. The cooling rate is higher than that obtained by the pure water at the same temperature, because the presence of salt will decrease the propensity for vapour blanket formation and replace it by the boiling stage.

Figure 5-58 shows the calculated heat transfer coefficient as a function of surface temperature. The maximum heat transfer coefficient during the

quenching process is 4200 W $m^{-2}K^{-1}$ at 650°C. In the same way Figures 5-59 to 5-62 show the recorded cooling curves, the calculated cooling rate curves and the heat transfer coefficients as a function of surface temperature during quenching in brine at different temperatures (70 and 100°C).

Increasing the brine temperature produces a decrease in the quench severity (Figures 5-63 to 5-65) as in water but the decrease is not accompanied by extending vapour blanket cooling stage as in water which makes it possible to use the brine in the temperature close to the boiling temperature of the water.

Brine quenching offers superior heat extraction than water quenching. However, a major problem with using the brine quenchants is corrosion. Without special precautions, equipment exposed to the brine solution will quickly be corroded; this will make the cost of the quenching with brine much more expensive, this can be seen from the damage that occurred to our quench probes, thermocouples and furnace (figure 5-66).

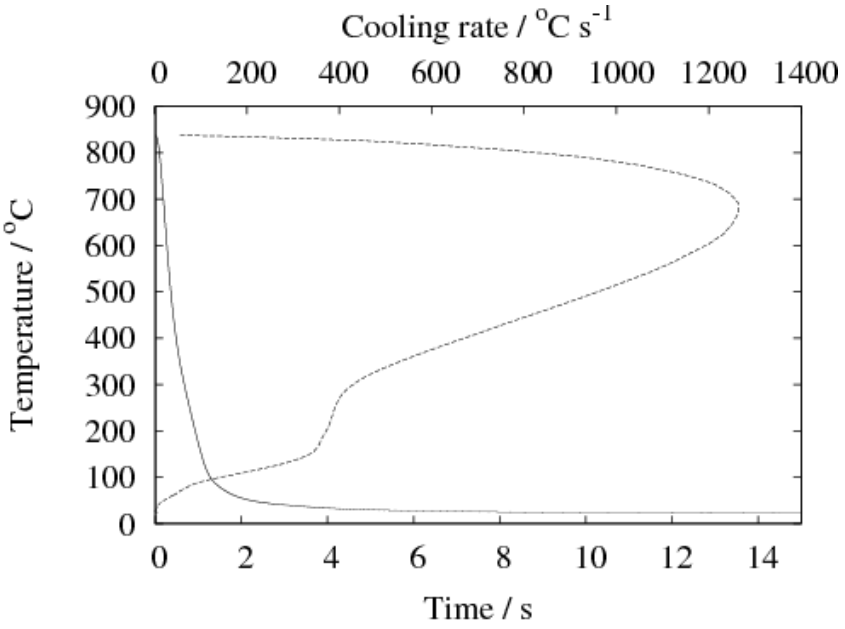

Figure 5-57: Cooling curve (solid) and calculated cooling rate curve (dashed) for steel A quenched in 20°C brine.

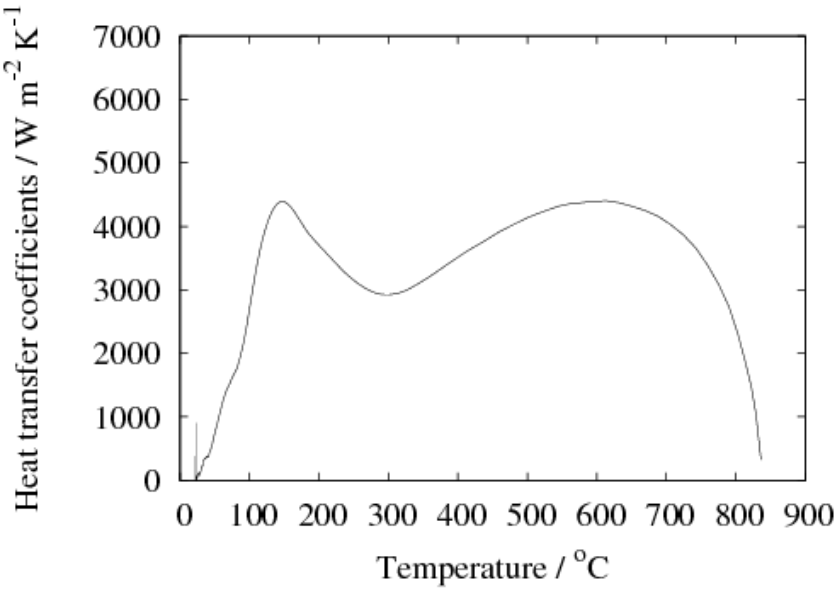

Figure 5-58: Heat transfer coefficient as a function of surface temperature during quenching in brine at 20°C.

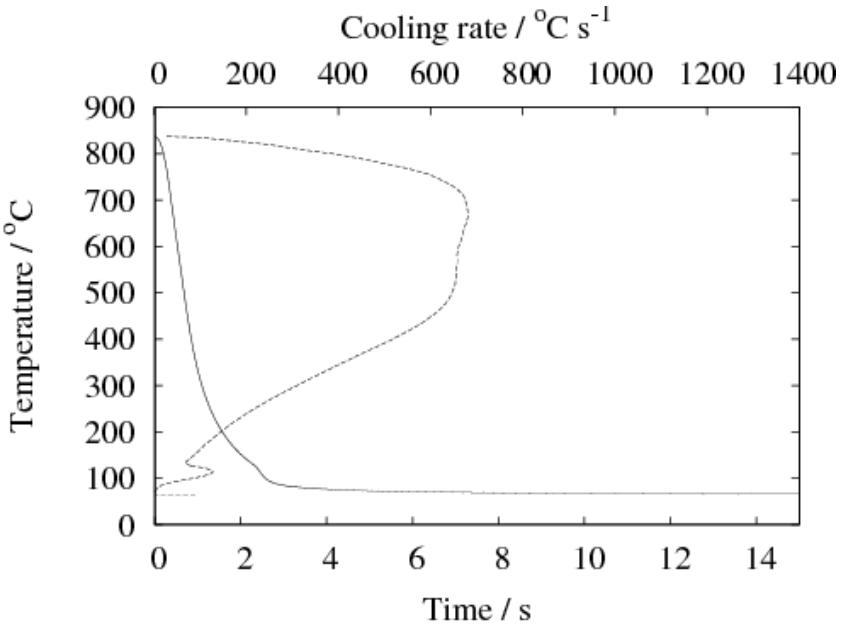

Figure 5-59: Cooling curve (solid) and calculated cooling rate curve (dashed) for steel A quenched in 70°C brine.

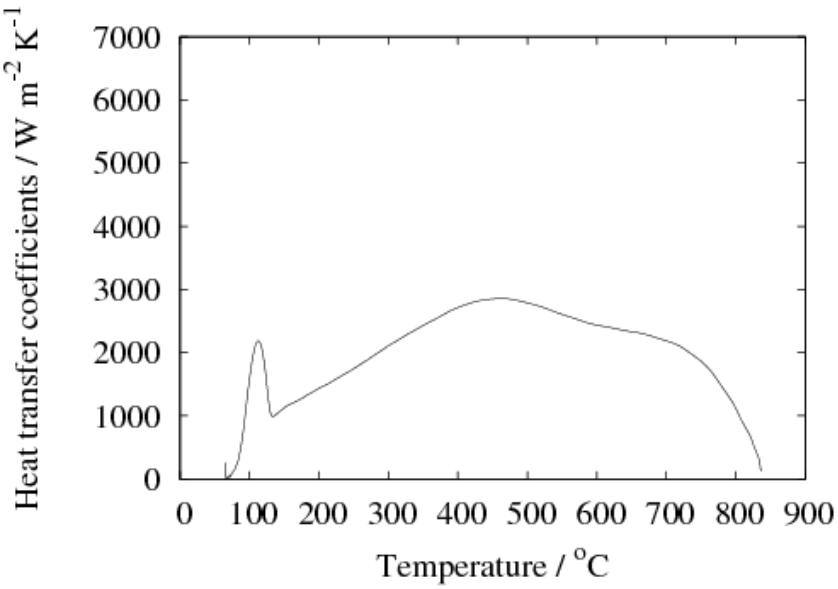

Figure 5-60: Heat transfer coefficient as a function of surface temperature during quenching in brine at 70°C.

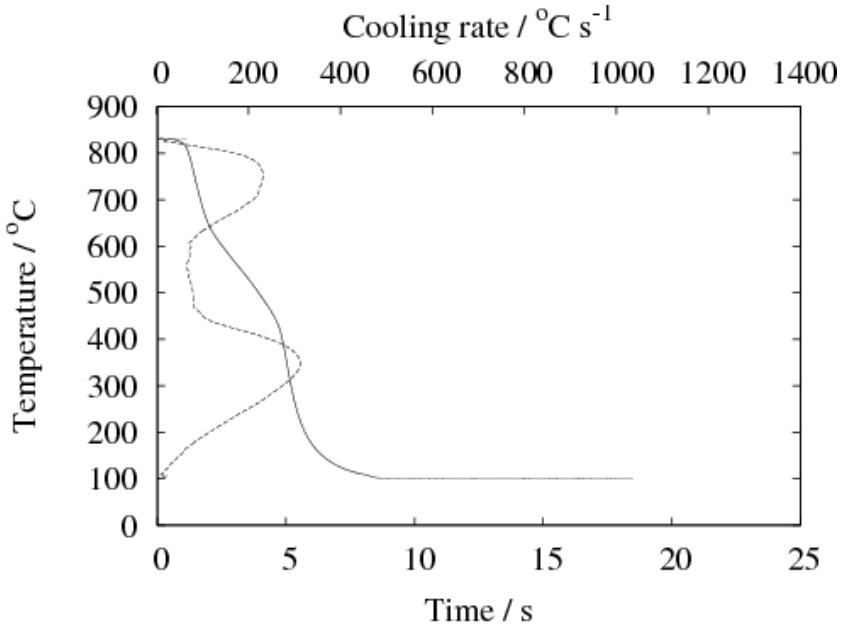

Figure 5-61: Cooling curve (solid) and calculated cooling rate curve (dashed) for steel A quenched in 100°C brine.

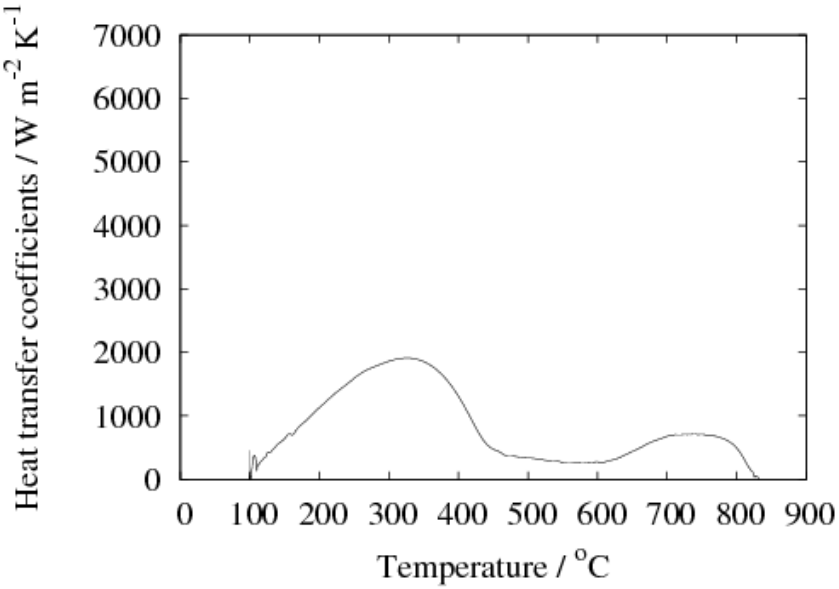

Figure 5-62: Heat transfer coefficient as a function of surface temperature during quenching in brine at 100°C.

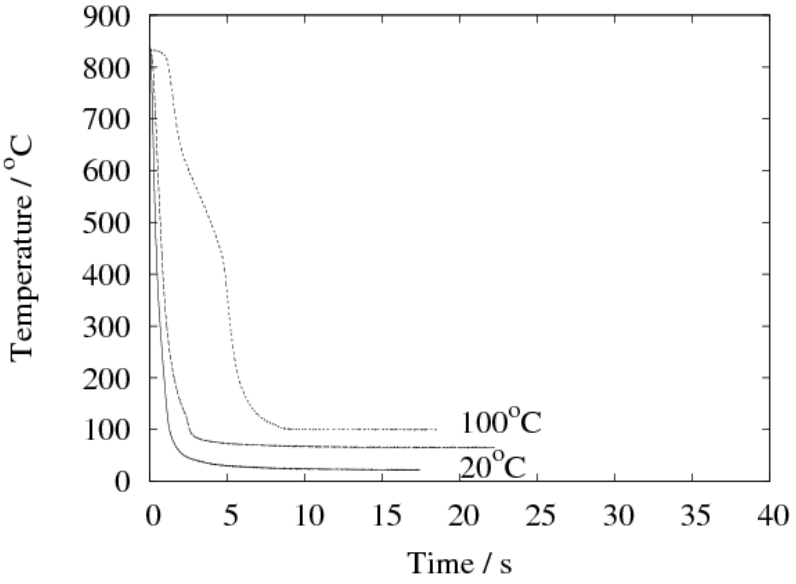

Figure 5-63: Cooling curves for steel A probes at different quenchant (brine) temperatures.

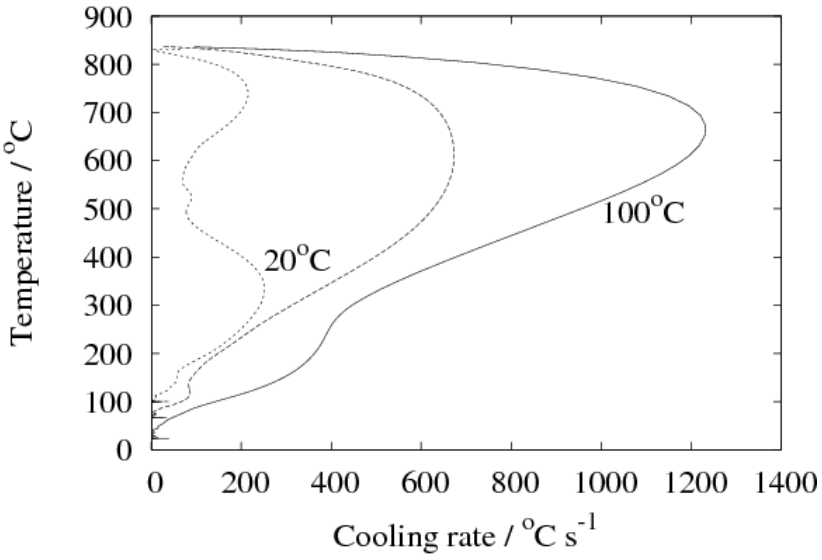

Figure 5-64: Effect of quenchant temperature (brine) on cooling rate for steel A probes.

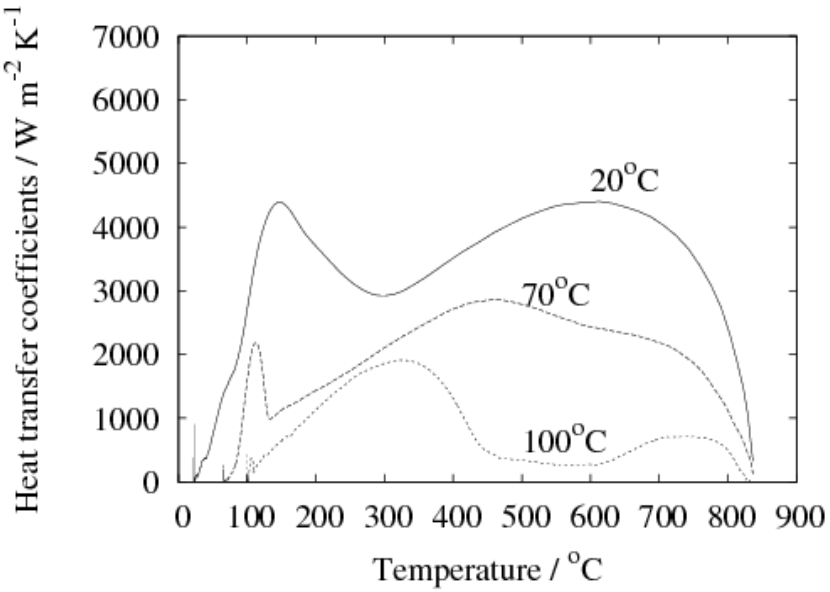

Figure 5-65: Heat transfer coefficient as a function of surface temperature during quenching at different quenchant temperature (brine).

Figure 5-66: the damage occurred to the furnace after using brine solution as a quenchant.

5.3.2 Quench factor and hardness results

Although the cooling rate curve can be quantitatively described, it cannot directly provide information about the associated metallurgical phenomena and the mechanical properties. The method described in Chapter 2 allows a single number (quench factor) to be calculated which encapsulates the factors of the quench severity, which is related to metallurgy via the time-temp-transformation curve. The factor is related to the as-quenched hardness using equation 2.3.

5.3.2.1: Water quenchant

Figure 5-67 shows the change in the quench factor with increasing water temperature while Figure 5-68 shows the calculated hardness as a function of water temperature. There is a reciprocal relationship between the quench factor and the hardness, the lower quench factor value being associated with higher cooling rate, minimum precipitation during cooling and higher hardness levels. Conversely, higher quench factor value is obtained with slower cooling rate and is associated with lower hardness value. We can see from the figure that the critical value is the maximum value of the quench factor, Q, that will result in the desired hardness and this value can be defined in terms of the maximum allowable amount of transformation during cooling. We can see this reciprocal relationship in all the curves for the other quenchants [17, 31].

5.3.2.2 Oil quenchant

Figure 5-69 and 5-70 shows the quench factor with increasing oil temperature and the calculated as-quenched hardness as a function of oil

temperature, there is little variation of the values depending on quenchant temperature compared to water or brine.

5.3.2.3 Brine quenchant

Figure 5-71 shows the calculated quench factor values in the three temperatures, as expected, the quench factor value increases intensely with increasing brine temperature and figure 5-72 shows the decrease of as quenched hardness with increasing brine temperature as was observed in pure water.

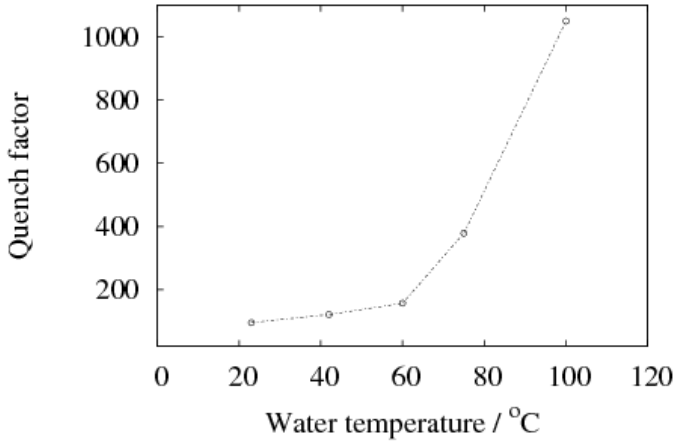

Figure 5-67: Quench factor of steel A as a function of water temperature

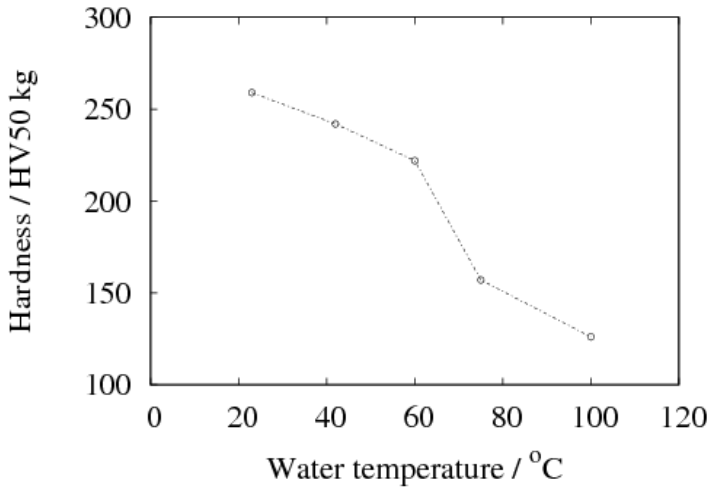

Figure 5-68: Predicted hardness of steel A as a function of water temperature.

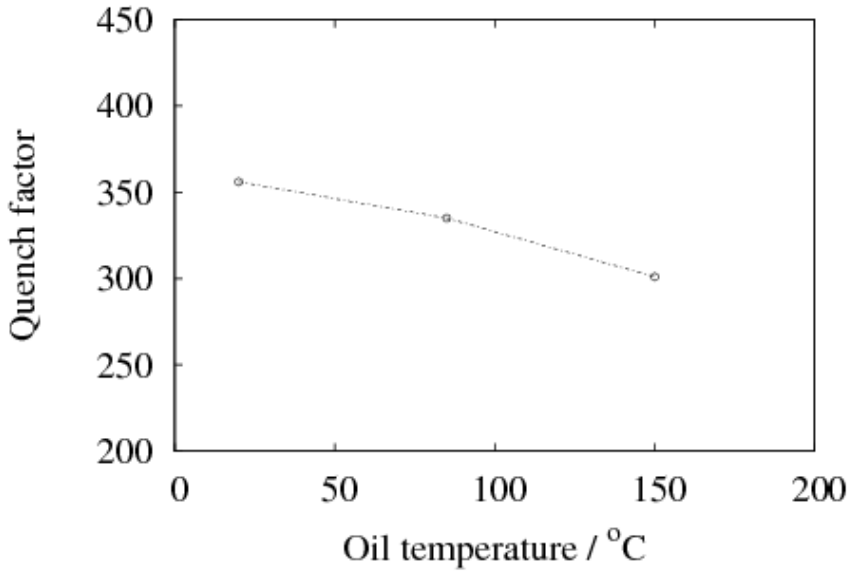

Figure 5-69: Quench factor of steel A as a function of oil temperature.

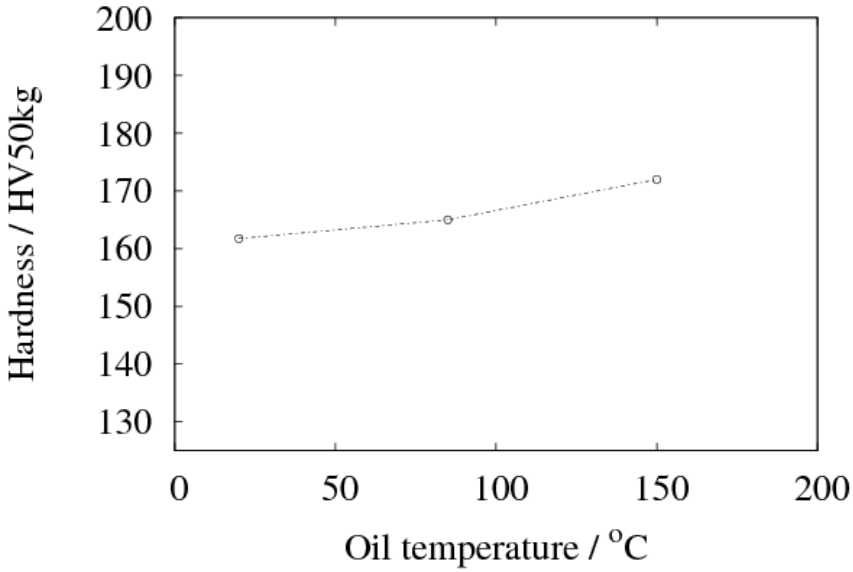

Figure 5-70: Predicted hardness of steel A as a function of oil temperature.

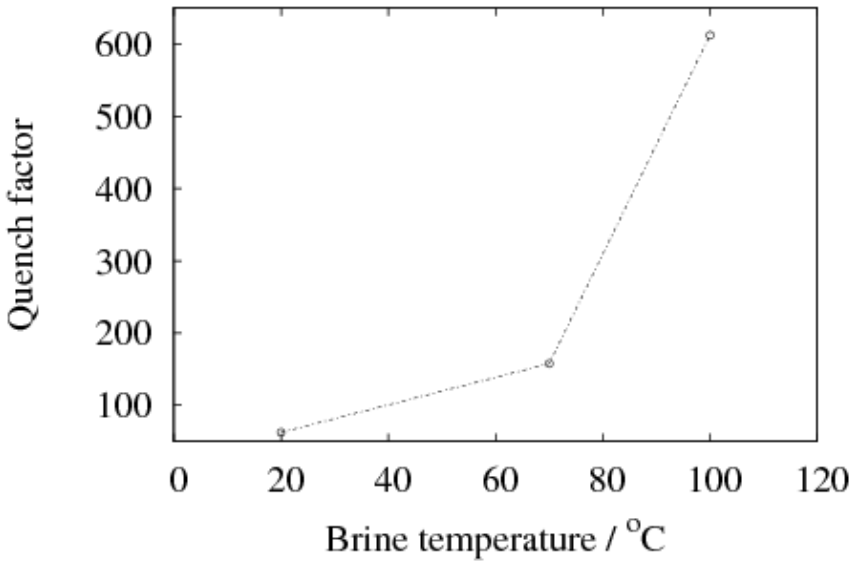

Figure 5-71: Quench factor of steel A as a function of brine temperature.

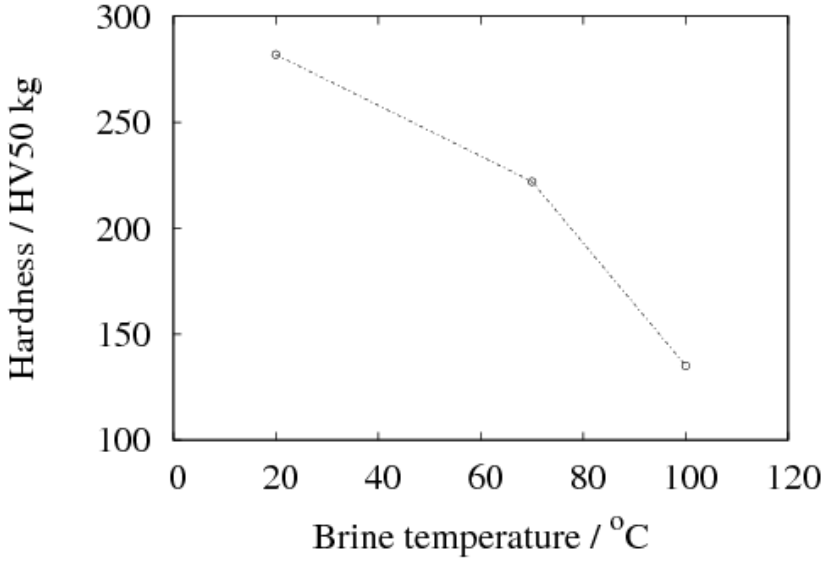

Figure 5-72: Predicted hardness of steel A as a function of brine temperature.

Comparison between the quenchants

The heat transfer rate decreased with increasing quenchant viscosity. The viscosity of the oil as a function of temperature was provided by the supplier [109] while reference [110] provided the corresponding data for water.

Figure 5-73 shows the cooling rates for steel probes quenched in different quenchants at room temperature (water, brine and oil). The heat transfer reaches a maximum with the brine solution with 10% volume percent salt concentration compared with the heat transfer in pure water or oil. Although, it is not always true that the quenchant that produces relatively high cooling rates during the early stages of cooling (A, B) also produces relatively high cooling rate in the martensite transformation region (C stage cooling), because the pure water produce a higher cooling rate in this region.

Comparing the quenching power of the water with that of the oil in figure 5-74 reveals exceptional performance of the water due chiefly to its high latent heat of vaporization (2500 J/g), high specific heat capacity (4.18 J g^{-1} K^{-1} at 23°C), small thermal conductivity (0.6 W m^{-1} K^{-1}) and the low boiling temperature (100 °C). All these thermal properties of water are jointly represented by the diagram of the heat transfer coefficient plotted as a function of temperature of the quenched part surface. Figure 5-74 also shows that the addition of 10% volume fraction salt (NaCl) increases the quench severity of water especially at higher temperatures, by destabilizing the vapour blanket around the hot metal during stage-A cooling which reduces the possibility of soft spots from steam (surface area with less severe quenching).

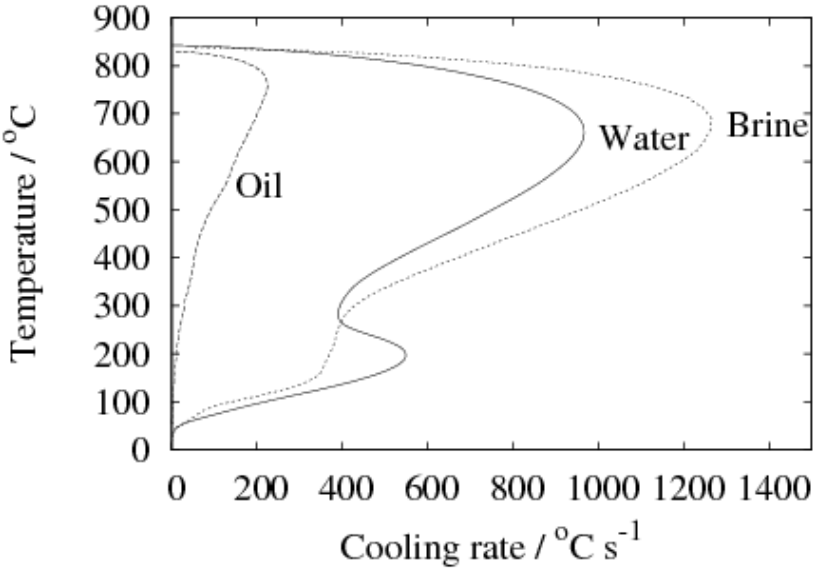

Figure 5-73: Cooling rate as a function of part surface temperature for steel A quenched in different quenchants at room temperature.

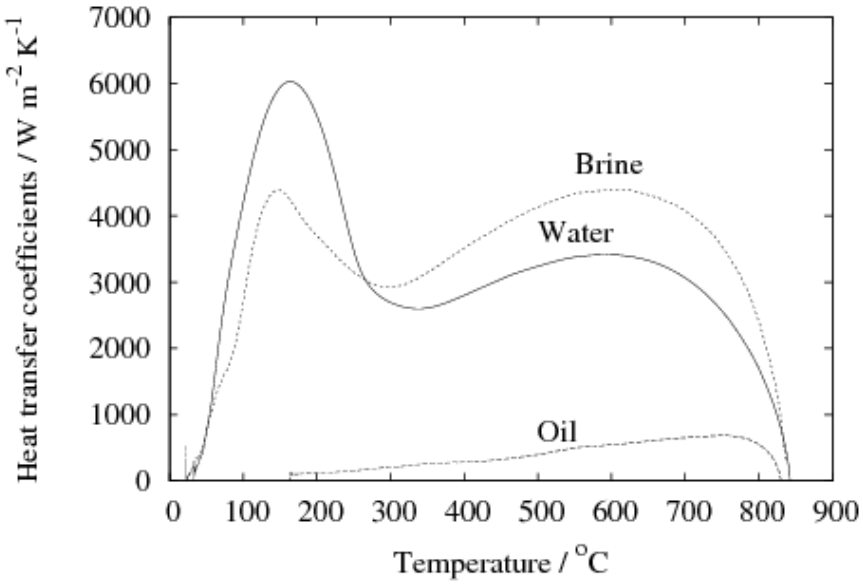

Figure 5-74: Heat transfer coefficient as a function of part surface temperature for steel A probes quenched in different quenchants at room temperature.

Summary

Heat transfer properties have been studied for brine, water, oil at temperatures between 20 to 150°C. The cooling rates and heat transfer coefficients systematically increase with decreasing quenchant viscosity, with the exception of water which is a result of its low viscosity (1 $mm^2 s^{-1}$ at 25°C) [110] as it clear from the figures 5-75 and 5-76 and the formation of a vapour blanket.

Figure 5-75 shows the decrease in the viscosity of water with increase in its temperature, and figure 5-76 shows the heat transfer coefficient value for the probe at 3 different surface temperatures (200, 400, 600°C) during quenching as a function of viscosity.

The heat transfer properties are largely affected by the quenchant temperature, especially in the temperatures range where the pearlite can form, this is due to its effect on the first stage of cooling and on the whole cooling process, though not for the oil because of its high viscosity which reduces as the oil is heated particularly above 100°C (figure 5-77 and 5-78). We can see from figure 5-78 the increase of the heat transfer coefficient with the increase of the quenchant temperature in the temperature range where pearlite usually forms while it is almost the same below 600°C.

Quench factors have been calculated to provide information about the mechanical properties obtained following quenching. The value of the quench factor increases with decreasing the heat transfer properties and that is associated too with decreasing the as quenched hardness for the steel.

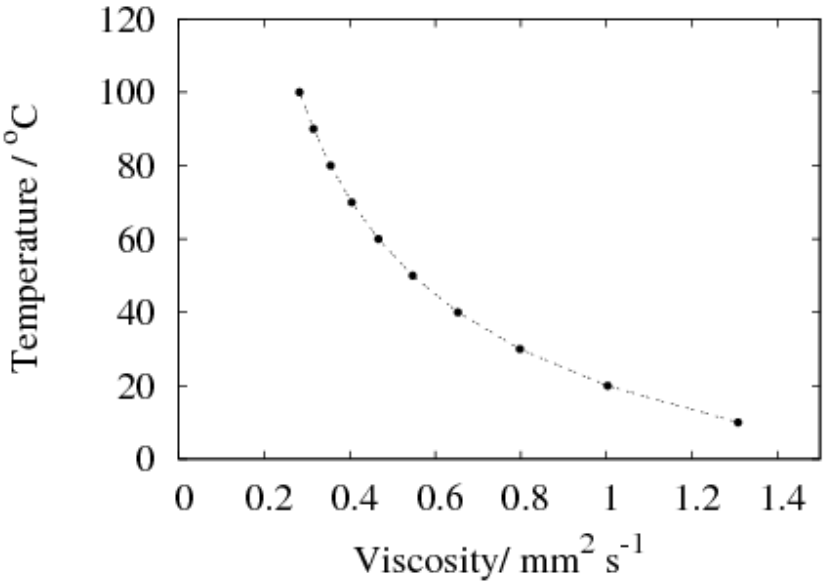

Figure 5-75: Water viscosity as a function of water temperature.

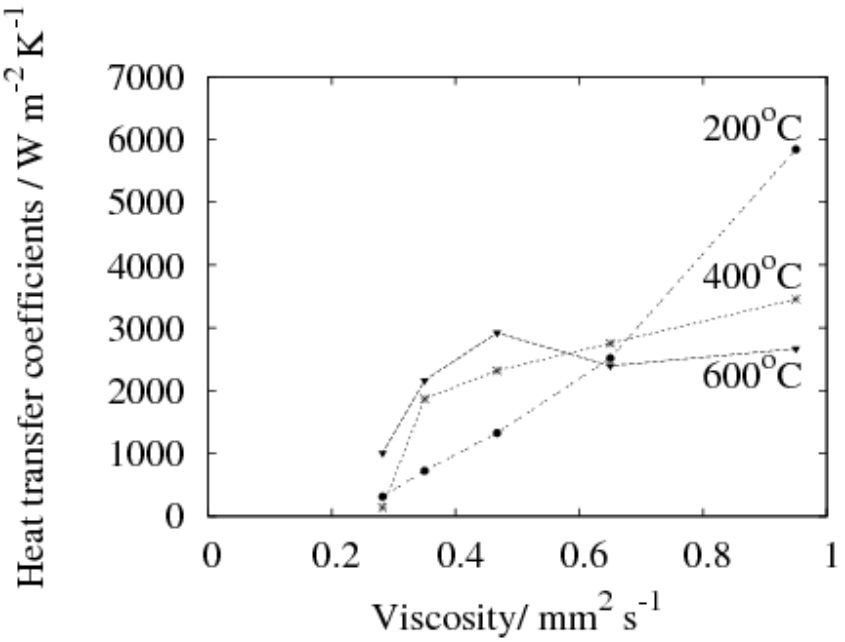

Figure 5-76: Heat transfer coefficient value for the probe at 3 different surface temperatures (200, 400, 600 °C) during the quenching as a function of the water viscosity.

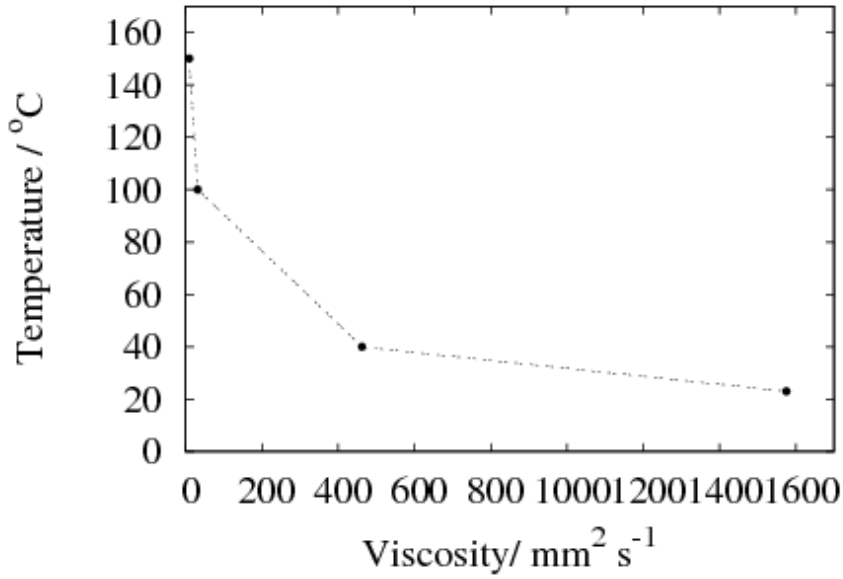

Figure 5-77: Oil viscosity as a function of oil temperature.

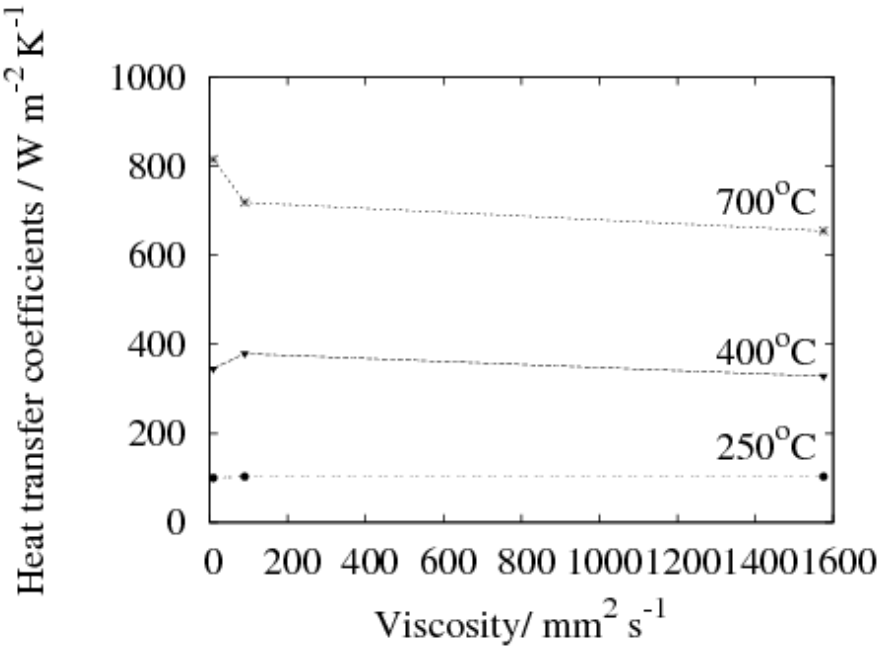

Figure 5-78: Heat transfer coefficient value for the probe at 3 different surface temperatures (250, 400, 700°C) during the quenching as a function of the oil viscosity.

Chapter 6

Conclusions and future work

6.1 Conclusions

1. A probe has been developed to determine the heat transfer coefficient of steel. The probe dimensions were fixed by ensuring an appropriate Biot number so that the probe temperature can be as uniform as possible during the course of the experiments.

2. The latent heat of transformation does affect the temperature field and transformation through thermal transients extending throughout the body of the sample, even at positions away from the quenchant.

3. A general neural network model has been developed, which is capable to predict thermal conductivity.

4. The confidence in the measured heat transfer coefficients is supported by the fact that reasonable predictions could be made of the cooling curves when applied to a steel sample much larger than the probes.

5. The heat–transfer coefficients when combined with calculated cooling and time– temperature–transformation curves, can with the help of the quench factor method enable the estimation of hardness variation as a function of distance.

6. It has been demonstrated that the steel probe, which replicates phase transformations during the course of cooling, is the best for determining the heat–transfer coefficients.

7. The heat transfer properties are greatly affected by the quenchant parameters.

6.2 Suggestions for the future work

1. Improving the mathematical model by including the latent heat in the calculations, in this case the equation for heat transfer coefficient should represent always the maximum values we observed for different compositions steels.

2. Study the effect of the other quenching parameters (agitation and surface roughness) on cooling rate, heat transfer coefficient and mechanical properties for steels.

3. Repeat the same experiments in inert atmosphere to evaluate the effect of surface oxide layer on heat transfer properties.

4. The thermal conductivity model could be enhanced by:
    1. Including calculation of physically meaningful parameters. For example the equilibrium volume fraction of austenite, cementite and ferrite could be included to attempt to distinguish the effect of the different components as they vary as a function of temperature.

    2. It seems likely that any significant improvement to the model would require new experiments to be performed to measure the effect of microstructure, which is required to model thermal conductivity changes as a function of time and temperature.

References

[1] B. Liscic, H. M. Tensi and W. Luty, “Theory and Technology of Quenching”, Springer-Verlag (1992).

[2] D. V. Doane and J. S. Kirkaldy, “Hardenability Concepts with applications to steel”, American Institute of mining, metallurgical and petroleum engineering, Inc (1978).

[3] B. L. Ferguson, Z. Li and A. M. Frebory, Computational Materials Science, 34 (2005) pp. 274-281.

[4] G. E. Totten and M. A. H. Howes, “Steel Heat Treatment Handbook”, Marcel Dekker, Inc (1997).

[5] H. J. Vergara- Hernández and B. Hernández-Morales, Experimental thermal and fluid Science, Accepted manuscript (2009).

[6] H. K. D. H. Bhadeshia, in G. Totten, M. Howes and T. Inone, editors, “Handbook of residual stress and deformation of steels”, ASM International, 2002, pp.3-10.

[7] C. Şimşir and C. Hakan Gür, Journal of materials processing technology, Vol. 207 (2008) pp. 211-221.

[8] R. A. Hardin and C. Beckermann, Proceedings of the 59th Technical and Operating Conference, SFSA, Chicago, IL, 2005.

[9] B. Smoljan: Journal of Materials Engineering and Performance, Vol. 11 (2002), pp. 75-79.

[10] R. N. Penha, L. C. Canale, G. E. Totten, G. Sanchez Sarmiento and J. M. Ventura, Journal of ASTM International , Vol. 3, issue 5 (2006) pp. 89-97.

[11] D. B. Marghitu: "Mechanical Engineers Handbook", Academic Press (2001).

[12] B. K. Dutta, "Heat Transfer, Principles and Applications", Prentice Hall of India (2006).

[13] D. E. Smith, 19th ASM Heat treating Society conference proceeding including steel heat treating in the new millennium, ASM International, Material OH, 1999, pp. 325- 333.

[14] N. Chen, L.Han, W. Zhang and X. Hao, Materials letters, 61(2007), pp. 3021- 3024.

[15] Materials algorithms project (MAP), World Wide Web, www.msm.com.ac.uk/map/mapmain.html.

[16] S. Singer, Journal of Numerical Analysis, Industrial and Applied Mathematics (JNAIAM), Vol. 2, No. 1- 2, 2007, pp. 103- 114.

[17] "Heat Treating of Steel", ASM Handbook Vol. 4, Heat Treating, 1991, ASM International, Materials Park, OH. pp. 67-121.

[18] C. E. Bates, G. E. Tooten and N. A. Clinton, "Handbook of Quenchants and Quenching Technology", ASM International, Materials Park, OH, 1993.

[19] L. C. F. Canale, G. Sanchez Sarmiento, G. E. Totten, I. Felde and R. N. Penha, http://www.kbeng.com.ar/rpublications.html

[20] B. Hernández-Morales, J. S. Téllez-Martinez, A. Ingalls-Cruz and J. A. Barrera Godlínez, 19th ASM Heat treating Society conference proceeding including steel heat treating in the new millennium, ASM International, Material OH, 1999, pp. 284- 291.

[21] S. Ma, A. S. Varde, M. Takahashi, D. K. Rondeau, M. Maniruzzaman and R. D. Sisson, Proceedings of the Fourth International Conference on Quenching and the Control of Distortion, 20-23 May 2003, Beijing.

[22] K. Funatani, M. Narazaki and M. Tanaka, 19th ASM Heat treating Society conference proceeding including steel heat treating in the new millennium, ASM International, Material OH, 1999, pp. 255- 263.

[23] A. G. Ksenofontov and S. Y. Shevchenko, Metal Science and Heat treatment, Vol. 40 (1998), pp. 9-10.

[24] N. Chen, W. Zhang, C. Gao, B. Liao, and J. Pan, Solid state phenomena, Vol. 118 (2006), pp. 227-232.

[25] I. Tamura, N. Shimizu, and T. Okada; J. of Heat Treating, VOL. 3, NO. 4, December (1984), pp. 335-343.

[26] X. Chen, L. Meekisho and G. E. Totten, 19th ASM Heat treating Society conference proceeding including steel heat treating in the new millennium, ASM International, Material OH, 1999, pp. 453-460.

[27] G. E. Totten and Y. H. Sun, 19th ASM Heat treating Society conference proceeding including steel heat treating in the new millennium, ASM International, Material OH, 1999, pp. 292- 297.

[28] C. Heming, H. Xieqing and X. Jianbin, Journal of Materials Processing Technology, 138 (2003), pp. 399- 402.

[29] H. K. Kim and S. I. Oh: Journal of Materials Processing Technology, 112 (2001), pp. 157- 165.

[30] D. A. Guisbert and D. L. Moore, 19th ASM Heat treating Society conference proceeding including steel heat treating in the new millennium, ASM International, Material OH, 1999, pp. 264- 269.

[31] G. E. Totten, H. M. Tensi and B. Liscic, Heat Treatment of Metals, 4 (1997), pp. 92-94.

[32] [32] Japanese Industrial Standard K 2242, "Heat Treating Oils", 1980.

[33] Tagaya and I. Tamura, Journal of Hart.-Tech. Mitt., Vol. 18(1963) pp. 63- 67.

[34] ASTM D6200 -01(2007), Standard test method for determination of cooling characteristics of quench oils by cooling curve analysis.

[35] C. E. Bates and G.E. Totten, Heat Treatment of metals, Vol. 4 (1988) pp. 89-97.

[36] N. B. Pilling, Physical Review, Vol. XIV., Second series, Septemper (1991) pp. 222-230.

[37] N. Lambert and M. Economopoulos, Journal of Iron and Steel institute, October (1970), pp. 917-928.

[38] J.Cai, L. Chuzhoy, C. Berndt, G. Keil, K. Burris and M. Taft, 19th ASM Heat treating Society conference proceeding including steel heat treating in the new millennium, ASM International, Material OH, 1999, pp. 299-300.

[39] M. Maniruzzaman and R. D. Sisson Jr, Journal of Physics IV France 120 (2004), pp. 269-276.

[40] N. Chen, B. Liao, J. Pan, Q. Li and C. Gao, Materials letters, 60 (2006), pp. 1659-1664.

[41] B. Smoljan, Journal of Materials Processing Technology, 175 (2006), pp. 393- 397.

[42] K. Narayan Prabhu and P. Fernandes, Materials and Design, 28 (2007), pp. 544- 550.

[43] C. Heming, H. Xieqing and W. Honggang, Journal of Materials Processing Technology, 89-90 (1999), pp. 339-343.

[44] I. Felde, T. Réti, G. Sánchez Sarmiento, M. G. Palandella, G. E. Totten, X. L. Chen, http://www.kbeng.com.ar/pdf/Paper_Indianapolis_2001_Imre.pdf.

[45] K. Narayan Prabhu and P. Fernandes: Materials and design, 28 (2007), pp. 544-550.

[46] L. Huiping, Z. Guoqun, N. Shanting and L. Yiguo, Finite Element in Analysis and Design, 42(2006), pp. 1087-1096.

[47] P. Masson, T. Loulou, E. Artioukhine, P. Rogeon, D. Carron and J. Quemener, International Journal of Thermal Science, 41(2002), pp. 517-527.

[48] J. Taler and W. Zima, International Journal of Heat and Mass Transfer, 42 (1999), pp. 1123-1140.

[49] M. Narazaki, K. Osawa, A. Shirayori and S. Fuchizawa, 19th ASM Heat treating Society conference proceeding including steel heat treating in the new millennium, ASM International, Material OH, 1999, pp. 600-607.

[50] S. Segerberg and J. Bodin, Heat treating , may (1988), pp. 26-28.

[51] S. Segerberg, J. Bodin and I. Felde, Proceedings of the Fourth International Conference on Quenching and the Control of Distortion, 20-23 May 2003, Beijing, pp. 183-186.

[52] E. Troell, H. Kristoffersen, J. Bodin, S. Segerberg and I. Felde, Z. Werkst, Wärmebeh, Fertigung 62 (2007) 3.

[53] L. Huiping, Z. Guoqun, H. Lianfang, and M. Yue: Measurement, Vol. 41(2008), pp. 676- 686.

[54] J. T. Staley and J. W. Evancho, Metallurgical Transactions, Vol. 5 (1974), pp. 43- 47.

[55] G. E. Totten, G. M. Webster and C. E. Bates, http://www.quenchtek.com/pdf_files/technical_paper/pdf.

[56] D. S. MacKenzie and J. W. NewKirk: International Federation of Heat Treatment and Surface Engineering Conference, September 11-14, 2001 in Dubrovnik, Croatia.

[57] P. A. Rometsch, M. J. Starink and P. J. Gregson, Materials Science and Engineering A339 (2003), pp. 255-264.

[58] S. Ma, M. Maniruzzaman, D. S. Mackenzie and R. D. Sisson, Metallurgical and Material Transactions B, Vol.38B (August 1974), pp. 583-589.

[59] R. J. Flynn and J. S. Robinson, Journal of Materials Processing Technology, 153-154 (2004), pp. 674-680.

[60] G. P. Dolan and J. S. Robinson, Journal of Materials Processing Technology, 153-154 (2004), pp. 346-351.

[61] P. A. Rometsch, M. J. Starink and P. J. Gregson, Materials Science and Engineering A339 (2003), pp. 255-264.

[62] H. K. D. H. Bhadeshia and R.W. K. Honeycombe, “Steels, microstructure and properties” Elsevier Ltd. (2006).

[63] P. Fernandes and K. Prabhn, Journal of Materials Processing Technology, 183 (2007) pp. 1- 5.

[64] A. J. Fletcher, “Thermal Stress and Strain Generation in Heat Treatment”, Elsevier Applied Science (2001).

[65] C. R. Brooks, “Heat Treatment of Ferrous Alloy”, Hemisphere Publishing Corporation (1979).

[66] D. S. Mackenzie, Presented at the ASM Heat treating show and exposition, Indianapolis, IN, 15-18 September, 2003.

[67] D. S. Mackenzie and D. Lambert, Presented at the 6th International conference on quenching and control of residual stresses conference, Beijing PRC, 24-27 November 2003.

[68] A. Zehtab Yazdi, S. A. Sajjadi, S. M. Zebarjad and S. M. Moosavi, Journal of Materials Processing Technology, Vol. 199 (2008), pp. 124-129.

[69] V. S. Arpaci, "Conduction heat transfer", Addison-Wesley (1966).

[70] J. P. Holman, "Heat Transfer", McGraw-Hill, Inc (2004).

[71] G. E. Myers, "Analytical methods in conduction heat transfer", McGraw-Hill, Inc (1971).

[72] C. F. Weber: International Journal of Heat and Mass transfer, Vol. 24, No. 11 (1981), pp. 1783-1792.

[73] S. Chantasiriwan: International Communication in Heat and Mass transfer, Vol. 27, No. 8 (2000), pp. 1155-1164.

[74] A. Buczek and T. Telejko, Journal of Materials Processing Technology, 155-156 (2004), pp. 1324-1329.

[75] C. Heming, X. Jianbin and L. Jianyun; Computational materials science, 29 (2004), pp. 453-458.

[76] G. S. Sarmiento, X. Chen, J. Vega, G. Totten, R. Raynoldson, L. Huynh and L. Meekisho: http://www.getottenassociates.com/pdf_files/HT%20MOD%20-%20A%20Comparison.pdf.

[77] F. Kreith, "Mechanical Engineering Handbook", CRC Press LLC (1999).

[78] W. F. Gale and T.C. Totemeier, "Smithells Metals Reference Book", Elsevier Inc. (2004).

[79] Materials algorithms project (MAP), World Wide Web, www.msm.com.ac.uk/map/Steel/ Programs/ Thermal model.html

[80] Efunda material property data, http://www.efunda.com/home.cfm.

[81] Matweb, material property data, http://www.matweb.com/.

[82] H. K. D. H. Bhadeshia: ISIJ International, Vol. 39(1999), pp. 966 - 979.

[83] R. Kemp, "Alloy design for fusion power plant" ,PhD thesis, University of Cambridge, 2006.

[84] W. M. Rohsenow, J. P. Hartnett and Y. I. Cho, "Handbook of heat transfer", third edition, Mc Graw-Hill companies, Inc. , 1998.

[85] N. F. Mott and H. Jones, "The theory of the properties of metals and alloys", Dover publications, Inc., 1958.

[86] J. M. Ziman, "Electron and phonons, the theory of transport phenomena in solids", Oxford university press, 1960.

[87] E. Nechtelberger, "The properties of cast irons up to 500°C", Technical report, Technicopy Ltd, 1980.

[88] F. Richter, "Die Wichtigsten Physikalishen Eigenschaften von 52 Eisenwerkstoffen", Verlag Stahleisen mbH, 1973.

[89] R. W. Powell, In "The physical properties of a series of steels-part II", paper No. 23 of the alloy steels research committee, (1964) pp. 116-121.

[90] H. K. D. H. Bhadeshia, R .C. Dmitriu, S. Forsik, J. H. Pak, and J. H. Ryu, Materials Science and Technology, Vol. 25, No. 4 (2009) pp. 504-510.

[91] David J. C. MacKay, In H. Cerjak and H. K. D. H. Bhadeshia, editors, Mathematical modelling of weld phenomena 3.

[92] David J.C. MacKay, "Bayesian methods for adaptive models", PhD thesis, Caltech, 1991.

[93] D. J. C. MacKay, Neural Computation, Vol. 4 (1992) pp. 415-447.

[94] D. J. C. MacKay, Neural Computation, Vol. 4 (1992), pp. 448-472.

[95] H. Fujii, D. C. MacKay and H. K. D. H. Bhadeshia, ISIJ International, Vol. 36, No. 11(1996), pp. 1373-1382.

[96] J. H. Ryu and H. K. D. H. Bhadeshia, Materials and Manufacturing Processes, Vol. 24 (2009), pp. 1-7.

[97] L. Gavard, H. K. D. H. Bhadeshia, D. J. C. MacKay and S. Suzuki, *M*aterials Science and Technology, Vol. 12 (1996), pp. 453-463.

[98] J. Pak, J. Jang, H. K. D. H. Bhadeshia and L. Karlsson, Materials and Manufacturing Processes, Vol. 24 (2009), pp. 16-21.

[99] M. A. Yescas, International Journal of Cast Metals Research, Vol. 15 (2003), pp. 513-521.

[100] T. Cool and H. K. D. H. Bhadeshia, Materials Science and Technology, Vol. 2, January (1996), pp. 40-44.

[101] T. Sourmail, H. K. D. H. Bhadeshia, and D. J. C. MacKay, Materials Science and Technology, Vol. 18, June (2002), pp. 655-663.

[102] T. Sourmail and H. K. D. H. Bhadeshia in "Introduction to materials modelling",Maney publishing (2005).

[103] D. J. C. MacKay, Neural Computation, Vol. 4, No. 4 (1992), pp. 590-604.

[104] H. K. D. H. Bhadeshia , "Neural Networks and Genetic Algorithms in Materials Science and Engineering", Tata McGraw-Hill Publishing Company Ltd., India, January 11-13, 2006,

[105] URL: http://www.neuromat.com/.

[106] Hasan and Peet, http://www.msm.cam.ac.uk/map/data/materials/thermaldata.html.

[107] L. Leibowitz and R. A. Blomquist, International Journal of thermophysics, Vol. 9, No. 5(1988), pp. 873-883.

[108] D Carrouge, H. K. D. H. Bhadeshia and P. Woollin, Science and Technology of Welding and Joining, Vol. 9, No. 5(2004), pp. 377-389.

[109] Technical data sheet for Micron GP 460, Specialised products (Western) Ltd.

[110] Wikipedia, http://en.wikipedia.org/wiki/Viscosity.